Experimental studies of nuclei near doubly magic 100Sn and 78Ni

A Dissertation Presented for
the Doctor of Philosophy Degree
The University of Tennessee, Knoxville

Lucia Cartegni
May 2012

Copyright © 2011 by Lucia Cartegni.
All rights reserved.

Acknowledgments

First of all I want to thank Prof. Robert Grzywacz, the best advisor and teacher any student could hope for. I also want to thank my other committee members: Prof. Carrol Bingham, Prof. Lee Riedinger, Prof. Thomas Papenbrock and Prof. Jason Hayward. All of my committee members have always been available and helped me with insightful comments and constructive criticism. I am grateful to all of the people working at ORNL and NSCL, especially to Dr. Carl Gross and Dr. Krzysztof Rykaczewski, who have always been willing to share their knowledge with me. I am very grateful to Dr. Chiara Mazzocchi for her friendship and her invaluable help with physics. A special thanks goes to Prof. Marianne Breinig, who gave me excellent advice and encouragement, and pointed out areas where I needed improvement. Many thanks to the graduate students and postdocs in the group, always very friendly and helpful. It would be impossible to mention here all of the friends that I want to thank.

Infine desidero ringraziare le persone che mi sono più care, e che in questi anni mi hanno sempre dato il loro appoggio: i miei genitori, il nonno Alfredo, i miei fratelli Emanuele e Pietro, e il mio carissimo Dwayne.

Abstract

The experimental study of exotic nuclei is very important for our understanding of nuclear structure. In this work the nuclei near doubly magic nuclei ^{100}Sn and ^{78}Ni were studied in two separate experiments. The first one was performed at the Holifield Radioactive Ion Beam Facility (HRIBF) at Oak Ridge National Laboratory. This experiment searched for the alpha decay of ^{112}Cs, in order to establish the proton separation energy of ^{104}Sb. Although the alpha decay of ^{112}Cs was not observed, the upper limit of the alpha branching ratio was set at 0.26%. The improved statistics enabled an improved half-lives measurement of ^{112}Cs, with the result of 506(55) microseconds. From these measurements and systematics arguments new limits for the proton separation energies of ^{104}Sb and ^{108}I were established. These estimates were compared to shell model calculations. The decay properties of ^{111}Xe, the proton decay daughter of ^{112}Cs, were also re-investigated. The alpha branching ratio for 111Xe was measured as 10.4(1.9)%.

The second experiment was performed at the National Superconducting Cyclotron Laboratory (NSCL) at Michigan State University. It was aimed to measure the half-life of excited states in two neutron-rich isotopes of nickel: ^{70}Ni and ^{72}Ni. These isotopes of Ni are close to doubly magic ^{78}Ni, and therefore particularly interesting for the investigation of shell closure effects. The experiment attempted to measure the lifetimes of electromagnetic transitions from 4+ to 2+, and from 2+ to ground state. The results for the 2+ transition in ^{70}Ni show a lifetime of the order of 10 ps, significantly longer than expected from a previous experiment.

Contents

1 Introduction **1**

2 Alpha decay of proton-rich nuclei in the ^{100}Sn region **3**

2.1 Alpha decay 5

2.2 Experimental studies of alpha decay near ^{100}Sn 6

2.3 The ^{112}Cs experiment 8

2.4 Astrophysical interest 8

2.5 Odd-even effect 12

3 The ^{112}Cs experiment **15**

3.1 The Holifield Radioactive Ion Beam Facility 15

3.2 Beam and reaction target 15

3.3 The Recoil Mass Spectrometer 16

3.4 RMS focal plane detectors 19

3.5 Digital data acquisition system 22

4 Data analysis and results of the ^{112}Cs experiment **24**

4.1 Calibration of the DSSD 24

4.2 Background reduction 29

4.3 Detection efficiency 32

4.4 Results for ^{112}Cs 35
4.4.1 Proton decay 35
4.4.2 Alpha decay 36
4.4.3 Proton separation energies 40
4.4.4 Odd-even effect 40
4.5 Results for ^{111}Xe 42
4.5.1 Alpha branching ratio of ^{107}Te 42
4.5.2 Alpha branching ratio of ^{111}Xe 44
4.5.3 Alpha reduced widths 44
4.6 Summary 47

5 The ^{70}Ni and ^{72}Ni experiment **49**
5.1 Motivation 49
5.2 The Plunger method 51
5.3 Setup 53

6 Data analysis and results of the ^{70}Ni experiment **59**
6.1 Detectors calibration 60
6.1.1 SeGa calibration 60
6.1.2 CRDC calibration 62
6.1.3 Ion chamber calibration 65
6.2 Particle identification 69
6.2.1 Incoming particle identification 69
6.2.2 Outgoing particle identification 69
6.3 Gammas from ^{70}Ni 73
6.4 Particle tracking 78
6.5 Simulations 79
6.5.1 Half-life of ^{70}Ni excited states 80

6.6 Summary 82

Bibliography **94**

Vita **106**

List of Tables

2.1 Properties of alpha emitters above ^{100}Sn: half-life ($T_{1/2}$), branching ratio (b_α), and energy (E_α). Reference (a) [Liddick et al., 2006], (b) [Schardt et al., 1981], (c) [Page et al., 1994a], (d) [Schardt et al., 1979], (e) [Heine et al., 1992], (f) [Audi et al., 2003], (g) [Kirchner et al., 1977], (h) [Dombrádi et al., 1995], (i) [Mazzocchi et al., 2007], (j) [Tidemand-Petersson et al., 1985], and (k) [Roeckl et al., 1980]. 7

4.1 Ranges (R) in silicon and detection efficiencies calculated for alphas and protons of different energies in the DSSD. For these calclations it was assumed that particles were emitted in the DSSD at a position of $11.24 \pm 0.62\,\mu$m, corresponding to the implantation depth of ^{112}Cs ions in this experiment. . 35

4.2 Summary of the newly estimated Q_p and Q_α values. 42

4.3 Summary of alpha decay properties of ^{111}Xe and ^{107}Te: energy (E_α), branching ratio (b_α), reduced alpha-decay width (δ^2) and reduced alpha-decay width relative to ^{212}Po (W_α). See text for details. 47

5.1 List of the experimental runs, grouped by S800 and plunger settings; d is the target-degrader distance. 58

6.1 Detectors used for TOF measurements. Refer to Figure 5.4 for the position of the scintillator along the meam line. 69

6.2 List of the main beam parameters that need to be adjusted in the simulations. See text for details. 79

List of Figures

2.1 Chart of nuclides [BNL, 2011]. The color map illustrates the main decay mode for each nucleus. 4

2.2 Portion of the nuclide chart above ^{100}Sn. The arrows show decay chains starting at ^{112}Cs. 9

2.3 Path of the rp-process during an X-ray burst. Continuous lines represent reaction flows of more than 10% of the reaction flow through the 3α reaction, while dashed lines represent reaction flows of 1%-10% [Schatz et al., 2001]. 11

2.4 Termination of the rp-process. Continuous arrows represent the calculated path [Schatz et al., 2001]. Dashed arrows represent an alternative path. . . 13

2.5 Branching of the rp-process into proton capture at various Sb isotopes as a function of $Q_p = -S_p$ [Mazzocchi et al., 2007]. 13

2.6 Q_p values for neutron-deficient Sb (Z = 51), I (Z = 53) and Cs (Z = 55) isotopes. Full symbols represent measured values [Blank and Borge, 2008] while open symbols represent extrapolations [Audi et al., 2003]. 14

3.1 Schematic drawing of the Holifield Radioactive Ion Beam Facility. 17

3.2 Schematic drawing of the RMS [Ginter, 1999]. 17

3.3 A/Q spectra of ions going through the MCP foil. The horizontal position measured by the MCP is on the horizontal axis and corresponds to the mass/charge ratio. Upper panel: no slits. Lower panel: with slits. The labels next to the peaks show the corresponding mass/charge states. 18
3.4 Picture of the DSSD. 20
3.5 Picture of the DSSD-Si box assembly. The energy degrader is visible on top of the silicon box. The DSSD is located underneath the box in this view. . 20
3.6 Schematic view of the DSSD and veto detectors. Arrow number 1 represents the trajectory of an ion detected by the MCP and then implanted in the DSSD. Arrows number 2, 3, and 4 represent the trajectories of particles escaping the DSSD. Arrow number 5 represents the trajectory of a particle not escaping the DSSD. 21
3.7 Schematic drawing of the electronic chain from the detector to the DGF module. 23
3.8 Picture of the DGF module. 23

4.1 Energy spectra before (left) and after (right) the gain matching procedure. The channel number, corresponding to energy, is on the horizontal axis. The front strip number is on the vertical axis. 25
4.2 Upper panel: time-energy spectrum of decays in the DSSD. Lower panel: analytical function used to fit the data points. The function is evaluated on a grid corresponding to the energy and time channels. 27
4.3 Time-energy spectrum of protons after applying the time-dependent energy correction. 28
4.4 Correlation spectra of decay events. The energy of the 1^{st} generation decay is on the vertical axis, and the energy of the 2^{nd} generation decay is on the horizontal axis. The energy scales are 2 keV/ch. Left panel: no condition is applied. Right panel: the anticoincidence condition is applied. 31

4.5 Correlation spectra of decay events. The energy of each decay is on the vertical axis, and the energy of the next decay at the same DSSD position is on the horizontal axis. The energy scales are 2 keV/ch. Left panel: no condition is applied. Right panel: the anticoincidence condition is applied. . 33

4.6 Correlation spectra of decay events. The energy of the 1^{st} generation decay is on the vertical axis, and the energy of the 2^{nd} generation decay is on the horizontal axis. The energy scales are 2 keV/ch. Upper left panel: no condition is applied. Upper right panel: the energy difference condition is applied. Lower left panel: the anticoincidence condition is applied. Lower right panel: both the anticoincidence and the energy difference conditions are applied. 34

4.7 Portion of the energy spectrum of decay events following the implantation of an ion in the same pixel of the detector. This spectrum shows decays within 5 ms of a recoil. 37

4.8 Proton decay of ^{109}I and ^{112}Cs, with the time decay curve used to determine the half-life of ^{112}Cs. The dashed line represents the decay of ^{112}Cs, and the dotted line represents the decay of ^{109}I. 38

4.9 Decay-decay correlated events: the energy of the first decay event detected after ion implantation is on the horizontal axis, while the energy of the second decay event in the same DSSD pixel is on the vertical axis. The box shows where alpha decay of ^{112}Cs, correlated to alpha decay of ^{108}I (3947 ± 5 keV [Page et al., 1994a]), would be expected. 39

4.10 Alpha branching ratio of ^{112}Cs as a function of its Q_α value. The green (dark) and the yellow (light) bands represent the value with error bars calculated for l=0 and l=2 respectively. The horizontal line shows the measured upper limit for the alpha branching ratio. The dashed vertical line shows the estimated upper limit for the Q_α value. See text for details. 41

4.11 Q_p values for neutron-deficient Sb (Z = 51), I (Z = 53) and Cs (Z = 55) isotopes. Full symbols represent measured values [Blank and Borge, 2008] while open symbols represent extrapolations [Audi et al., 2003]. The boxes represent the energy windows expected for the proton separation energies of ^{104}Sb and ^{108}I ([Page et al., 1994a] and present work). The symbols connected by the dotted line represent shell model calculations. See text for details. . 43

4.12 Partial beta half-life T_β for odd-A tellurium isotopes [Blachot, 2006,Blachot, 2009, Blachot, 2005a, Blachot, 2005b] as a function of the mass number A. The straight dashed line represents a linear fit on $\ln(T_\beta)$, used to estimate the beta half-life of ^{107}Te. 45

4.13 Energy spectrum of the alpha decay of ^{111}Xe. These decay events are selected by requiring that the next decay in the same DSSD pixel belongs to ^{107}Te. Both the ^{111}Xe alpha transitions are present in the spectrum. 46

5.1 Experimental B(E2;$0^+ \rightarrow 2^+$) values for even-even nickel and zinc isotopes. The dashed and dotted lines represent shell model calculations. (Figure taken from [Perru et al., 2006]). 50

5.2 Left panel: schematic drawing of the plunger device, at three different target-degrader distances. Right panel: the experimental energy spectra. The dark gray color corresponds to gammas emitted before the degrader, while the light gray color corresponds to gammas emitted after the degrader. The energies are measured by detectors at a forward angle. (Figure taken from [Adrich et al., 2009]). 52

5.3 Picture of the Köln-NSCL plunger device [Adrich et al., 2009]. 54

5.4 Schematic drawing of the beam line used for this experiment at NSCL. . . . 55

5.5 Drawing of the detectors at the focal plane of the S800 spectrometer. (Figure modified from [Yurkon et al., 1999]). 57

6.1 Energy-calibrated gamma spectra of the ^{226}Ra source. The horizontal axis shows the energy in keV. The two spectra are measured by the central contacts of SeGa detectors number 1 and 2. 61
6.2 Energy-calibrated gamma spectra of the ^{226}Ra source, measured by the segments of detector number 1. The horizontal axis shows the energy in keV. The four spectra, from top to bottom, show Fold 1, 2, 3, and 4 events. . . . 63
6.3 Schematic drawing of the mask used for the calibration of CRDCs. 64
6.4 Upper panel: raw spectrum of counts per channel in the X direction obtained from a calibration run. Lower panel: the rectangles indicate the group of channels used in the calibration procedure. 66
6.5 Reconstructed 2D image of the beam passing through the mask, after calibration. The horizontal and vertical axes show the X and Y position in mm, respectively. The upper image corresponds to the calibration mask in front of the first CRDC, while the lower image corresponds to the calibration mask in front of the second CRDC. 67
6.6 Energy loss of unreacted ^{71}Cu ions in segments number 1, 2 and 3 of the ion chamber. The upper and lower plots show the spectra before and after the gain-matching procedure. The energy on the horizontal axis is expressed in arbitrary units. 68
6.7 TOF spectra used for the particle identification of the ^{71}Cu incoming beam. The time of flight on the horizontal axis is expressed in arbitrary units. . . 70
6.8 Uncorrected TOF-angle plot for one of the experimental runs. The TOF is on the horizontal axis, and the angle in the X direction is on the vertical axis. This figure shows that there is a correlation between the two quantities. 72
6.9 Corrected TOF-angle plot for the same experimental run as in Figure 6.8. The corrected TOF is on the horizontal axis, and the angle in the X direction is on the vertical axis. 74

6.10 Particle ID plot for runs without plunger, S800 set for ^{71}Cu. The black closed curve is the two-dimensional gate used to select ^{71}Cu. 74
6.11 Particle ID plot for runs with target only, S800 set for ^{71}Cu. The black closed curve is the two-dimensional gate used to select ^{71}Cu. 75
6.12 Particle ID plot for runs with plunger, S800 set for ^{71}Cu. The black closed curve is the two-dimensional gate used to select ^{71}Cu. 75
6.13 Particle ID plot for runs with plunger, S800 set for ^{70}Ni. The black closed curve is the two-dimensional gate used to select ^{70}Ni. 76
6.14 Particle ID plot for runs without plunger, S800 set for ^{73}Cu. The black closed curve is the two-dimensional gate used to select ^{73}Cu. 76
6.15 Particle ID plot for runs with target only, S800 set for ^{73}Cu. The black closed curve is the two-dimensional gate used to select ^{73}Cu. 77
6.16 Particle ID plot for runs with plunger, S800 set for ^{73}Cu. The black closed curve is the two-dimensional gate used to select ^{73}Cu. 77
6.17 Particle ID plot for runs with plunger, S800 set for ^{72}Ni. The black closed curve is the two-dimensional gate used to select ^{72}Ni. 83
6.18 ^{70}Ni gamma spectra with target only. Blue: forward array. Green: backward array. The spectra are Doppler-corrected with $\beta = 0.369$. 84
6.19 Doppler-corrected ^{70}Ni gamma spectra with plunger, d=10 mm. Blue: forward array. Green: backward array. The spectra are Doppler-corrected with $\beta = 0.369$. 85
6.20 Doppler-corrected ^{70}Ni gamma spectra with plunger, d=0.1 mm. Blue: forward array. Green: backward array. The spectra are Doppler-corrected with $\beta = 0.369$. 86

6.21 Doppler-corrected ^{70}Ni gamma spectra measured by the forward array. Upper panel: d=0.1 mm. Middle panel: d=1 mm. Lower panel: d=10 mm. The yellow shaded region shows the position of the $2^+ \rightarrow 0^+$ peak at the correct energy, corresponding to gammas emitted before the degrader. The blue shaded region shows the shifted peak, corresponding to gammas emitted after the degrader. 87
6.22 Schematic drawing of the beam at the focal plane. The angles Ata and max Ata are measured in the dispersive plane. An analogous drawing would illustrate the angles Bta and max Bta, measured in the non-dispersive plane. 88
6.23 Simulation (in blue) and measurement (in red) of the unreacted ^{71}Cu beam going through the plunger. Upper left: Ata (angle with respect to optical axis in the dispersive plane). Upper right: Bta (angle with respect to optical axis in the non-dispersive plane). Lower left: Y (position in the non-dispersive direction). Lower right: Dta (difference in kinetic energy with respect to the particles in the central trajectory). 89
6.24 Gamma spectra for ^{70}Ni, with d=10 mm. The measurement is in red, and the simulation is in blue. Upper panel: forward ring. Lower panel: backward ring. 90
6.25 Gamma spectra for ^{70}Ni, with d=1 mm. The measurement is in red, and the simulation is in blue. Upper panel: forward ring. Lower panel: backward ring. 91
6.26 Gamma spectra for ^{70}Ni, with d=0.1 mm. The measurement is in red, and the simulation is in blue. Upper panel: forward ring. Lower panel: backward ring. 92
6.27 Gamma spectra for ^{70}Ni, with d=0.1 mm. The measurement is in red, and the simulation is in blue. Upper panel: forward ring. Lower panel: backward ring. The simulation corresponds to a half life of 1 ps for the 2^+ state. . . . 93

Chapter 1

Introduction

Studying the properties of nuclei far from stability is essential for our understanding of the nuclear phenomena. It is important to gather experimental data that can be compared to theoretical predictions, so that the accuracy of different nuclear models can be assessed. Both proton-rich and neutron-rich exotic nuclei have astrophysical importance. Knowing their properties is important for the simulation of astrophysical nucleosynthesis processes, in particular the rp-process and the r-process.

The first experiment described in this work explored proton-rich nuclei in the region of the nuclear chart directly above doubly magic ^{100}Sn. Its goal was to detect the alpha decay of ^{112}Cs and also gain more information about its neighbors. The second experiment described in this work focused on neutron-rich Nickel isotopes, close to doubly magic ^{78}Ni.

Chapter 2 contains an introduction on the ^{100}Sn region, and in particular on the alpha decay of those nuclei, explaining the reasons for trying to detect the alpha decay of ^{112}Cs. The setup of the ^{112}Cs experiment is described in Chapter 3. In Chapter 4 we discuss the data analysis and results of the ^{112}Cs experiment. Chapter 5 contains the motivation for the ^{70}Ni and ^{72}Ni experiment, and a short description of the experimental setup. Chapter 6 shows the data analysis and preliminary results for that experiment.

My contributions to the work presented in this dissertation include the following tasks:

I helped set up the cesium experiment, I participated in running it, and I analyzed the data. To do so, I modified the existing analysis code and added several subroutines to it. I wrote a manuscript (in collaboration with the other co-authors) based on the results of this experiment, that has been published Physical Review C. I participated in running the nickel experiment, performed Monte Carlo simulations, and analyzed the data. The experimental data will result in a publication.

Chapter 2

Alpha decay of proton-rich nuclei in the ^{100}Sn region

Tin-100, with $Z = N = 50$, is the heaviest known doubly magic nucleus with the same number of protons and neutrons. That renders the region of the nuclide chart above ^{100}Sn particularly interesting, because protons and neutrons outside the closed shells occupy the same single-particle states. Thanks to these features, there is a small island of alpha emitters in this region. Figure 2.1 shows the chart of nuclides, color-coded to indicate the main decay mode of each nucleus. The small island of alpha emitters is visible just beyond the $Z = 50$ and $N = 50$ lines. The nuclei above ^{100}Sn are expected to be the ideal subjects for the so-called superallowed alpha decay [Macfarlane and Siivola, 1965, Liddick et al., 2006, Darby et al., 2010], because of the vicinity of the double-closed shell. Another interesting feature is the presence of the proton drip-line, so both alpha decay and proton decay can occur in this region [Kirchner et al., 1977, Page et al., 1994a]. Cesium-112 ($Z = 55$, $N = 57$) is a known proton emitter, with half-life $T_{\frac{1}{2}} = 500 \pm 100\,\mu$s [Page et al., 1994b]. In this work we searched for an alpha decay branch of ^{112}Cs.

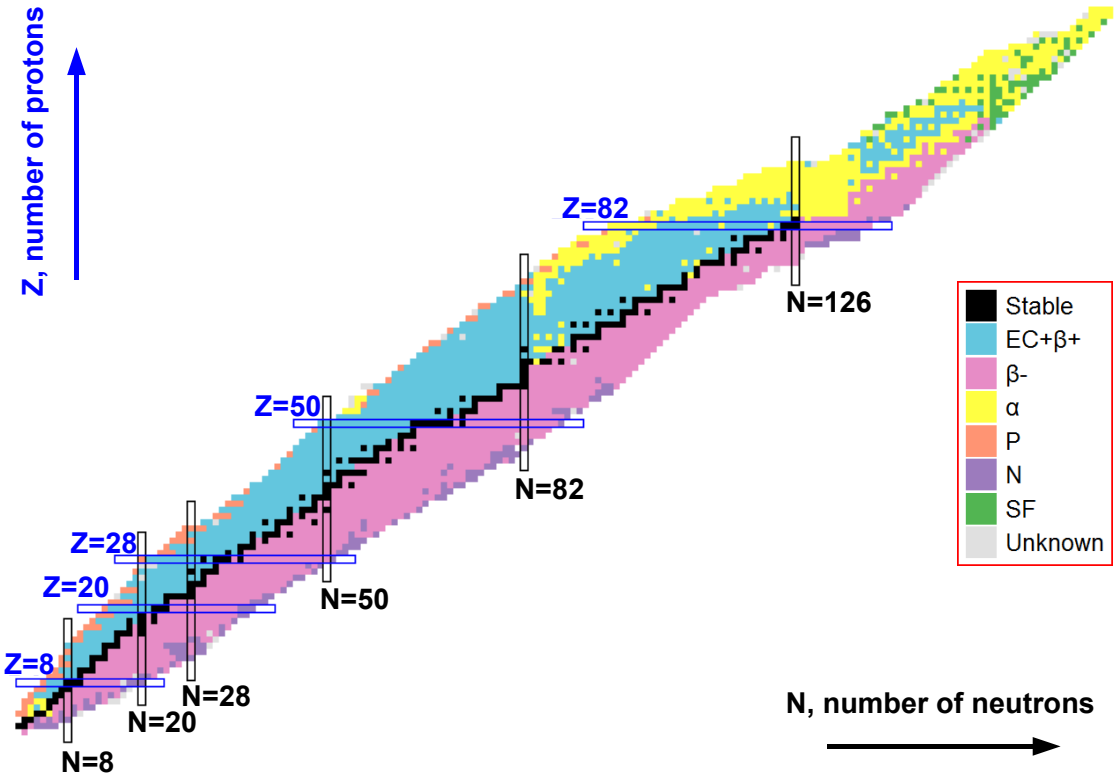


Figure 2.1: Chart of nuclides [BNL, 2011]. The color map illustrates the main decay mode for each nucleus.

2.1 Alpha decay

When doing experiments on alpha decay, the main quantities that can be measured are the energy of the alpha particle, the total half-life $\mathrm{T}_{\frac{1}{2}}$ and the alpha branching ratio b_α. The energy of the alpha particle and the recoil energy of the daughter nucleus give the decay energy Q_α. The alpha decay probability per unit time λ_α is defined as

$$\lambda_\alpha = b_\alpha \left(\frac{\ln 2}{T_{\frac{1}{2}}} \right). \tag{2.1}$$

In the Gamow model of alpha decay it is assumed that the alpha particle is preformed inside the nucleus, then it tunnels through the potential barrier. Within this model, the alpha decay probability can be written as

$$\lambda_\alpha = S^\alpha f P \tag{2.2}$$

where S^α is the preformation probability, f is the frequency with which the alpha particle hits the barrier, and P is the barrier penetration probability, given by the following expression

$$P_\alpha = \exp\left(-2 \int_{R_i}^{R_a} \sqrt{\frac{2M_\alpha \left(U(R) - Q_\alpha + \delta E_{scr} \right)}{\hbar^2}}\, dR \right). \tag{2.3}$$

U(R) is the potential as a function of the radial position R, R_i and R_a are the inner and outer classical turning points of the alpha particle in the potential well, M_α is the mass of the alpha particle, and δE_{scr} is the energy correction due to the electron screening of the nucleus. If the angular momentum l of the alpha particle is not zero, the centrifugal term U_c, given by the expression

$$U_c = \frac{l\,(l+1)\,\hbar^2}{2MR^2} \tag{2.4}$$

is added to the potential U(R). The barrier penetration probability strongly depends

on the energy of the alpha particle, so the alpha decay probability λ_α also has a strong dependence on the energy. That dependence is removed in the alpha decay reduced width δ^2, which is a parameter defined as

$$\delta^2 = \frac{h\lambda_\alpha}{P} = S^\alpha f h \tag{2.5}$$

where h is Planck's constant. A useful dimensionless parameter is W_α, the reduced width relative to ^{212}Po, defined as

$$W_\alpha = \frac{\delta^2}{\delta^2\,(^{212}Po)}. \tag{2.6}$$

The parameter W_α is usually called just alpha reduced width and is used as a way to quantify the role of the alpha particle preformation, a difficult problem to model [Mang, 1960].

2.2 Experimental studies of alpha decay near ^{100}Sn

The alpha emitters near ^{100}Sn have been an object of experimental studies for decades, since the discovery of this new region of alpha radioactivity reported in [Macfarlane and Siivola, 1965]. In this pioneering work, the authors postulated the existence of superallowed alpha decays, characterized by an unusually large reduced width. An evidence for such decays has been seen in the decay of ^{106,105}Te isotopes [Janas et al., 2005, Liddick et al., 2006]. New alpha emitters were discovered among light Te, I, Xe, and Cs isotopes (see for example [Schardt et al., 1979,Schardt et al., 1981,Heine et al., 1991,Page et al., 1994a,Liddick et al., 2006, Mazzocchi et al., 2007]). Technical progress over the years allowed the measurement of properties of those nuclei with growing accuracy. By measuring Q values and relating to known isotopes, it is possible to determine the mass of nuclei far from stability. Table 2.1 summarizes the properties of the known alpha emitters above ^{100}Sn.

One of the most interesting discoveries was the alpha decay of ^{109}I [Mazzocchi et al.,

Table 2.1: Properties of alpha emitters above ^{100}Sn: half-life ($T_{1/2}$), branching ratio (b_α), and energy (E_α). Reference (a) [Liddick et al., 2006], (b) [Schardt et al., 1981], (c) [Page et al., 1994a], (d) [Schardt et al., 1979], (e) [Heine et al., 1992], (f) [Audi et al., 2003], (g) [Kirchner et al., 1977], (h) [Dombrádi et al., 1995], (i) [Mazzocchi et al., 2007], (j) [Tidemand-Petersson et al., 1985], and (k) [Roeckl et al., 1980].

Nucleus	$T_{1/2}$ (s)	b_α (%)	E_α (keV)	References
^{105}Te	$(620 \pm 70)10^{-9}$	~ 100	4603 ± 5	(a)
^{106}Te	$(60 \pm 30)10^{-6}$	~ 100	4128 ± 9	(b)(c)
^{107}Te	$(3.1 \pm 0.1)10^{-3}$	70 ± 30	3861 ± 5	(b)(d)(e)
^{108}Te	2.1 ± 0.1	49 ± 4	3317 ± 4	(c)(d)(e)
^{109}Te	(4.6 ± 0.3)	3.9 ± 1.3	2624 ± 15	(b)(e)(f)
^{110}Te	18.6 ± 0.8	~ 0.003	2624 ± 15	(b)(f)(g)
^{108}I	$(36 \pm 6)10^{-3}$	91 ± 15	3947 ± 5	(c)
^{109}I	$(103 \pm 5)10^{-6}$	$(1.4 \pm 0.4)10^{-4}$	3774 ± 20	(h)(i)
^{110}I	0.65 ± 0.2	17 ± 4	3456 ± 5	(b)(e)
^{111}I	2.5 ± 0.2	~ 0.088	3174 ± 10	(e)(f)(g)
^{112}I	3.42 ± 0.11	~ 0.0012	2880 ± 30	(b)(f)(j)
^{113}I	6.6 ± 0.2	$\sim (3.3)10^{-7}$	2610 ± 40	(b)(f)
^{109}Xe	$(13 \pm 2)10^{-3}$	~ 100	4062 ± 7	(a)
^{110}Xe	~ 0.2	~ 0.5	745 ± 15	(b)(e)
^{111}Xe	0.74 ± 0.20	8 ± 8	3580 ± 30	(b)(c)
^{112}Xe	2.7 ± 0.8	0.9 ± 0.8	3216 ± 7	(c)(f)
^{113}Xe	2.74 ± 0.08	~ 0.011	2985 ± 15	(d)(f)(j)
^{114}Cs	0.57 ± 0.02	0.018 ± 0.006	3226 ± 30	(k)

2007], already known as a proton emitter. At present ^{109}I is the only nucleus in this region to possess a proton decay branch and an alpha decay branch. The fact that two different decay chains (alpha-proton and proton-alpha) could in principle start from ^{109}I and lead to ^{104}Sn, and the fact that three out of those four decays had known energies, was used to determine the energy separating ^{104}Sn from ^{105}Sb, i.e. the proton separation energy of ^{105}Sb [Mazzocchi et al., 2007].

Another fascinating discovery was the alpha decay chain ^{109}Xe $\rightarrow$ ^{105}Te $\rightarrow$ ^{101}Sn, detected for the first time [Liddick et al., 2006]. The decay of ^{105}Te leads to ^{101}Sn, with only one nucleon outside the closed shells. It has a half-life of 620 ± 70 ns and can be considered the first example of superallowed alpha decay [Liddick et al., 2006, Darby et al., 2010].

2.3 The ^{112}Cs experiment

Among the candidates for having both alpha and proton decay branches, we chose to investigate $^{112}_{55}$Cs$_{57}$. It is a known proton emitter; its half-life $T_{\frac{1}{2}} = 500 \pm 100\,\mu$s and proton energy 807 ± 7 keV were determined from the observation of about 20 decay events [Page et al., 1994b]. In analogy with the approach followed for the investigation of ^{109}I alpha decay [Mazzocchi et al., 2007], the measurement of the Q_α value for ^{112}Cs would determine indirectly the proton separation energies of ^{104}Sb and ^{108}I, as shown in Figure 2.2. An upper limit for $Q_p(^{108}\mathrm{I})$, which implies an upper limit for $Q_p(^{104}\mathrm{Sb})$, was deduced in [Page et al., 1994a]. Adopting those upper limits, a lower limit of 3.83 MeV can be estimated for the ^{112}Cs Q_α value.

2.4 Astrophysical interest

Simulations of astrophysical nucleosynthesis processes require knowlege of masses, decay energies and reaction rates. Many of these quantities are unknown for nuclei far from

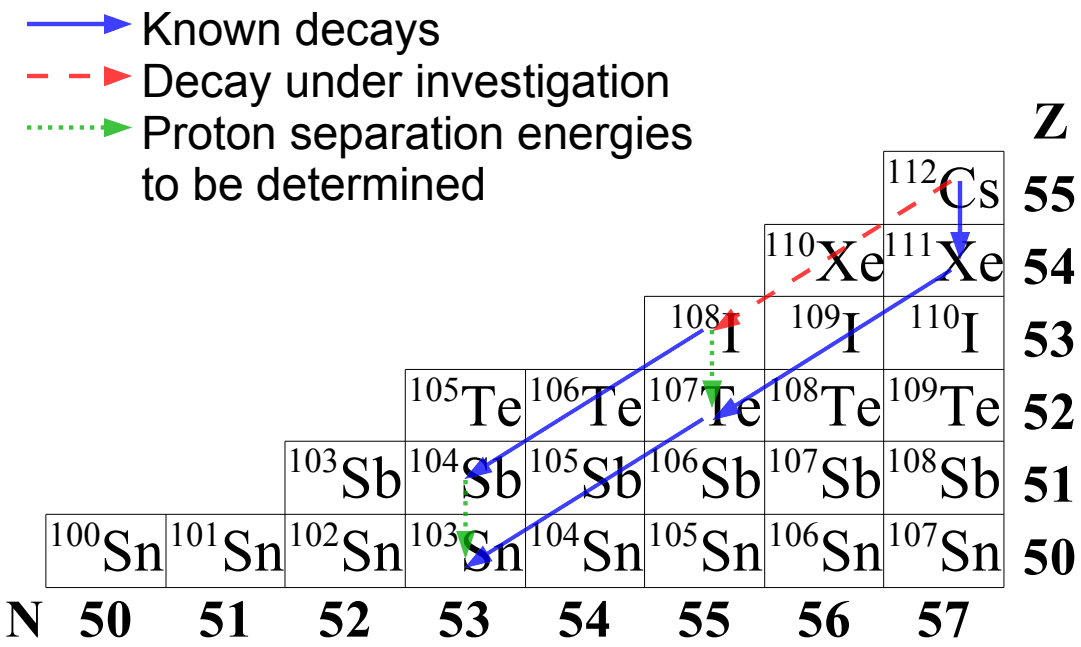


Figure 2.2: Portion of the nuclide chart above ^{100}Sn. The arrows show decay chains starting at ^{112}Cs.

stability, so simulations have to rely on theoretical predictions and assumptions. It has been shown that nucleosynthesis simulations based on different nuclear mass models can lead to considerably different results, particularly regarding the time scale of the process involved, and the final composition of the ashes when the nucleosynthesis process reaches its final equilibrium state [Schatz et al., 1998, Clement et al., 2003]. It is important to gather experimental data to be input in simulations instead of theoretical estimates, so that the simulations can be more accurate.

The proton separation energy of ^{104}Sb is especially interesting because of its relevance for the astrophysical rp-process [Wallace and Woosley, 1981]. The rp-process is a nucleosynthesis process occurring at temperatures higher than 10^8 K and densities higher than $0.1\,\mathrm{g/cm^2}$. Possible sites for this process are supermassive stars ($M > 10^5 M_\odot$), accreting neutron stars, red giants with neutron core, nova and supernova outbursts.

The rp-process consists of rapid successive proton captures and β^+ decays. It starts from helium-burning products and develops approximately along the N = Z line, with the overall effect of burning hydrogen into heavier proton-rich elements. Its path on the nuclide chart is shown in Figure 2.3.

Proton capture can occur for the nucleus (N,Z) if the resulting nucleus (N,Z+1) is stable against proton decay, and the proton capture reaction competes favorably with the (γ, p) disintegration of the (N,Z+1) nucleus. Proton capture may even occur when the resulting nucleus is unstable against proton decay, provided that its partial half-life for proton decay is sufficiently long [Schatz et al., 1998]. When proton capture is not possible, β^+ decay usually occurs, followed by more proton captures and β^+ decays.

According to calculations, the rp-process terminates when ^{107}Te is reached. Then ^{107}Te undergoes (γ, α) photodisintegration to ^{103}Sn, thus forming a loop that terminates the process in a Sn-Sb-Te cycle [Schatz et al., 2001].

Figure 2.4 shows the predicted termination of the rp-process, together with a possible alternative. If ^{104}Sb turns out to be sufficiently proton-bound, the rp-process could proceed

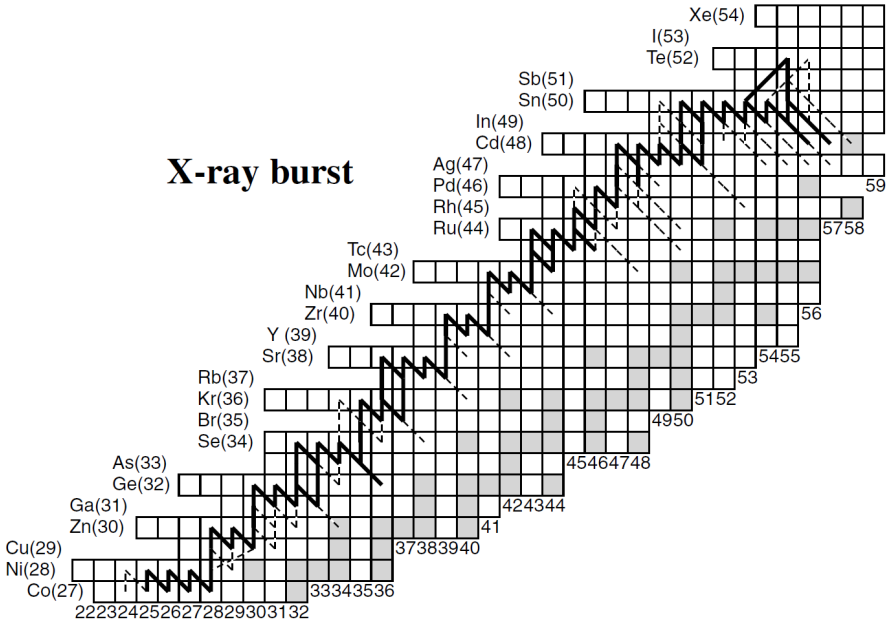


Figure 2.3: Path of the rp-process during an X-ray burst. Continuous lines represent reaction flows of more than 10% of the reaction flow through the 3α reaction, while dashed lines represent reaction flows of 1%-10% [Schatz et al., 2001].

with proton captures from ^{103}Sn to ^{104}Sb and ^{105}Te, then end in a different loop with alpha decay of ^{105}Te to ^{101}Sn. That earlier onset of the Sn-Sb-Te cycle would enhance the rate of hydrogen burning and helium production.

Simulations were performed to calculate the value of proton separation energy S_p necessary for proton capture to occur at a significant rate. Figure 2.5 shows those results. A significant Sn-Sb-Te cycle can be established if the corresponding branching ratio is at least 10%, which corresponds to a Q_p value of at most -0.51 MeV for ^{104}Sb. A measurement of $Q_p(^{104}\text{Sb})$ will determine how much of the reaction flow can reach this point. It has already been shown that the Sn-Sb-Te cycle can not start at ^{105}Sb, because ^{105}Sb is not sufficiently proton-bound [Mazzocchi et al., 2007].

Recent measurements [Elomaa et al., 2009] indicate that the Sn-Sb-Te cycle is weaker than expected, since only a few percent of the reaction flow may branch into the Sn-Sb-Te cycle. However it would still be important to acquire more accurate information on the proton separation energies of the nuclei in this region.

2.5 Odd-even effect

Figure 2.6 shows the Q values for proton emission for some odd-Z isotopes close to the proton drip-line. In most cases Q_p decreases as N increases. Q_p for ^{112}Cs is smaller than Q_p for ^{113}Cs because of nucleon pairing forces. The odd proton pairs up with the odd neutron in ^{112}Cs, therefore it is more bound than in ^{113}Cs. Analogously, Q_p values for ^{104}Sb and ^{108}I are expected to be smaller than for ^{105}Sb and ^{109}I. If that is correct, Q_α for ^{112}Cs is expected to be larger than 3.98 MeV, so its measurement could establish the magnitude of this effect. According to Figure 2.6 it appears that the odd-even staggering effect is stronger for the I and Cs isotopes than for the Sb isotopes, and stronger beyond the proton drip-line. A similar effect has been observed for proton emitters in the Ho [Rykaczewski et al., 1999] and Lu [Sellin et al., 1993] regions.

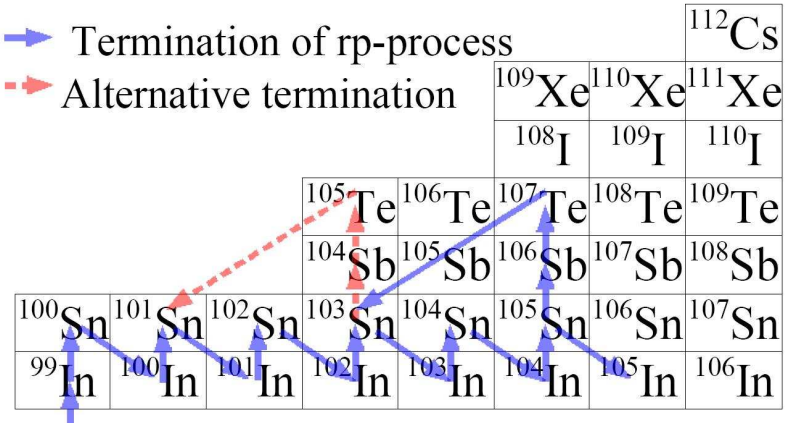


Figure 2.4: Termination of the rp-process. Continuous arrows represent the calculated path [Schatz et al., 2001]. Dashed arrows represent an alternative path.

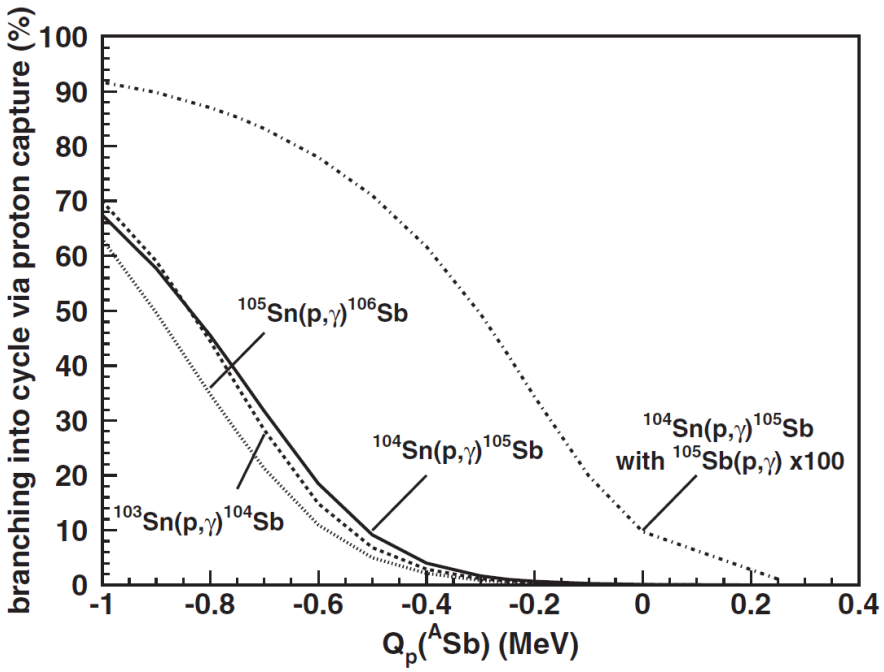


Figure 2.5: Branching of the rp-process into proton capture at various Sb isotopes as a function of $Q_p = -S_p$ [Mazzocchi et al., 2007].

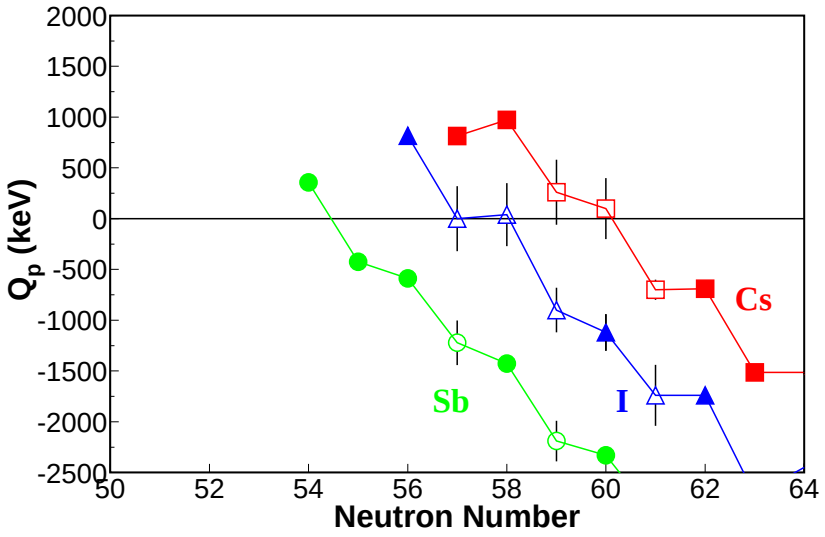


Figure 2.6: Q_p values for neutron-deficient Sb (Z = 51), I (Z = 53) and Cs (Z = 55) isotopes. Full symbols represent measured values [Blank and Borge, 2008] while open symbols represent extrapolations [Audi et al., 2003].

Chapter 3

The ^{112}Cs experiment

3.1 The Holifield Radioactive Ion Beam Facility

The experiment was performed at the Holifield Radioactive Ion Beam Facility (HRIBF) at Oak Ridge National Laboratory. A drawing of the facility is shown in Figure 3.1. HRIBF is one of the few facilities capable of producing intense beams of accelerated ions, stable or radioactive. The tandem accelerator at HRIBF [Bair et al., 1975, Jones, 1981], commissioned in 1980, is the electrostatic accelerator with the highest controlled voltage in the world. It reached 32 MV in tests performed before the installation of acceleration tubes [Jones, 1981], and 25.5 MV with accelerated beam [Jones et al., 1989].

3.2 Beam and reaction target

A ^{58}Ni beam with energy E = 250 MeV impinged on a ^{58}Ni target, producing ^{112}Cs ions via the fusion-evaporation reaction $^{58}\mathrm{Ni}\left(^{58}\mathrm{Ni}, \mathrm{p3n}\right)^{112}\mathrm{Cs}$. The target, 300 μg/cm^2 thick, was mounted on a rotating support, so that it could sustain higher beam intensities with respect to a stationary target. Typical beam intensities used ranged between 20 and 40 part·nA.

3.3 The Recoil Mass Spectrometer

After the interaction of the primary beam with the target, the recoiling products were selected through the the Recoil Mass Spectrometer (RMS) [Gross et al., 2000]. Figure 3.2 shows a schematic drawing of the RMS [Ginter, 1999]. The first portion of the RMS is the Momentum Separator, which separates particles according to their momentum/charge ratio, to achieve a good suppression of the primary beam. The last portion of the RMS is the Mass Separator. Electric and magnetic dipoles separate the particles according to their mass/charge ratio A/Q. Magnetic quadrupoles and sextupoles along the beam line provide focusing of the beam and corrections to optical aberrations. They can be adjusted while monitoring the beam position and shape at the focal plane. The time of flight of the ions through the RMS is of the order of microseconds.

For this experiment the RMS was set on the following parameters: $A = 112$, $E = 113\,\mathrm{MeV}$, $Q = 29.47$. Selecting that nonexistent charge state for the central trajectory resulted in having the two charge states $Q = 29$ and $Q = 30$ with mass $A = 112$ reaching the focal plane. For some of the runs the set charge state was $Q = 30.47$, so the charge states with mass $A = 112$ arriving at the focal plane were $Q = 30$ and $Q = 31$.

Partial beam blockers can be inserted in the beam line to block some of the mass/charge states from reaching the focal plane. Two blockers can be inserted from the right and from the left, and the third can be raised between them, thus forming two separate slits where the beam can pass. The blockers themselves are usually called "slits" by experimenters, and we will follow the same convention here. The position of the lateral slits can be adjusted, and the central slit can be rotated so that it can block more or less of the beam.

Figure 3.3 shows the effect of inserting the slits in the beamline. The slits are used to keep the desired mass ($A = 112$ in this case) and eliminate others from the beam. It is apparent in Figure 3.3 that the peaks are distinguishable but they partially overlap, so it is not possible to eliminate all of the unwanted contaminants.

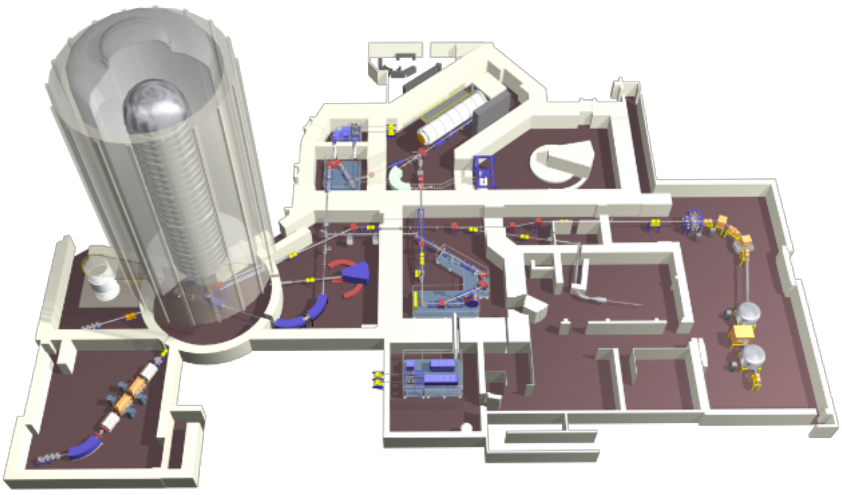


Figure 3.1: Schematic drawing of the Holifield Radioactive Ion Beam Facility.

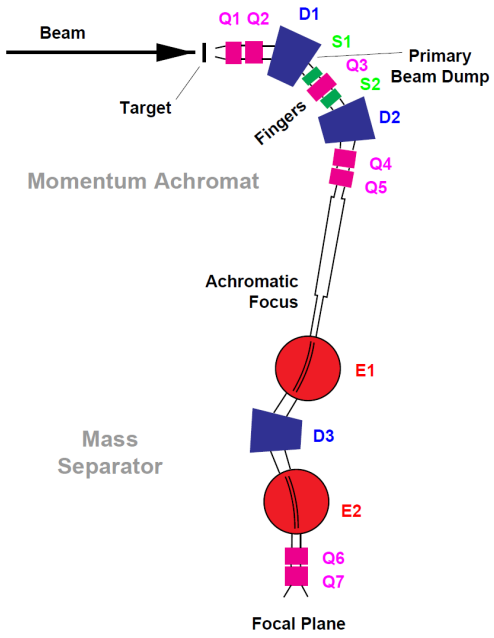


Figure 3.2: Schematic drawing of the RMS [Ginter, 1999].

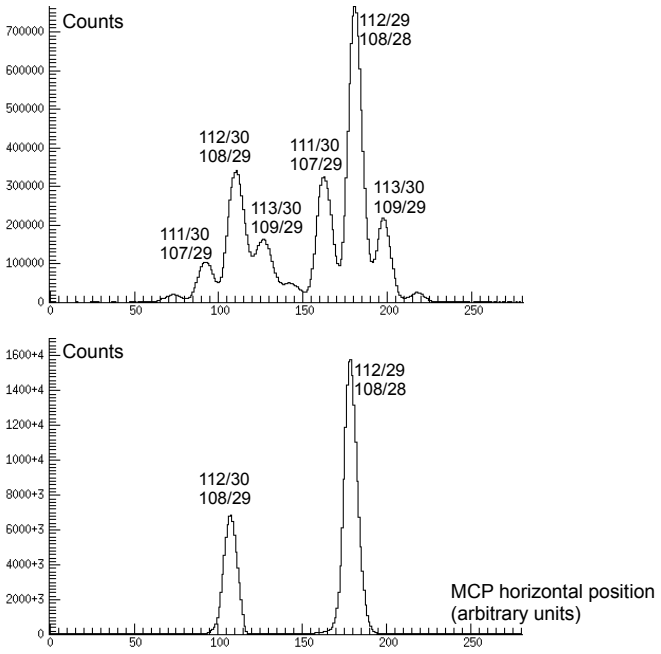


Figure 3.3: A/Q spectra of ions going through the MCP foil. The horizontal position measured by the MCP is on the horizontal axis and corresponds to the mass/charge ratio. Upper panel: no slits. Lower panel: with slits. The labels next to the peaks show the corresponding mass/charge states.

3.4 RMS focal plane detectors

At the focal plane the separated recoils passed through the large foil of the Multichannel Plate (MCP) detector system [Shapira et al., 2000] that provided a two-dimensional image of the position of the ions arriving at the focal plane. The recoils were then implanted into a Double-sided Silicon Strip Detector (DSSD).

This DSSD, shown in Figure 3.4, was the main detector used in the experiment. It is 4 cm by 4 cm, 65 μm thick and segmented in 40 horizontal strips in the front and 40 vertical strips in the back. It allowed detection of the incoming ions as well as their decay products. The energy of the recoil ions at the focal plane of the RMS was of the order of 100 MeV, while the energy of the decay products ranged between 0.8 MeV for protons and several MeV for alpha and beta-delayed alpha and proton particles. Thin layers of aluminum and mylar (308 and 354 μg/cm^2 thick, respectively) were placed in front of the DSSD as degraders, to reduce the energy of incoming ions to allow it to fall in the range of the DSSD electronics. We performed energy loss calculations [Tarasov and Bazin, 2004, Ziegler et al., 1985] to ensure that the energy loss was adequate.

The detection setup was completed by a series of veto detectors, that allowed the suppression of particles escaping the DSSD detector with good efficiency [Karny et al., 2008]: upstream a box consisting of 4 silicon detectors (Si-box) surrounded the DSSD, while a 5 mm-thick Si(Li) detector was placed just behind it in close geometry. The DSSD-Si box assembly is shown in Figure 3.5. Figure 3.6 is a schematic drawing of the DSSD and veto detectors. Decay events that escaped the DSSD, like for examples number 2, 3, and 4 in the figure, could be identified by the presence of a signal generated in other detectors. Alpha particles and protons emitted by nuclei involved in this experiment were expected to be stopped inside the DSSD, thus releasing all of their energy there, with a probability ranging between 81% and 96%, depending on their energy. The MCP was also used as a veto detector, as explained in Section 4.2.

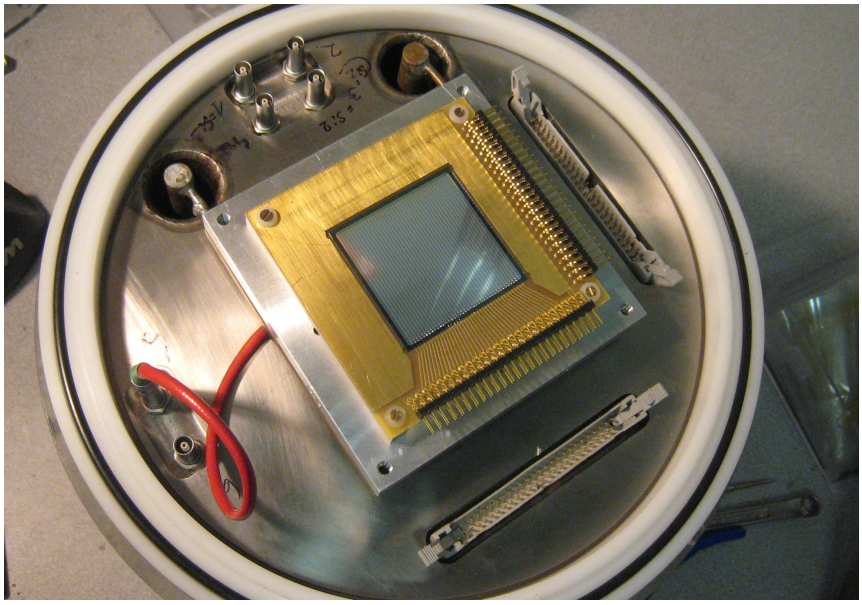


Figure 3.4: Picture of the DSSD.

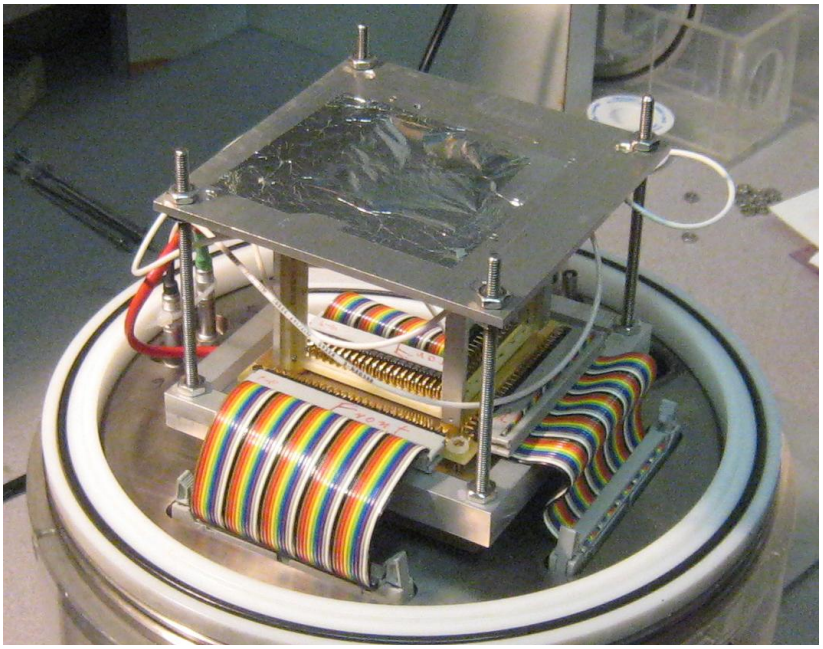


Figure 3.5: Picture of the DSSD-Si box assembly. The energy degrader is visible on top of the silicon box. The DSSD is located underneath the box in this view.

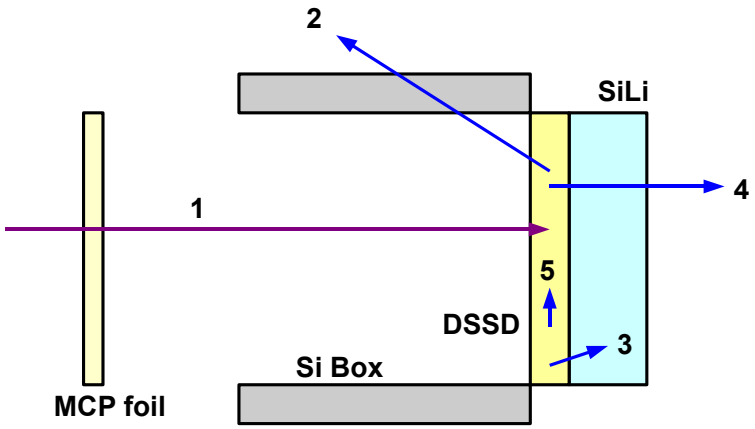


Figure 3.6: Schematic view of the DSSD and veto detectors. Arrow number 1 represents the trajectory of an ion detected by the MCP and then implanted in the DSSD. Arrows number 2, 3, and 4 represent the trajectories of particles escaping the DSSD. Arrow number 5 represents the trajectory of a particle not escaping the DSSD.

3.5 Digital data acquisition system

Data from all detectors were collected by digital signal processing electronics [Grzywacz, 2003]. Figure 3.7 shows a schematic drawing of the electronic chain. The preamplifiers were directly connected to DGF (Digital Gamma Finder [Hubbard-Nelson et al., 1999]) modules. Figure 3.8 shows a picture of one of the DGF modules used in the experiment. Each event was time-stamped and registered with its amplitude.

The energy deposited in the DSSD by each event was used to discriminate between implanted ions, with energies of the order of 100 MeV, and particles emitted by the ions, with energies of less than 5 MeV. In the offline software analysis of the data, decay events were correlated in time and space with the implanted ions.

New features were added to the code during the data analysis for this experiment. Some of them were needed to correlate each DSSD decay with other decays, and with energy depositions in the other detectors, if any. In particular, the multi-generation correlation analysis for the decay events was implemented up to the 4^{th} generation. Other additions to the code were used to reduce the background, and will be discussed in Section 4.2.

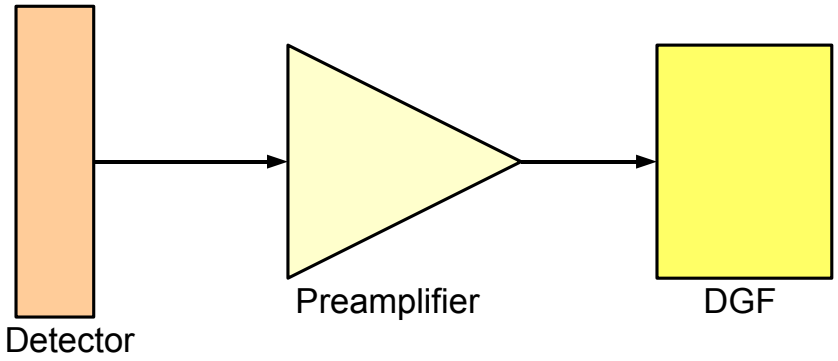


Figure 3.7: Schematic drawing of the electronic chain from the detector to the DGF module.

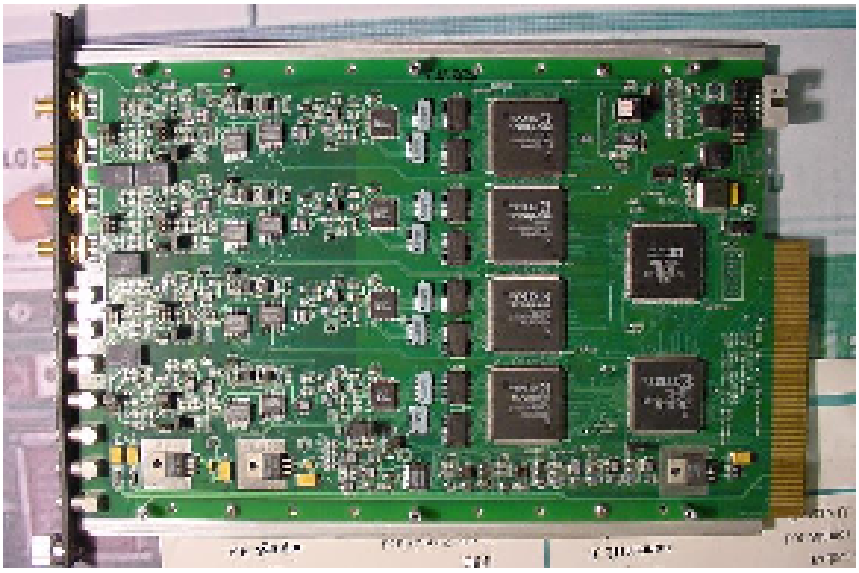


Figure 3.8: Picture of the DGF module.

Chapter 4

Data analysis and results of the ^{112}Cs experiment

4.1 Calibration of the DSSD

The first step for DSSD calibration is the gain matching of the strips. The gain matching algorithm is based on the fact that energy detected in the front of the DSSD should be equal to the energy detected in the back, within the strips' energy resolution (about 40 keV). It is not necessary to know the energy of the particles detected, so runs with an alpha calibration source or normal measurement runs can be used. The calibration program scans the whole input data several times, slightly adjusting the calibration parameters at each event. The calibration parameters of each strip converge to their optimal values, and self-consistent gain matching is achieved. The algorithm was already used successfully in previous experiments. After the gain matching procedure, corresponding peaks in all of the DSSD strips appear more aligned, as shown in Figure 4.1.

For the energy calibration in keV we used the position of the ^{108}Te alpha peak, which is the most intense in our energy spectra; ^{108}Te was present in the beam as a contaminant. We assumed a linear response to the energy and calculated a multiplication parameter for

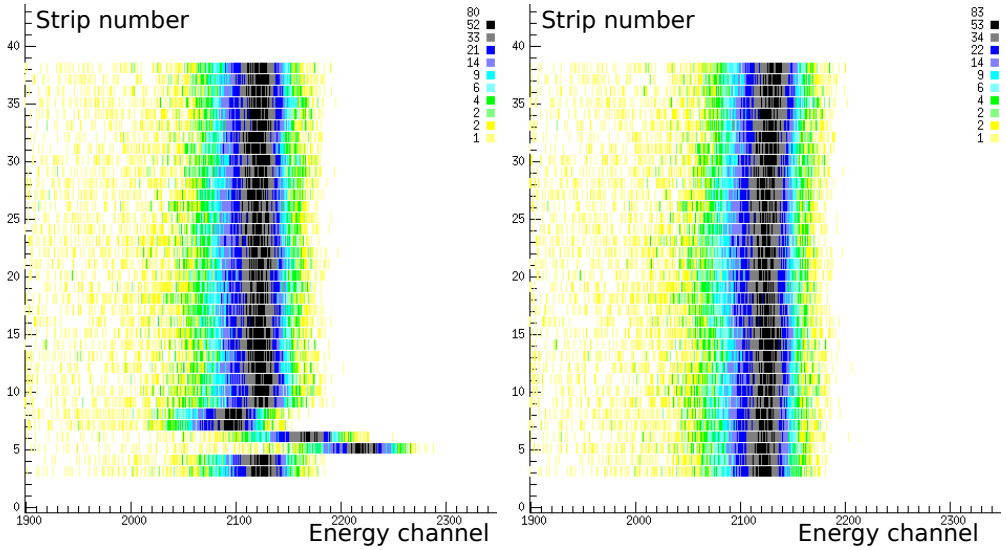


Figure 4.1: Energy spectra before (left) and after (right) the gain matching procedure. The channel number, corresponding to energy, is on the horizontal axis. The front strip number is on the vertical axis.

each strip. The response of the DSSD varies over time, mainly due to radiation damage, so the gain matching and energy calibration parameters were calculated specifically for each run (or small group of runs).

In the data acquisition for this experiment a short pulse integration time (4μs) was chosen. While that may have a negative impact on noise and energy resolution, it has the advantage of allowing higher rates, with shorter dead time (of about $10\,\mu$s for each strip in this case). The capability of acquiring data at high rates was essential, in order to minimize the risk of missing the alpha decay of ^{112}Cs.

The short integration time affected the baseline restoration in the preamplifier. Pulses that arrived at the preamplifier when the baseline was not yet restored have a lowered amplitude, so their energy was underestimated. This effect is apparent for example in the upper panel of Figure 4.2, showing a time-energy spectrum for protons detected in the DSSD. These protons were emitted by ^{112}Cs and ^{109}I, as will be discussed in Section 4.4.1. The lower panel in Figure 4.2 shows an analytical function of time and energy fitted to the data. The function was designed to reproduce the deviation of the detected energy from the true energy as a function of time, a gaussian broadening of the energy line, and the time decay constants for the protons. This function was fitted to the data, then used to calculate the appropriate time-dependent energy correction to be applied to the decays.

Figure 4.3 shows a time-energy spectrum for protons after the energy correction. The latest measurements in this experiment were performed using new preamplifiers with a faster baseline restoration system, able to completely restore the baseline as soon as $10\,\mu$s after each pulse. The energy was measured correctly even at short times in those measurements, so it was not necessary to apply any time-dependent energy correction when the new preamplifiers were used.

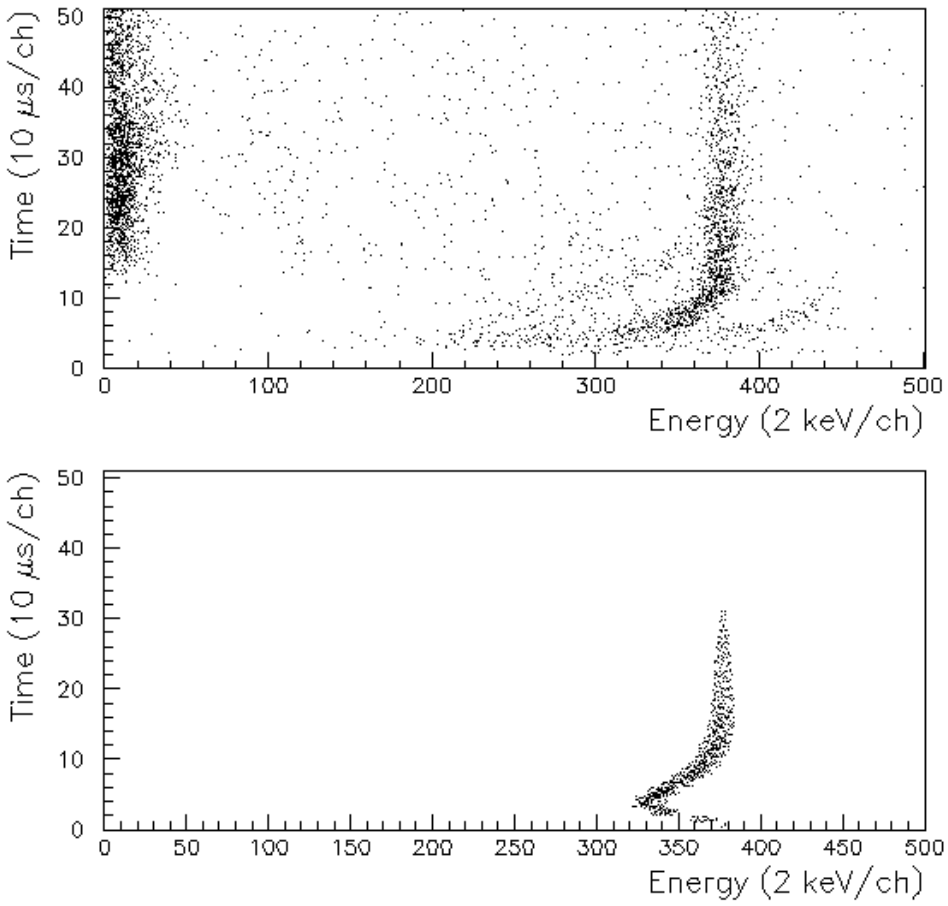


Figure 4.2: Upper panel: time-energy spectrum of decays in the DSSD. Lower panel: analytical function used to fit the data points. The function is evaluated on a grid corresponding to the energy and time channels.

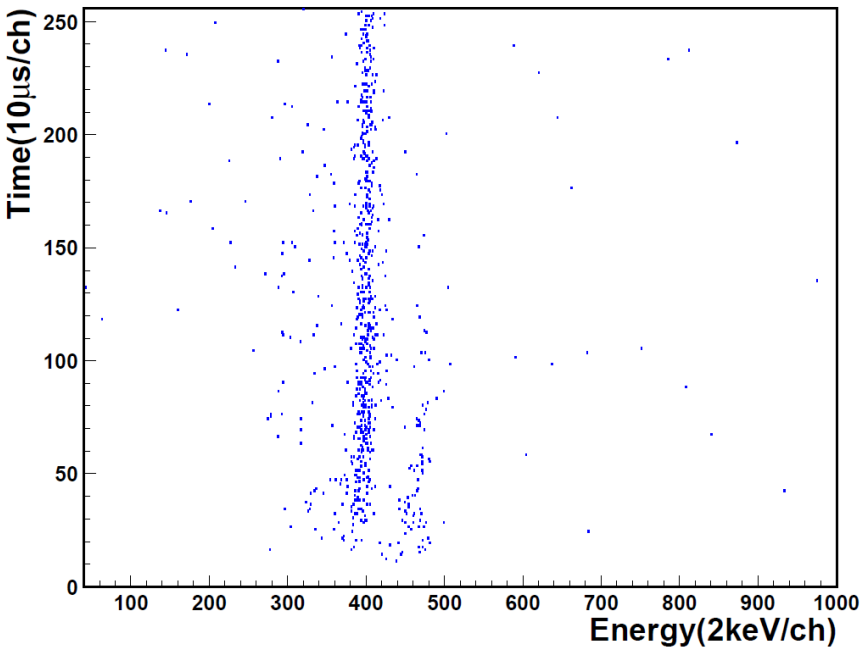


Figure 4.3: Time-energy spectrum of protons after applying the time-dependent energy correction.

4.2 Background reduction

Background radiation can come from cosmic rays, other environmental radioactivity, and contaminants in the beam. There are also sources of background that are due to the detectors themselves, and to the methods used for the data analysis.

Background reduction is particularly important when the number of expected events is low. For example, when the alpha decay of ^{109}I was detected for the first time [Mazzocchi et al., 2007], less than 10 events were detected. That small number of events was enough to unequivocally identify the new peak because the background was remarkably low. With a higher background, the same peak would have been drowned and no longer recognizable as a peak.

We tried several methods to reduce background and isolate the alpha decay events, and in particular to find any $^{112}\text{Cs} \rightarrow {}^{108}\text{Te} \rightarrow {}^{104}\text{Sb}$ that may be present in the experimental data.

Since we are interested in α-particles and their energy, we selected the decay events that deposit all of their energy in the DSSD. We excluded events where there was an energy deposition in the DSSD in coincidence with any of these detectors: SiLi and SiBOX. In other words, we kept only the events in anticoincidence with those detectors. This excludes decay products that escaped from the DSSD and reached other detectors.

The anticoincidence with the MCP also eliminated unwanted recoil nuclei from the decay spectra. Recoils were identified by the large energy that they deposited in the DSSD (of the order of 100 MeV), while typical decay energies are smaller (lower than 5 Mev). Some recoils hit the DSSD between strips, so their energy appeared to be smaller and they could be mistakenly identified as decays. Those recoils were eliminated from the decay spectra by selecting decay events in anticoincidence with the MCP, because recoils were detected by the MCP before reaching the DSSD.

Figure 4.4 shows a coincidence spectrum before and after applying the anticoincidence condition. Each 1^{st} generation - 2^{nd} generation coincidence was kept only if both decays

satisfied the condition. This method proved to be very effective in reducing the background, while leaving the peaks almost unaffected.

When a nucleus from the beam hit the DSSD, it deposited an energy of the order of 100 MeV. The ionization in the DSSD was high enough so that charge carriers could induce signals in more than one strip on each side. That could create two signals in two different pixels at the same time. In those cases one of the signals could be mistaken for a decay, because of its lower intensity. Approximately 20% of all the first generation events initially identified as decays were in fact not decays. This was verified by checking that the event was at the same time as a recoil, and that recoil was in a neighboring strip both in the front and in the back of the DSSD. Those "false decays" were rejected.

In this experiment we are especially interested in alpha-alpha decay chains. That creates other sources of unwanted background, specific to the correlation techniques. Decay events that are detected in the same pixel could appear to be correlated even when they are not, or true correlations could be disrupted by the detection of other unrelated events in the same pixel.

The basic method to look for the ^{112}Cs $\rightarrow$ ^{108}Te $\rightarrow$ ^{104}Sb decay chain consisted in a 1^{st} generation-2^{nd} generation coincidence analysis. The generation number was counted starting from the latest recoil event in the pixel. If a new recoil event hit the same pixel, the generation number was reset. With this method, some true correlations could be lost due to another ion arriving between the first and second generation decays. This problem would be unimportant if the average time between implants in each pixel was much longer than the half lives of the decays that we want to study, but it could be significant for higher implantation rates. In our experiment the implantation rate was of about 0.45 Hz for pixels in the middle of the DSSD, and about 0.2 Hz for pixels close to the corners. The overall implantation rate was 993 Hz for the whole DSSD. The decay of ^{112}Cs and ^{108}I have half lives of $500 \pm 100\,\mu$s [Page et al., 1994b] and 36 ± 6 ms [Page et al., 1994a], respectively, so their detection should not be much affected by the implantation rate. However, we were

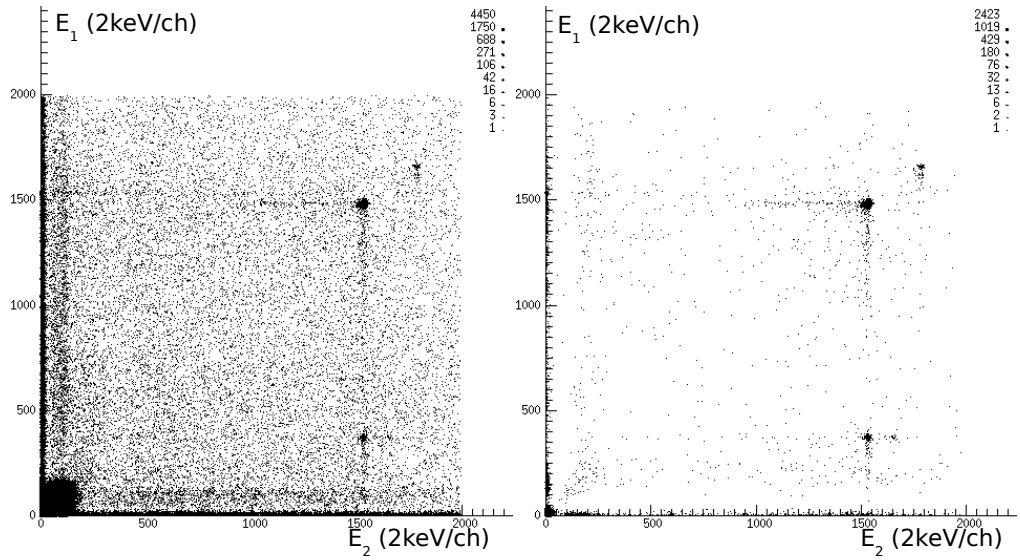


Figure 4.4: Correlation spectra of decay events. The energy of the 1^{st} generation decay is on the vertical axis, and the energy of the 2^{nd} generation decay is on the horizontal axis. The energy scales are 2 keV/ch. Left panel: no condition is applied. Right panel: the anticoincidence condition is applied.

interested also in studying ^{111}Xe, the proton daughter of ^{112}Cs, which has a half life of 0.74 ± 0.20 s, so it was decided to address the problem anyway. This was done by ignoring all implants and considering all the pairs of successive decays registered in the same pixel. Figure 4.5 shows a decay-decay spectra constructed this way. This method did recover some decay-decay correlations that would have been otherwise lost, but at the price of creating many false correlations that added greatly to the background.

For the majority of the events in the DSSD, the energy detected in the front of the detector was equal to the energy detected in the back of the detector, within a few percent. Approximately 30% of the detected decays have a front-back energy difference greater than 200 keV. By eliminating those decays, we could obtain cleaner energy spectra. Figure 4.6 shows the effect of this method on a decay-decay correlation spectrum. This method, while somewhat effective when used alone, didn't seem to add any significant advantage over the anticoincidence method.

Other attempts to get cleaner correlation spectra with reduced background include: energy cuts (to exclude events with energy below a threshold of 2500 keV and retain only alpha decays), and time cuts (to select events corresponding to specific half-lives). We concluded that for this experiment the application of the anticoincidence method was essential, because it was very effective in reducing the background while leaving the energy peaks practically unaffected; the application of other methodes in addition to it did not improve the results.

4.3 Detection efficiency

The detection efficiency of the DSSD was calculated for alphas and protons emitted within the detector itself at various energies. The implantation depth D of ^{112}Cs ions ($11.34\pm, 0.62\,\mu$m) was calculated by taking into account the energy loss through the degraders and the DSSD's dead layer. It was assumed that all alphas and protons were emitted from that depth. The range R of each particle was calculated with SRIM/TRIM simulations [Ziegler et al., 1985].

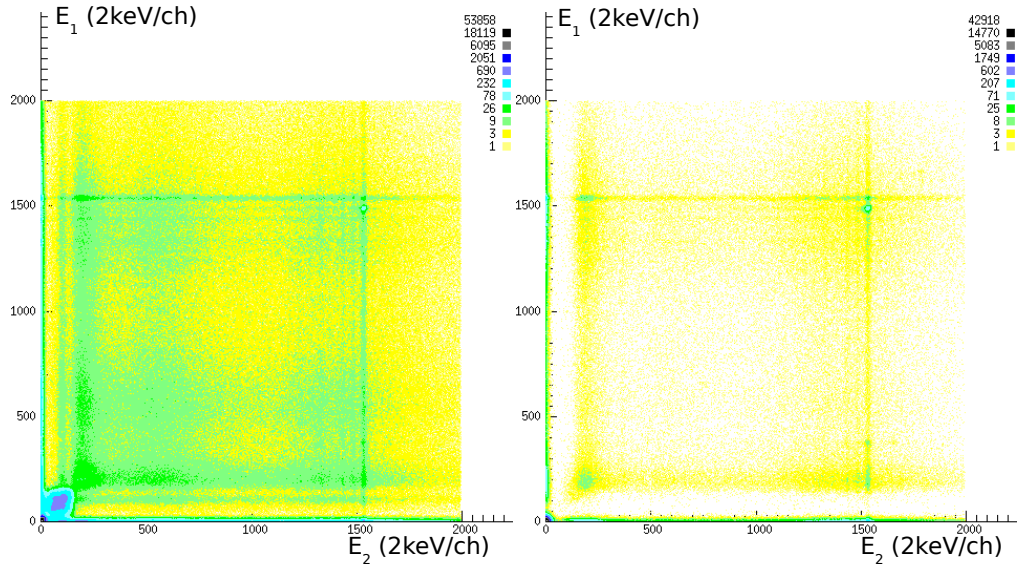


Figure 4.5: Correlation spectra of decay events. The energy of each decay is on the vertical axis, and the energy of the next decay at the same DSSD position is on the horizontal axis. The energy scales are 2 keV/ch. Left panel: no condition is applied. Right panel: the anticoincidence condition is applied.

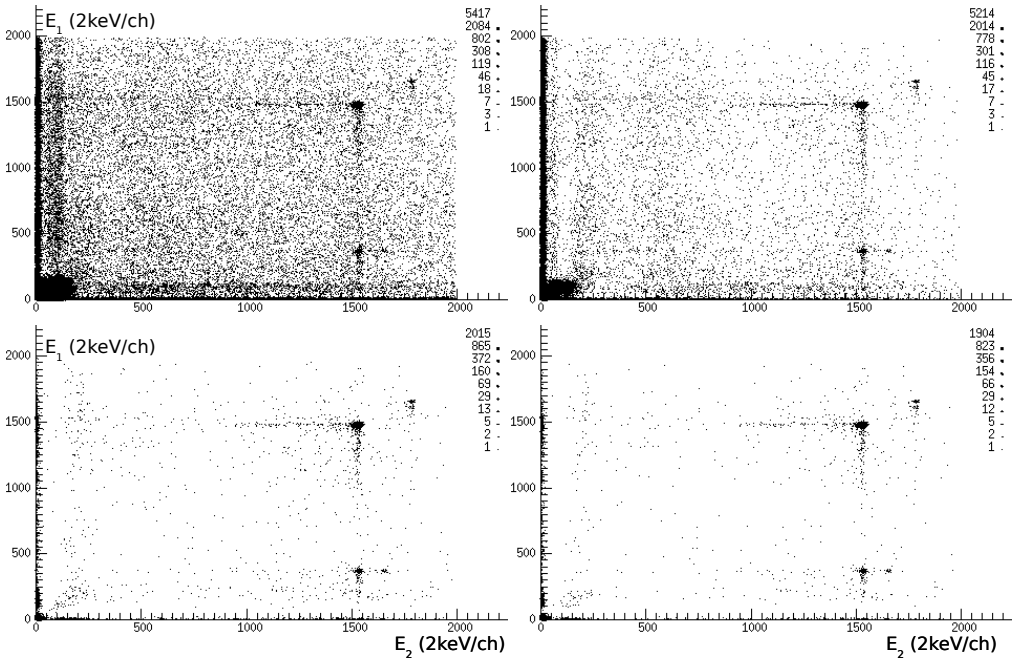


Figure 4.6: Correlation spectra of decay events. The energy of the 1^{st} generation decay is on the vertical axis, and the energy of the 2^{nd} generation decay is on the horizontal axis. The energy scales are 2 keV/ch. Upper left panel: no condition is applied. Upper right panel: the energy difference condition is applied. Lower left panel: the anticoincidence condition is applied. Lower right panel: both the anticoincidence and the energy difference conditions are applied.

Table 4.1: Ranges (R) in silicon and detection efficiencies calculated for alphas and protons of different energies in the DSSD. For these calclations it was assumed that particles were emitted in the DSSD at a position of $11.24 \pm 0.62\,\mu$m, corresponding to the implantation depth of ^{112}Cs ions in this experiment.

Parent	Particle	R (μm)	Efficiency (%)
^{111}Xe	α	15.5 ± 0.31	87 ± 3
^{107}Te	α	16.9 ± 0.31	84 ± 2
^{108}I	α	18.4 ± 0.36	81 ± 2
^{112}Cs	p	12.1 ± 0.28	97 ± 3

The fraction of particles escaping the active volume of the DSSD is

$$F = \frac{2\pi\,(1 - \cos\theta)}{2} \tag{4.1}$$

where the angle θ is defined by the relation

$$\cos\theta = \frac{D}{R} \tag{4.2}$$

if R is larger than D. This simple calculation was tested with GEANT simulations. Those simulations included the inplantation of ions in a silicon detector and their subsequent decay. The simulated results agree with Equation 4.1. The calculated efficiencies are reported in Table 4.1.

4.4 Results for ^{112}Cs

4.4.1 Proton decay

Figure 4.7 shows the spectrum of first generation decay events collected in 120 hours of measurement. The lower energy peak corresponds to the protons emitted by ^{109}I and ^{112}Cs (811 ± 5 keV [Blank and Borge, 2008] and 807 ± 7 keV [Page et al., 1994b], respectively) that cannot be resolved, while the higher energy peak corresponds to the protons emitted by ^{113}Cs ($E_p = 960 \pm 3$ keV [Hofmann, 1995], $T_{\frac{1}{2}} = 18.3 \pm 0.3\,\mu$s [Gross et al., 1998]). Both ^{109}I

and ^{113}Cs are present in the beam as either charge-state contaminants or tail-of-the-recoil-distribution contaminants. The amount of ^{109}I present in the beam was determined by analysing the time distribution of the ^{109}I and ^{112}Cs protons, since their half-lives differ by a factor of about 5. Figure 4.8 shows the proton decay of ^{112}Cs and ^{109}I. The exponential curve describes the decay of both nuclei, with the half-life of ^{109}I being $93.5 \pm 0.3\,\mu$s [Mazzocchi et al., 2007]. This time decay curve was fitted to the data with a Poisson maximum log-likelihood method, which has been shown to give better results than chi-square methods for counting experiments [Hauschild and Jentschel, 2001]. From these data the half-life of ^{112}Cs could be determined with higher precision to be $506 \pm 55\,\mu$s.

4.4.2 Alpha decay

Figure 4.9 shows the decay-decay correlated events. Two known decay chains can be identified:

$^{112}\mathrm{Xe} \rightarrow {}^{108}\mathrm{Te} \rightarrow {}^{104}\mathrm{Sn}$

$^{111}\mathrm{Xe} \rightarrow {}^{107}\mathrm{Te} \rightarrow {}^{103}\mathrm{Sn}$

The alpha decay of ^{111}Xe is preceded by the proton decay of ^{112}Cs, which may be undetected if it occurs within $100\,\mu$s of an ion implantation. Some of the alpha decays of ^{111}Xe thus appear in this figure as first generation decays, while they are actually second generation decays.

The alpha decay of ^{112}Cs would be expected to have a Q value of at least 3.83 MeV, as noted in the Introduction, and to be followed by the alpha decay of ^{108}I with energy 3947 ± 5 keV, corresponding to a Q value of 4099 ± 5 keV [Page et al., 1994a]. The alpha decay of ^{112}Cs was not observed in these measurements, therefore only an upper limit to the branching ratio for α decay of ^{112}Cs could be inferred. We took into account the alpha branching ratio of ^{108}I (91^{+9}_{-14} % [Page et al., 1994a]) and the detection efficiency for alphas (83(2) % at 3.83 MeV). The efficiency of the DSSD was calculated from the depth of ion implantation and the range of emitted particles in silicon and tested with a GEANT4

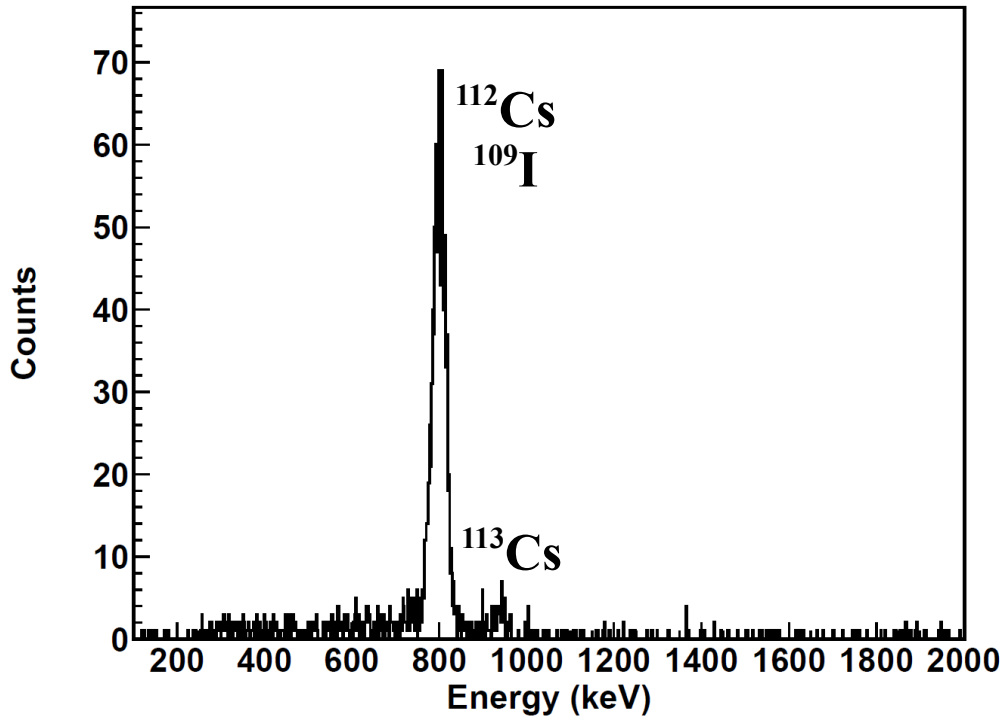


Figure 4.7: Portion of the energy spectrum of decay events following the implantation of an ion in the same pixel of the detector. This spectrum shows decays within 5 ms of a recoil.

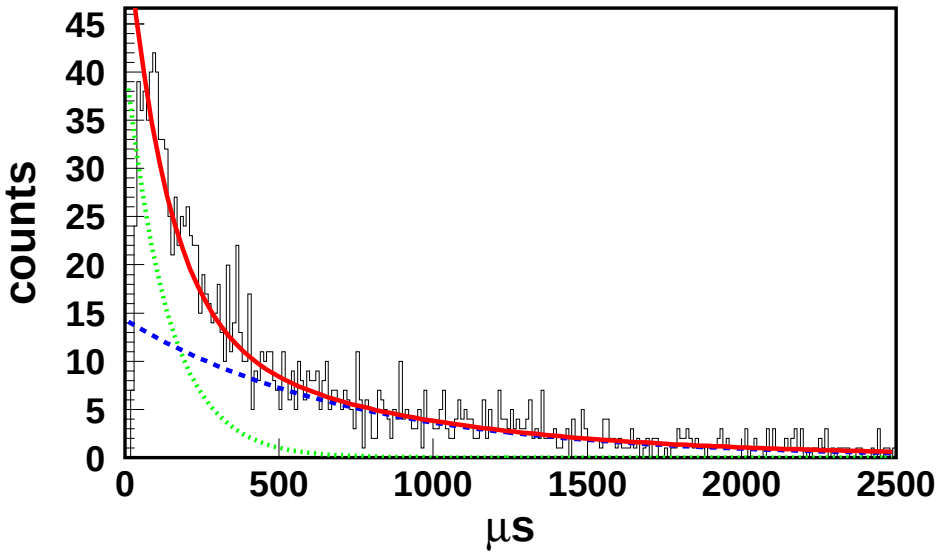


Figure 4.8: Proton decay of ^{109}I and ^{112}Cs, with the time decay curve used to determine the half-life of ^{112}Cs. The dashed line represents the decay of ^{112}Cs, and the dotted line represents the decay of ^{109}I.

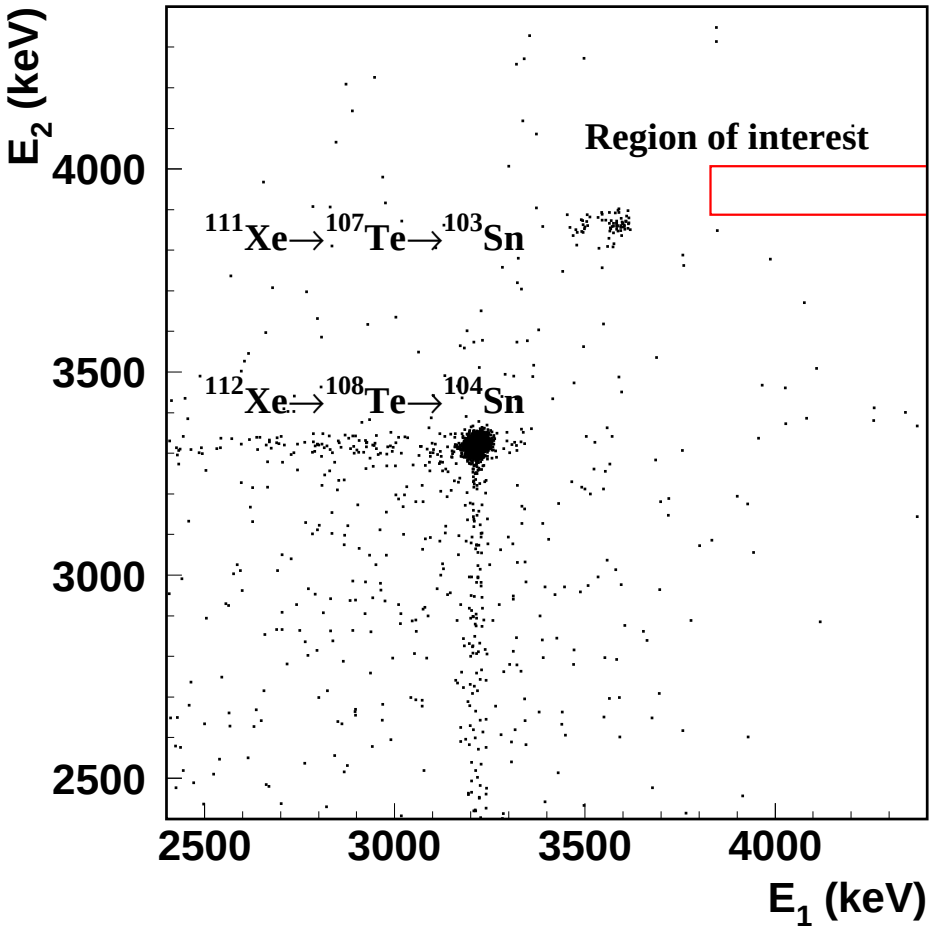


Figure 4.9: Decay-decay correlated events: the energy of the first decay event detected after ion implantation is on the horizontal axis, while the energy of the second decay event in the same DSSD pixel is on the vertical axis. The box shows where alpha decay of ^{112}Cs, correlated to alpha decay of ^{108}I (3947 ± 5 keV [Page et al., 1994a]), would be expected.

simulation , as reported in section 4.3.

Using Poisson statistical analysis, we could establish an upper limit of 0.53% for the alpha branching ratio of ^{112}Cs, with 90% confidence level.

In order to estimate the $Q_\alpha$value for ^{112}Cs from the available information, an assumption had to be made. Since away from the Z=50 shell closure, at Z=53, 55, shape deformation is expected (of the order of $\beta = 0.1$ for ^{112}Cs [Ferreira and Maglione, 2001]), the reduced α-decay width [Rasmussen, 1959] of ^{114}Cs was assumed for ^{112}Cs, i.e. $\delta^2 = 0.072^{+0.048}_{-0.028}$ MeV [Schardt et al., 1979,Roeckl et al., 1980]. In this approximate way any deformation of ^{112}Cs is taken into account: using the reduced α-decay width for the neighbor ^{114}Cs and δ^2 analysis in the spherical approach, we assume a similar potential tunnelled by the alpha particle for the decay of the two neighboring odd-odd cesium isotopes. Under this ansatz the α branching ratio can be calculated as a function of the Q_α value for l=0 and l=2, as shown in Figure 4.10. We can therefore infer an upper limit to the Q_α value for ^{112}Cs of 4.21 MeV, as indicated by the vertical dashed line in Figure 4.10.

4.4.3 Proton separation energies

The new upper limit on Q_α (^{112}Cs) implies lower limits on the Q_p values for ^{104}Sb and ^{108}I of 0.15 MeV and 0.24 MeV, respectively. In Figure 4.11 the Q_p values for the odd-Z cesium, iodine and antimony isotopes are plotted. An upper limit for $Q_p(^{108}\mathrm{I})$, which implies an upper limit for $Q_p(^{104}\mathrm{Sb})$, was deduced in [Page et al., 1994a]. This constrains the Q_p values to the energy windows $0.15\,\mathrm{MeV} \leq Q_p(^{104}\mathrm{Sb}) \leq 0.52\,\mathrm{MeV}$ and $0.24\,\mathrm{MeV} \leq Q_p(^{108}\mathrm{I}) \leq 0.60\,\mathrm{MeV}$, as shown by the boxes in Figure 4.11. These new estimated Q values are also summarized in Table 4.2.

4.4.4 Odd-even effect

These results are compatible with the expected odd-even effect discussed in Section 2.5. The estimated value of $Q_p(^{104}\mathrm{Sb})$ indicates that ^{104}Sb is unstable against proton emission,

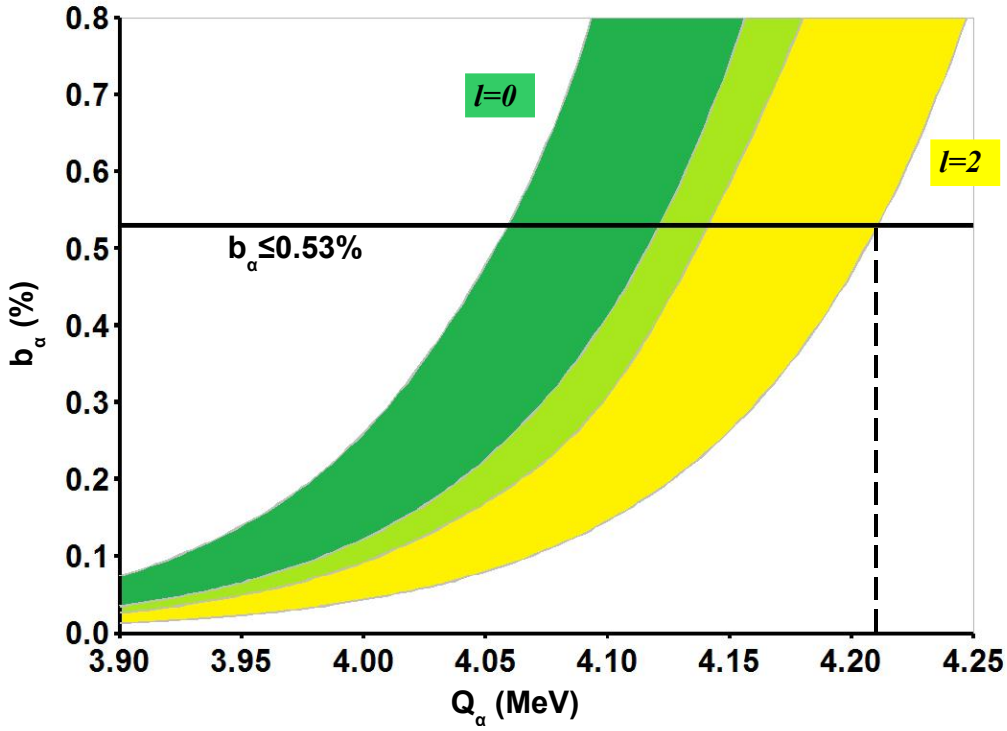


Figure 4.10: Alpha branching ratio of ^{112}Cs as a function of its Q_α value. The green (dark) and the yellow (light) bands represent the value with error bars calculated for l=0 and l=2 respectively. The horizontal line shows the measured upper limit for the alpha branching ratio. The dashed vertical line shows the estimated upper limit for the Q_α value. See text for details.

Table 4.2: Summary of the newly estimated Q_p and Q_α values.

Nucleus	Q_p (MeV)	Q_α (MeV)
^{104}Sb	0.15–0.52	
^{108}I	0.24–0.60	
^{112}Cs		3.83–4.21

and therefore the Sn-Sb-Te cycle described in Section 2.4 can not start at ^{104}Sb.

The available data for Q_p values of antimony isotopes were compared to shell model calculations, using the nucleon-nucleon potential AV18 [Wiringa et al., 1995]. The calculations' results, normalized to the experimental value of $Q_p(^{105}\text{Sb})$, are shown in Figure 4.11. Given the excellent agreement between calculations and experimental data, it is reasonable to expect the simulations to offer reliable predictions on the Q_p values of ^{103}Sb and ^{102}Sb. According to the calculations, those two nuclei would decay with proton emission, with half-lives of the order of 10 ps and 1 ns, respectively. The detection of such short-lived decay would not be possible with standard techniques.

4.5 Results for ^{111}Xe

With this experiment it was also possible to gather information on ^{111}Xe, produced by the proton decay of ^{112}Cs, and its daughter ^{107}Te. In particular, the alpha decay chain $^{111}\text{Xe} \rightarrow {}^{107}\text{Te} \rightarrow {}^{103}\text{Sn}$ was studied. Both ^{111}Xe and ^{107}Te are alpha and beta emitters. Their alpha branching ratios are known with low precision, their respective values being 8^{+8}_{-5} % [Page et al., 1994a] and 70 ± 30 % [Schardt et al., 1979].

4.5.1 Alpha branching ratio of ^{107}Te

The beta-decay partial half-life of ^{107}Te was calculated in [Möller et al., 1997] as 0.8994 s. It can also be estimated on the basis of systematics of beta-decay partial half-lives for tellurium isotopes. Figure 4.12 shows the trend of these values as a function of the mass number A, from ^{109}Te to ^{115}Te [Blachot, 2006, Blachot, 2009, Blachot, 2005a, Blachot,

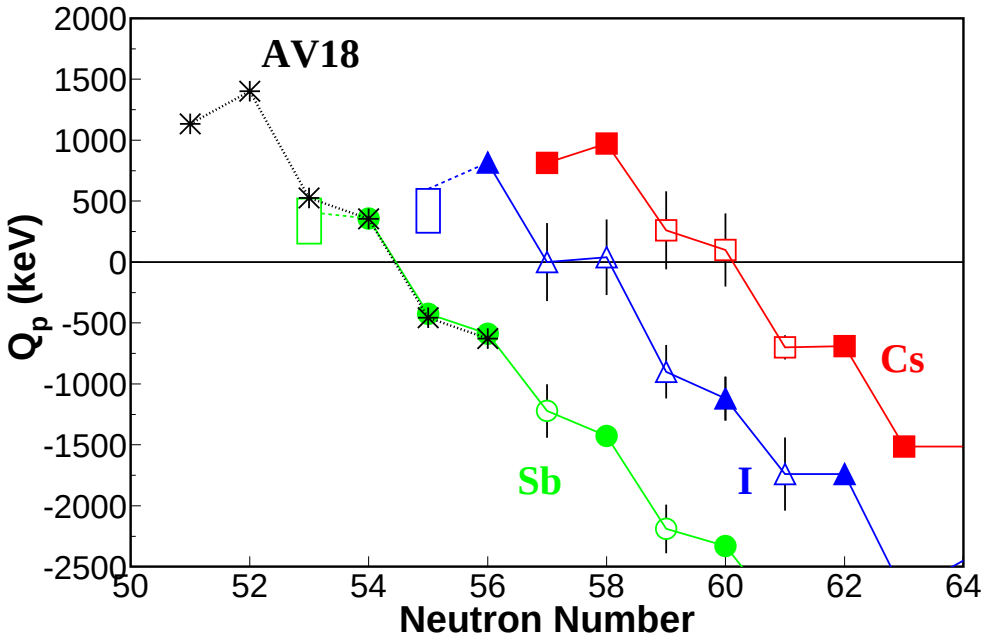


Figure 4.11: Q_p values for neutron-deficient Sb (Z = 51), I (Z = 53) and Cs (Z = 55) isotopes. Full symbols represent measured values [Blank and Borge, 2008] while open symbols represent extrapolations [Audi et al., 2003]. The boxes represent the energy windows expected for the proton separation energies of ^{104}Sb and ^{108}I ([Page et al., 1994a] and present work). The symbols connected by the dotted line represent shell model calculations. See text for details.

2005b]. With a linear regression on $\ln(T_\beta)$, the beta-decay partial half-life of ^{107}Te can be estimated to be 1.1 ± 0.1 s. This value, obtained with a simple extrapolation, is in agreement with the value calculated in [Möller et al., 1997]. Using 3.1 ± 0.1 ms as the total half-life [Page et al., 1994a], the beta branching ratio for ^{107}Te is calculated to be 0.29(3) %. Its alpha branching ratio is therefore larger than 99.7 %.

4.5.2 Alpha branching ratio of ^{111}Xe

In order to determine the alpha branching ratio for ^{111}Xe, the number of ^{111}Xe nuclei needs to be known. This can be directly inferred from the number of protons from the decay of ^{112}Cs, corrected for the detection efficiency for ^{112}Cs protons (97(3) %). The alpha branching ratio of ^{111}Xe can be determined by taking into account the number of ^{111}Xe nuclei, the number of ^{107}Te alpha decays, the detector's efficiency for ^{107}Te alphas (84(2) %), and the newly estimated alpha branching ratio of ^{107}Te. The result is $b_\alpha(^{111}\text{Xe}) = 10.4 \pm 1.9$ %, much more accurate than the earlier value of 8^{+8}_{-5} % [Page et al., 1994a].

Figure 4.13 shows the two alpha transitions from the decay of ^{111}Xe. This observation of fine structure in the alpha decay of ^{111}Xe leads also to an improved determination of the relative branching ratios: 76(5) % of the alpha decays of ^{111}Xe proceed to the ground state of ^{107}Te. This is consistent with the previous result of 69(7) % [Schardt et al., 1979].

4.5.3 Alpha reduced widths

The results described so far have been utilized to determine the reduced alpha-decay width for the relevant transitions with improved accuracy. Table 4.3 contains those values. The W_α value for the decay of ^{107}Te is larger than the W_α value for the alpha transitions of ^{111}Xe. That is consistent with the expectation that the alpha decay is enhanced for nuclei with only a few valence nucleons outside of a doubly magic core, and particularly for those with a simpler valence configuration like that of ^{107}Te when compared to ^{111}Xe. The same trend was observed for the alpha decay of ^{109}Xe and its daughter ^{105}Te when those decays

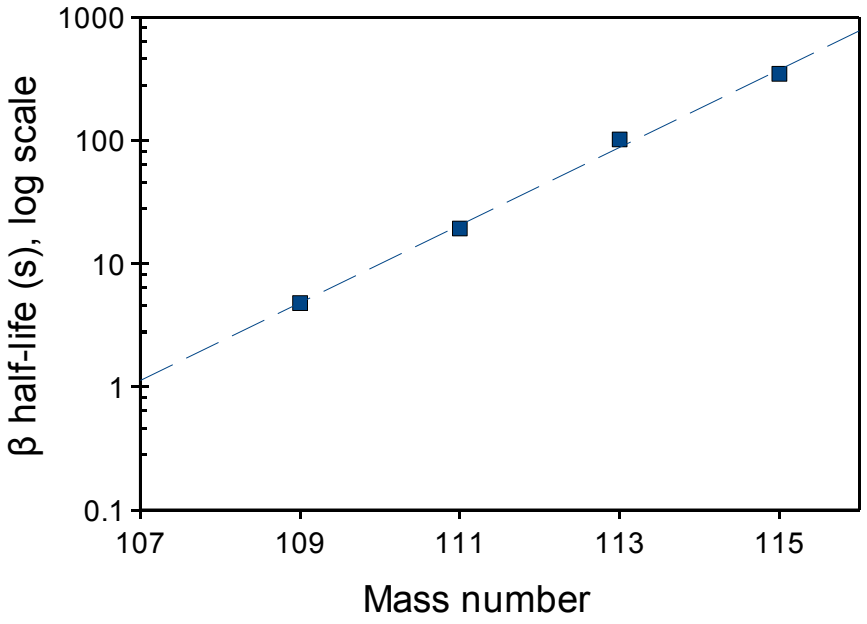


Figure 4.12: Partial beta half-life T_β for odd-A tellurium isotopes [Blachot, 2006, Blachot, 2009, Blachot, 2005a, Blachot, 2005b] as a function of the mass number A. The straight dashed line represents a linear fit on $\ln(T_\beta)$, used to estimate the beta half-life of ^{107}Te.

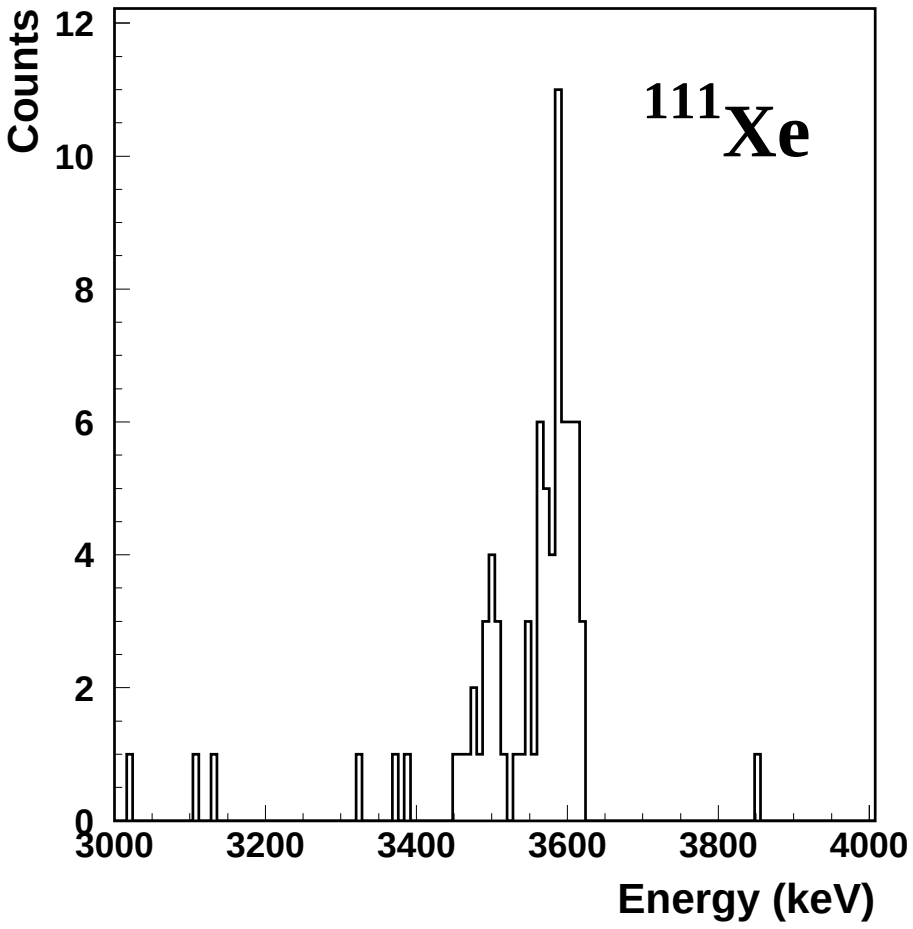


Figure 4.13: Energy spectrum of the alpha decay of ^{111}Xe. These decay events are selected by requiring that the next decay in the same DSSD pixel belongs to ^{107}Te. Both the ^{111}Xe alpha transitions are present in the spectrum.

Table 4.3: Summary of alpha decay properties of ^{111}Xe and ^{107}Te: energy (E_α), branching ratio (b_α), reduced alpha-decay width (δ^2) and reduced alpha-decay width relative to ^{212}Po (W_α). See text for details.

Nucleus	E_α (MeV)	b_α (%)	δ^2 (MeV)	W_α
^{111}Xe	3582 ± 10 [Heine et al., 1991]	7.9 ± 1.5	$0.054^{+0.02}_{-0.07}$	$0.78^{+0.11}_{-0.10}$
	3500 ± 15 [Heine et al., 1992]	2.5 ± 1.7	$0.028^{+0.008}_{-0.004}$	$0.40^{+0.06}_{-0.05}$
^{107}Te	3862 ± 5 [Page et al., 1994b]	≥ 99.7	$0.14^{+0.02}_{-0.01}$	$2.06^{+0.15}_{-0.14}$

were observed for the first time [Liddick et al., 2006]. In both cases the reduced alpha decay width of the tellurium isotope is larger than that of its xenon parent by a factor of about 2.

The value of W_α for ^{107}Te can also be compared to that of its valence mirror nucleus ^{215}Po. These nuclei have the same valence nucleon configuration ($2\alpha + n$) outside of a doubly closed core (^{100}Sn and ^{208}Pb, respectively). The alpha decay enhancement of a Te isotope with respect to its Po counterpart can be defined as W_α(Te)/W_α(Po). With $W_\alpha(^{215}\text{Po}) = 1.16 \pm 0.01$ [Audi et al., 2003], the result for the enhancement is 1.78 ± 0.15, consistent with the values reported in [Liddick et al., 2006] for ^{107}Te and other Te isotopes.

4.6 Summary

An improved measurement of the half-life of ^{112}Cs, which is $506 \pm 55\,\mu$s, has been obtained. The attempt to observe the alpha decay of ^{112}Cs for the first time was not successful, but it allowed an upper limit of 0.53% for its alpha branching ratio to be set. With this result, and assuming that ^{112}Cs has the same reduced alpha-decay width as ^{114}Cs, a new upper limit for the Q_α value of ^{112}Cs and new lower limits for the Q_p values of ^{104}Sb and ^{108}I were deduced. Those estimates are compatible with the expected odd-even effect, and indicate that the astrophysical rp-process can not reach ^{104}Sb. A new measurement of the alpha branching ratio of ^{111}Xe has also been obtained. The available information on proton emission has been compared to shell model calculations, finding very good agreement between observed

and predicted proton decay energies. Predictions for proton emission from the more exotic ^{103}Sb and ^{102}Sb have also been made.

Chapter 5

The ^{70}Ni and ^{72}Ni experiment

5.1 Motivation

A systematic study of Ni isotopes in the vicinity of doubly-magic ^{78}Ni will help in the understanding of shell closure effects, isomerism, and single particle states in this interesting region of the nuclear chart far from stability. In [Perru et al., 2006] the reduced transition probability B(E2) for electromagnetic transitions in ^{70}Ni was measured by Coulomb excitation, and the measured values were compared to shell model calculations [Lisetskiy et al., 2005], as shown in Figure 5.1. Calculations and measurement were in agreement for $8_1^+ \rightarrow 6_1^+$ and $6_1^+ \rightarrow 4_1^+$ transitions, but for $2_1^+ \rightarrow 0_{gs}^+$ the measured transition probability was significantly larger than the calculated value, indicating enhanced proton core polarization.

In order to further investigate the issue, the goal of the experiment described in this chapter was to measure the lifetime of electromagnetic transitions in ^{70}Ni and ^{72}Ni, particularly the $4_1^+ \rightarrow 2_1^+$ and $2_1^+ \rightarrow 0_{gs}^+$ transitions. From calculations [Lisetskiy et al., 2005] the lifetimes of the 4^+ states are expected to be of about 50 ps, and the lifetime of the 2^+ of ^{70}Ni was expected to be of about 4 ps. From the measurements in [Perru et al., 2006] the lifetime of the 2^+ of ^{70}Ni was of the order of 1 ps.

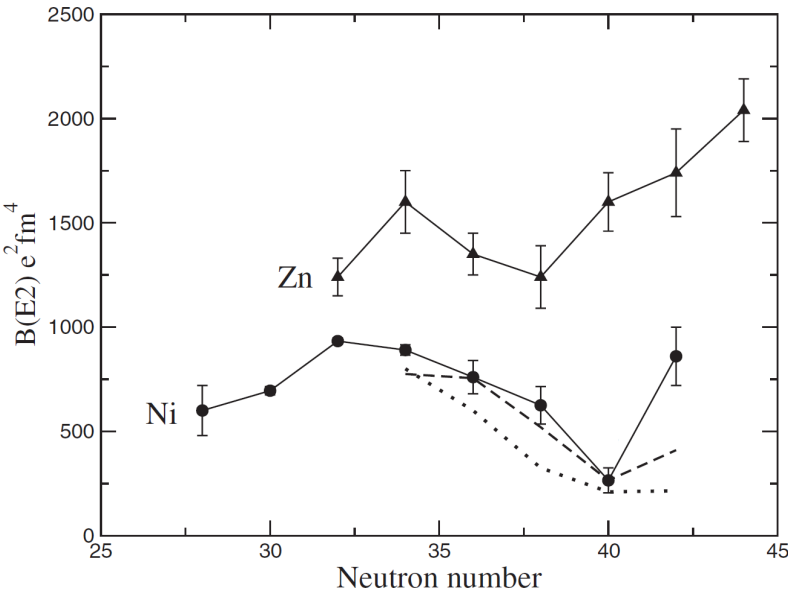


Figure 5.1: Experimental B(E2;$0^+ \rightarrow 2^+$) values for even-even nickel and zinc isotopes. The dashed and dotted lines represent shell model calculations. (Figure taken from [Perru et al., 2006]).

5.2 The Plunger method

The plunger method was shown to be particularly suited to measure gamma lifetimes of the order of a few picoseconds [Chester et al., 2006]. The main components of a plunger device are the target and the degrader, and the distance between them can be varied. The incoming beam goes through the target, where the nucleus of interest is produced. The beam coming out of the target then goes through the degrader, where it loses part of its kinetic energy.

The target-degrader distance is chosen so that the time of flight between them is of the order of the lifetime of the excited state that is to be measured. For this experiment, the expected lifetimes were of the order of 1 ps (corresponding to a distance of about 100 μm) to a few tens of ps (corresponding to a distance of a few millimeters). A gamma detector array at a forward angle will detect each gamma with a Doppler-shifted energy, as given by the expression

$$E_{detected} = E_0 \frac{1 - \beta \cos(\theta)}{\sqrt{1 - \beta^2}} \tag{5.1}$$

where β is the velocity of the emitting nucleus in units of c, and θ is the angle between the emitted gamma and the beam line.

As illustrated in Figure 5.2, a gamma transition in the beam will result in two energy peaks at two different doppler-shifted energies, with relative intensities depending on the distance between the target and degrader. The lifetime of the excited state can then be calculated from the relative intensities of the two peaks at different target-degrader distances (see for example [Chester et al., 2006] for details).

It is also possible to match the experimental gamma spectra with GEANT4 simulations [Adrich et al., 2009], using the half-life of the state of interest as a parameter that can be changed in order to obtain the best possible fit. This method of measurement gives good precision and accuracy [Audi et al., 2003, Bazin et al., 2003]. For example, it has been used

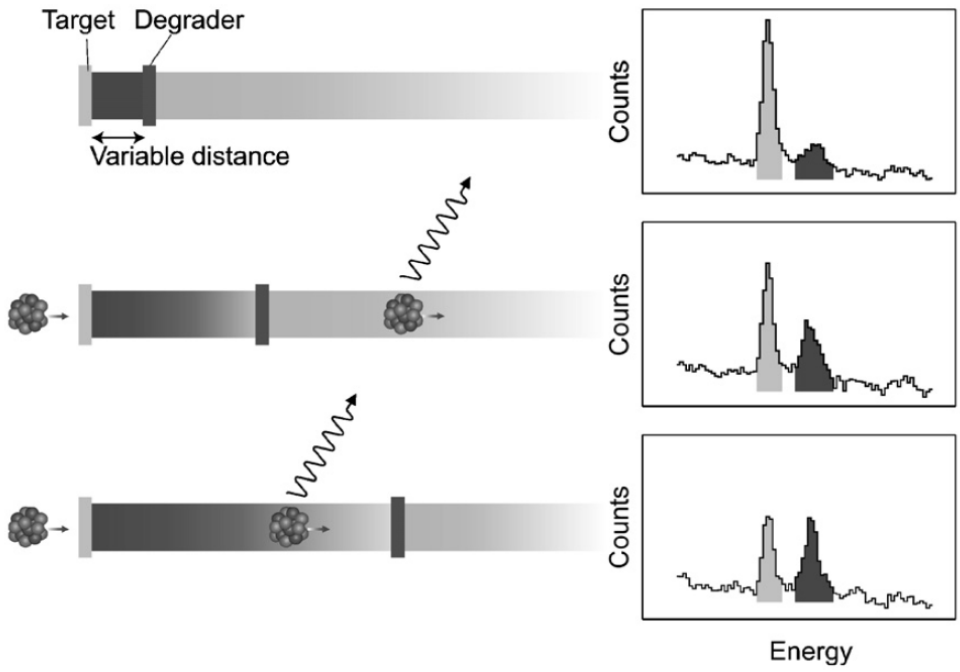


Figure 5.2: Left panel: schematic drawing of the plunger device, at three different target-degrader distances. Right panel: the experimental energy spectra. The dark gray color corresponds to gammas emitted before the degrader, while the light gray color corresponds to gammas emitted after the degrader. The energies are measured by detectors at a forward angle. (Figure taken from [Adrich et al., 2009]).

successfully for the measurement of the lifetime of the 2^+ state in ^{20}C [Petri et al., 2011].

Figure 5.3 shows a picture of the Köln-NSCL plunger device [Adrich et al., 2009], used for our experiment.

5.3 Setup

The experiment was performed at the National Superconducting Cyclotron Laboratory (NSCL) at Michigan State University. Figure 5.4 shows a schematic drawing of the beam line at NSCL, including the position of the S800 target, the S800 focal plane, and the scintillator detectors used for time-of-flight measurement (see Section 6.2). The plunger apparatus was situated at the target position of the S800 Spectrograph [Bazin et al., 2003] and it included a beryllium target (296 μm thick) and a gold degrader (210 μm thick). The degrader material and thickness were chosen after performing GEANT4 simulations of the experiment.

As discussed in [Adrich et al., 2009], GEANT4 simulation tools were developed specifically for the simulation of plunger experiments conducted at NSCL. The response of the detectors is accurately modeled, so that actual experimental results can be reproduced. More details will be given in Section 6.5. These simulations are very useful when experiments are planned, because they can be used to test different available options (such ase beam settings, targets, and position of movable detectors). Various possible materials and thicknesses were considered for the degrader. The objective was to obtain gamma spectra where the gammas emitted before and after the degrader were well separated. If the degrader was too thin the two detected peaks would be too close to be resolved. If the degrader was too thick there would be many gammas emitted while the ion was still traveling through the degrader, and the data analysis would be more difficult.

A secondary beam of ^{71}Cu, coming from the A1900 fragment separator [Morrissey et al., 2003], impinged on the beryllium target. The desired ^{70}Ni was produced via the one-proton knockout reaction $^{71}\mathrm{Cu} \rightarrow {}^{70}\mathrm{Ni} + \mathrm{p}$. The other nickel isotope of interest, ^{72}Ni,



Figure 5.3: Picture of the Köln-NSCL plunger device [Adrich et al., 2009].

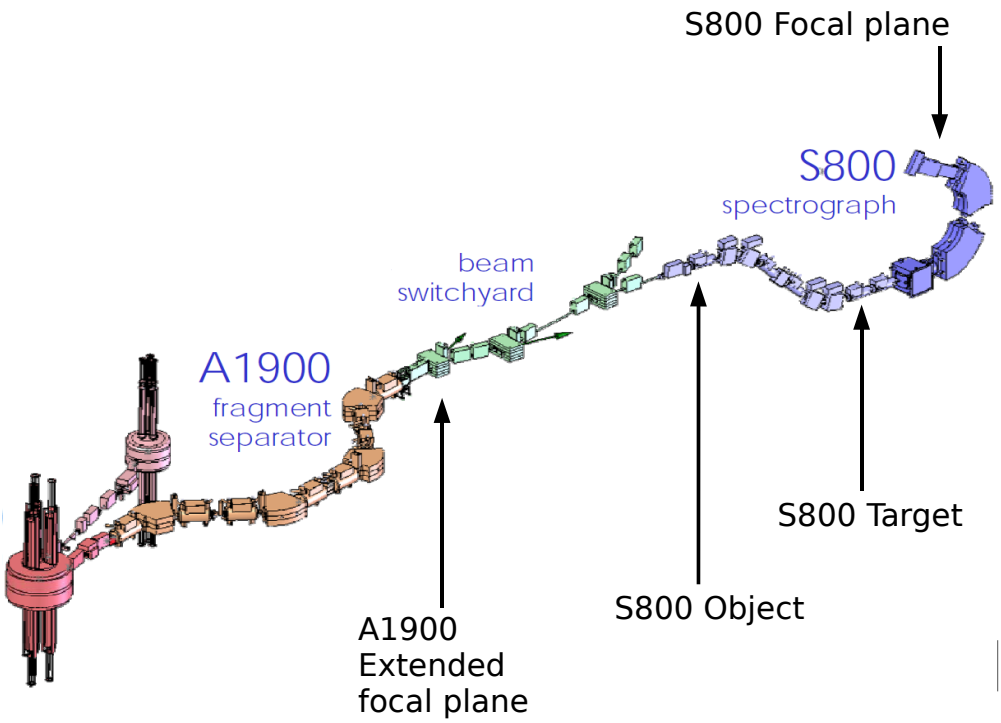


Figure 5.4: Schematic drawing of the beam line used for this experiment at NSCL.

was produced in the same way, using a secondary beam of ^{73}Cu from the A1900 and a one-proton knockout reaction in the target. The reaction products then went through the gold degrader.

The plunger was surrounded by two arrays of segmented germanium detectors (SeGA) to measure the gamma rays emitted by the nickel ions both before and after the degrader. The detectors in the forward and backward arrays were oriented at an angle of 30° and 140° with respect to the beam line, respectively. For the energy measurement we relied on the central contact. We used the segments mainly to calculate the angle of the emitted gamma with respect to the beam line, for the Doppler correction.

The reaction products went on through the S800 spectrometer, to be identified at the focal plane [Yurkon et al., 1999]. Figure 5.5 shows the detector array at the focal plane of the S800 spectrometer. The beam goes through two Cathode Readout Drift Chambers, CRDC1 and CRDC2. These detectors are used to measure the X and Y position of the particles as well as the angles of their trajectory in the dispersive and non-dispersive plane. The dispersive plane includes the beam axis and the X axis. The non-dispersive plane includes the beam axis and the Y axis. The information on position and angles is used for particle tracking. These detectors are followed by an ion chamber and three scintillator detectors. The energy loss in the ion chamber and the total energy are used for particle identifiction.

Table 5.1 lists the experimental runs at different settings of the S800 spectrometer and different plunger arrangements.

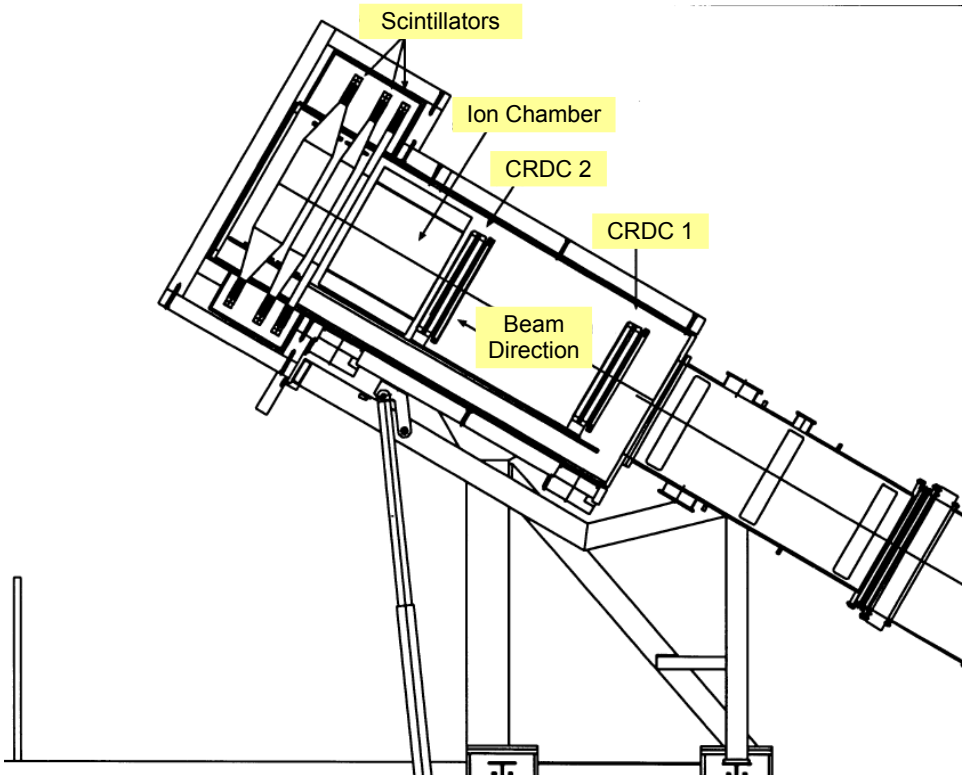


Figure 5.5: Drawing of the detectors at the focal plane of the S800 spectrometer. (Figure modified from [Yurkon et al., 1999]).

Table 5.1: List of the experimental runs, grouped by S800 and plunger settings; d is the target-degrader distance.

S800 setting	Plunger	d (mm)	Run numbers
^{71}Cu	No plunger		4, 63
^{71}Cu	Target only		64
^{71}Cu	Plunger		7
^{70}Ni	Target only		67-69, 73-78, 80-84
^{70}Ni	Plunger	0.1	11-23
^{70}Ni	Plunger	0.2	40-48
^{70}Ni	Plunger	0.5	30-31, 33-39
^{70}Ni	Plunger	1	24-29
^{70}Ni	Plunger	10	49-69
^{73}Cu	No plunger		151
^{73}Cu	Target only		152
^{73}Cu	Plunger		85-86
^{72}Ni	Target only		155-164, 166-167
^{72}Ni	Plunger	0	113-125, 129-134
^{72}Ni	Plunger	1	95-111
^{72}Ni	Plunger	2	184-195
^{72}Ni	Plunger	10	135-150

Chapter 6

Data analysis and results of the ^{70}Ni experiment

The data analysis was done through the following steps. First some of the detectors used in the experiment were calibrated: the Segmented Germanium Arrays surrounding the plunger, the Cathode Readout Drift Chambers, and the Ion Chamber. The calibration procedures are described in Section 6.1. Other detectors, such as scintillators along the beam line used for time-of-flight (TOF) measurements, did not require new calibrations. The next step was particle identification (ID). We identified the incoming particles, arriving to the target, and the outgoing particles, moving beyond the target. Then we selected the gammas detected in coincidence with the Ni ions under investigation (^{70}Ni or ^{71}Ni). Particle tracking was done by using the information from the detectors at the S800 focal plane to calculate the position and momentum of the particles at the target. Finally, GEANT4 simulations were used to reproduce the experimental gamma spectra and find the most probable values of the half-lives of interest. The standard method to extract that information is to run the simulation with different values of the half-life, calculate the goodness of fit with a chi-square method, and find the value of the half-life corresponding to the best fit.

6.1 Detectors calibration

6.1.1 SeGa calibration

A ^{226}Ra gamma source was used for the energy calibration of the Segmented Germanium Arrays. The source was stationary at the target position. For the central contacts, the relation between the channel number and the energy is approximately linear. A 2^{nd} order polynomial fit was used in order to obtain an accurate energy calibration. Figure 6.1 shows calibrated gamma spectra of the ^{226}Ra source, measured by the central contact of two of the detectors. The energy resolution is 3.6 keV FWHM at 1260 KeV.

The energy calibration of the segments is more complicated. When a gamma ray is detected, the central contact measures the whole energy deposited in the detector, but the same gamma may interact with more than just one of the segments. The event is called Fold 1, Fold 2, Fold 3... when the gamma interacts with one segment, two segments, three segments... respectively. Each segment needs to be energy-calibrated independently in order to measure Fold 1 events correctly. In case of Fold 2 events, the total energy deposited in the detector is not simply the sum of the energies measured in the two segments, because of electronic coupling between different segments. For that reason, an independent calibration is needed for each pair of segments in the same detector. There are 32 segments in each detector, so there are $(32 \times 31)/2 = 496$ pairs in each detectors. For the calibration of higher-order events, it would not be practical to consider each possible group of segments, so the interaction between segments is split into pair-wise couplings in order to calculate the total energy.

Figure 6.2 shows calibrated gamma spectra of the ^{226}Ra source, measured by the segments of detector number 1. The four spectra, from top to bottom, show Fold 1, 2, 3, and 4 events. As the number of segments increases, the lower energy peaks are less and less visible, because the gammas with lower energy are less likely to intheract with multiple segments. Considering multiple-fold events also tends to suppress the Compton continuum.

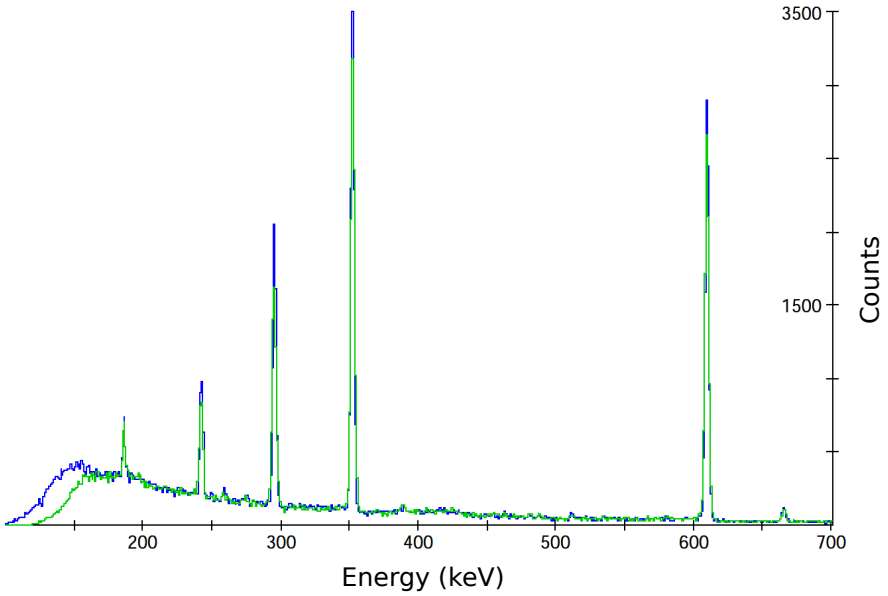


Figure 6.1: Energy-calibrated gamma spectra of the ^{226}Ra source. The horizontal axis shows the energy in keV. The two spectra are measured by the central contacts of SeGa detectors number 1 and 2.

The Compton continuum in the Fold 1 spectrum is due to gammas that escape the segment after Compton scattering events, without depositing their full energy in the segment. In the Fold 2 spectrum the Compton continuum is considerably reduced. Photons that interact only with one segment and then escape the detector are not registered in the Fold 2 spectrum. The only contributions to the Compton continuum in the Fold 2 spectrum come from photons that interact with more than two segments, and photons that escape the detector after interacting with two segments. In general, considering a Fold n spectrum, the only contributions to the Compton continuum come from gammas that interact with more than n segments, and from gammas that interact in exactly n segments before living the detector. Both occurrences are less likely for higher n, so the Compton continuum is greatly reduced. Figure 6.2 also shows the worsening of the resolution for higher-fold spectra. The FWHM of peaks in a Fold n spectrum is approximately $\sqrt{n}$ times larger than the FWHM in the Fold 1 spectrum, as expected.

6.1.2 CRDC calibration

For the position-sensitive Cathode Readout Drift Chambers, the relation between channel number and position is linear, both in the X and Y directions. In order to calibrate them we used a calibration mask that could be inserted in the beam line. The mask blocks most of the beam, and it has several holes and slits that allow the beam to pass only at those specific positions. It was inserted directly in front of either one of the CRDCs, at a distance of approximately 1 cm. Figure 6.3 shows a drawing of the calibration mask.

In the calibration procedure it is assumed that the trajectory of the particles in the beam is rectilinear as the beam traverses the calibration mask and the CRDCs. The angles of the trajectory with respect to the dispersive and non-dispersive planes are taken into account. The calibration program compares the calculated position of each hole and slit to its actual position on the calibration mask, which is known. The optimal calibration parameters are calculated with a least-squares procedure.

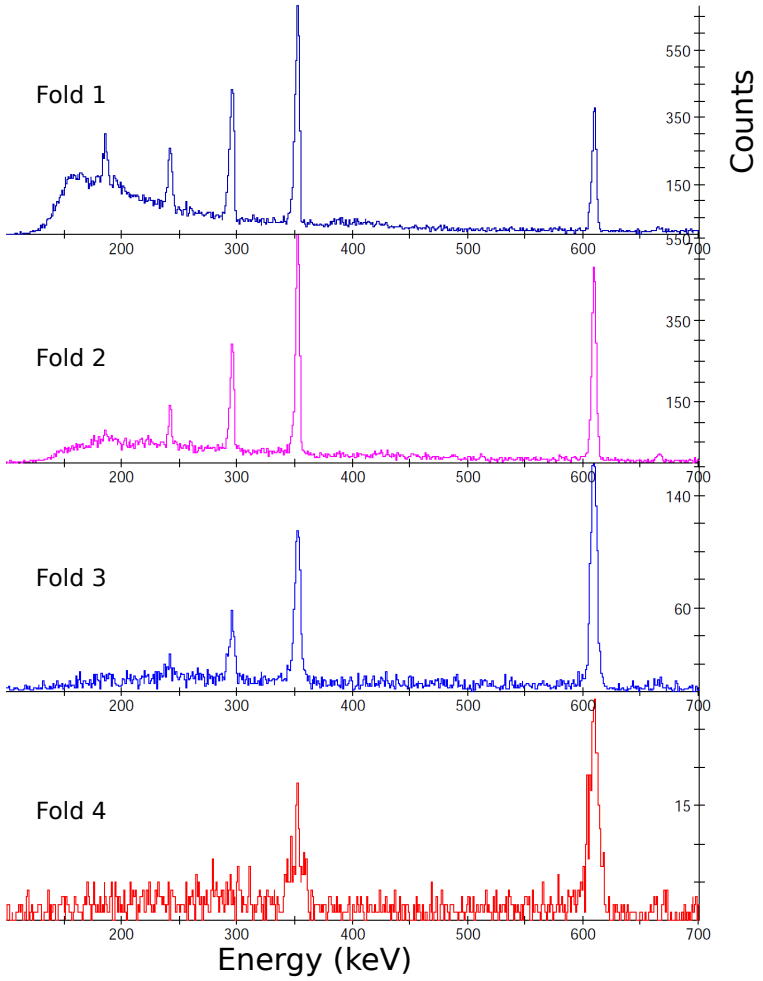


Figure 6.2: Energy-calibrated gamma spectra of the ^{226}Ra source, measured by the segments of detector number 1. The horizontal axis shows the energy in keV. The four spectra, from top to bottom, show Fold 1, 2, 3, and 4 events.

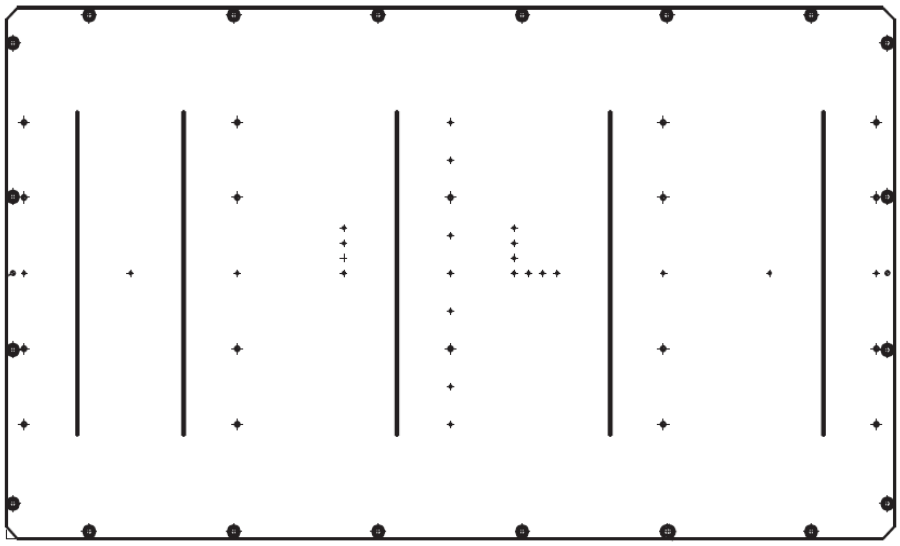


Figure 6.3: Schematic drawing of the mask used for the calibration of CRDCs.

The upper panel in Figure 6.4 shows the raw spectrum of counts per channel in the X direction obtained from a calibration run. The channels on the horizontal axis indicate the X position. The rectangles in the lower panel indicate the groups of channels selected by the experimenter to be used in the calibration procedure. The height of each rectangle is the ID number of the corresponding slit (or group of holes) on the mask.

Figure 6.5 shows the reconstructed 2D image of the beam passing through the mask, after calibration. The horizontal and vertical axes show the X and Y position in mm, respectively. The pattern of slits and holes of the calibration mask is well reproduced in this image, with a position resolution of 1 mm FWHM.

Mask calibration runs were repeated a total of four times during the whole experiment, because it has been noted that the calibration parameters vary over time. The variation over time of the calibration parameters found in this experiment was of the order of a few percent.

6.1.3 Ion chamber calibration

The ion chamber is divided into 16 segments, 1 inch thick and perpendicular to the beam line. Particles arriving at the S800 focal plane pass through all of the segments. The segments of the ion chamber were not truly energy calibrated. Instead they were gain-matched, so that each segment would read the same energy loss as other segments. It was assumed that a particle traversing the ion chamber lost the same amount of energy in each segment, which was a good approximation for the purpose of particle identification. We measured the energy loss of an unreacted monoenergetic ^{71}Cu beam, which gave a single peak in each segment of the ion chamber. Segment number 1 was taken as reference, with gain $= 1$ and offset $= 0$, and the other segments were matched to it.

The top of Figure 6.6 shows the raw spectra from three of the segments, as an example. The bottom of the figure shows the same spectra after gain-matching.

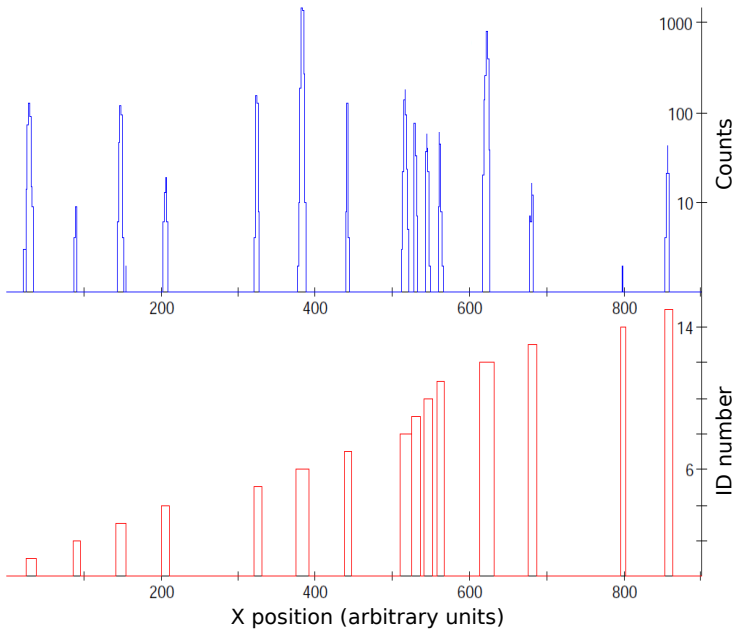


Figure 6.4: Upper panel: raw spectrum of counts per channel in the X direction obtained from a calibration run. Lower panel: the rectangles indicate the group of channels used in the calibration procedure.

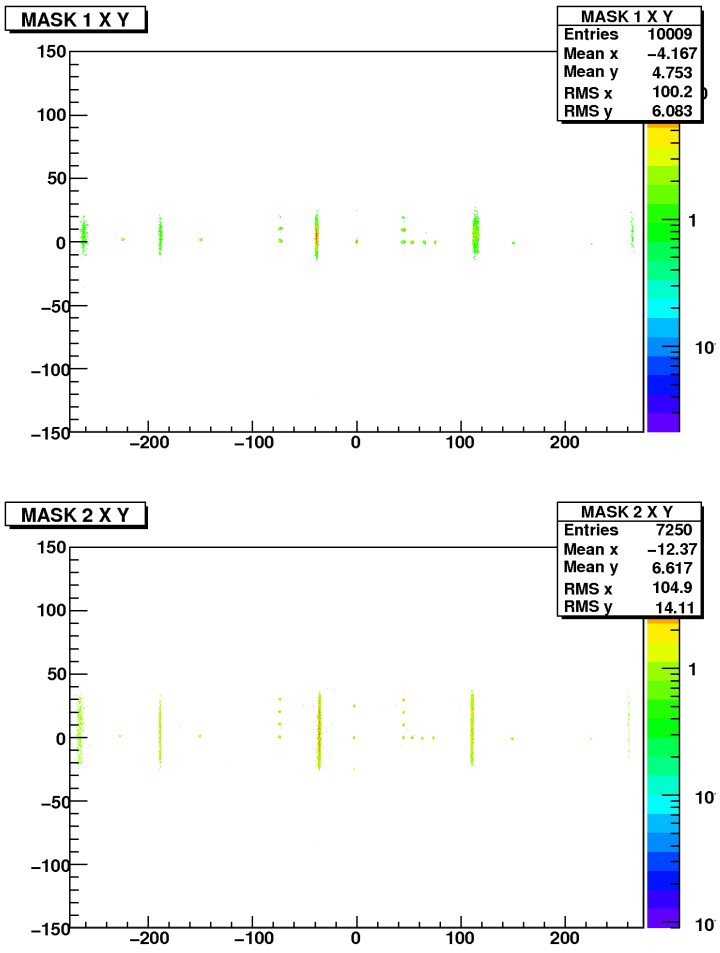


Figure 6.5: Reconstructed 2D image of the beam passing through the mask, after calibration. The horizontal and vertical axes show the X and Y position in mm, respectively. The upper image corresponds to the calibration mask in front of the first CRDC, while the lower image corresponds to the calibration mask in front of the second CRDC.

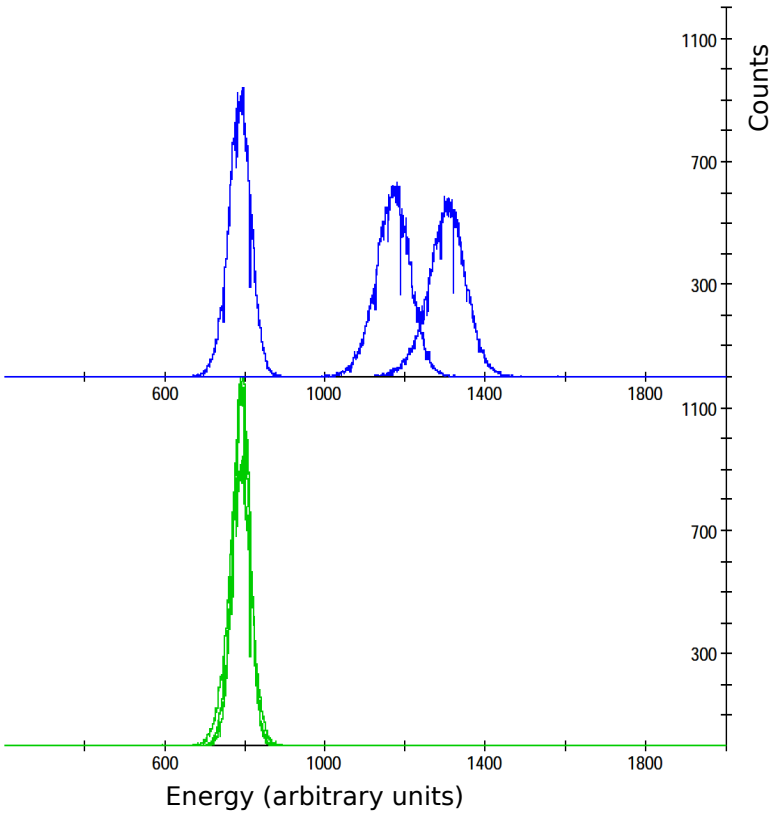


Figure 6.6: Energy loss of unreacted ^{71}Cu ions in segments number 1, 2 and 3 of the ion chamber. The upper and lower plots show the spectra before and after the gain-matching procedure. The energy on the horizontal axis is expressed in arbitrary units.

Table 6.1: Detectors used for TOF measurements. Refer to Figure 5.4 for the position of the scintillator along the meam line.

Name of scintillator	Position
XFP	Extended focal plane of A1900
OS	Object position of S800
E1	Focal plane of S800

6.2 Particle identification

6.2.1 Incoming particle identification

The identification of particles arriving at the target was based on time-of-flight (TOF) measurements. Table 6.1 gives the names of the scintillator detectors used for TOF measurements, as well as their positions along the beam line. Those positions are shown in the schematic drawing of Figure 5.4. The TOF between the XFP and OS detectors was used for incoming particle identification.

Figure 6.7 shows some of the TOF spectra used for particle identification of the incoming ^{71}Cu beam. The time of flight on the horizontal axis, expressed in arbitrary units, is between the XFP and OS detectors. The spectrum at the top of the figure corresponds to a run without plunger, the spectrum in the middle corresponds to a run with target only, and the spectrum at the bottom corresponds to a run with the complete plunger (target and degrader). In order to select ^{71}C ions and cut some of the contaminants from the incoming beam, we set a TOF gate for each run and we separated the corresponding data. The same method was used to identify incoming ^{73}Cu particles.

6.2.2 Outgoing particle identification

One of the quantities we used to identify particles leaving the target is the OS TOF, which is the time-of-flight through the S800 spectrometer. Ideally, particles with the same mass/charge ratio M/Q should have the same time-of-flight T through the S800 spectrometer, according to the equation

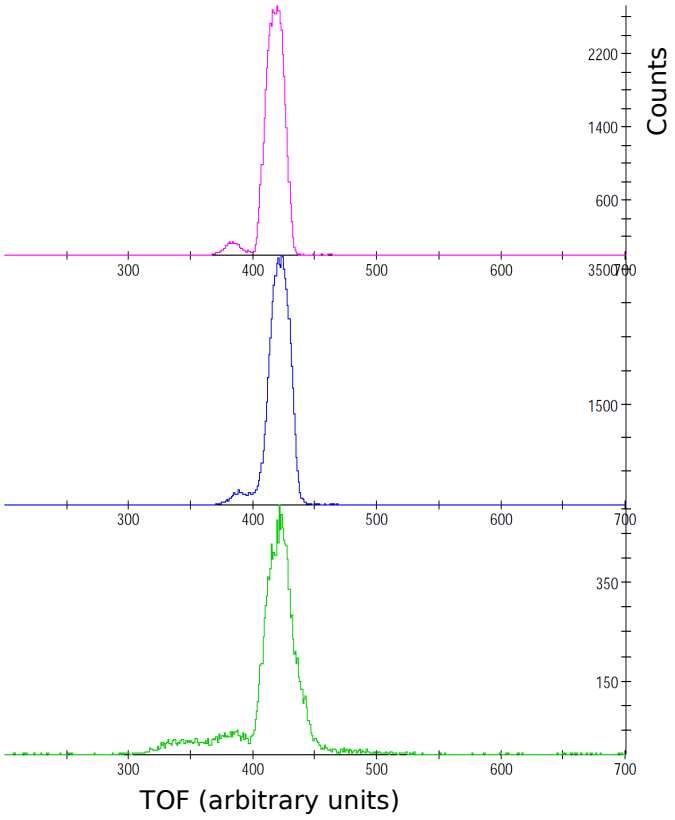


Figure 6.7: TOF spectra used for the particle identification of the ^{71}Cu incoming beam. The time of flight on the horizontal axis is expressed in arbitrary units.

$$\frac{M}{Q} = B\rho\frac{T}{L} \tag{6.1}$$

where Bρ is the magnetic rigidity of the system and L is the path length. In reality, the length of the path through the spectrometer is not the same for all particles. Actual trajectories are spread around the central trajectory and have different lengths. As a result there is a correlation between the time-of-flight and the position and angle of the trajectory of the particle measured at the S800 focal plane. For example, Figure 6.8 shows the correlation between the measured TOF and the angle in the X direction.

In order to calculate a corrected time-of-flight that is dependent on M/Q, as desired, but not dependent on the position and angles at the focal plane, we used the following expression:

$$T_c = T_m + a_x \cdot x + a_y \cdot y + a_\eta \cdot \eta + a_\zeta \cdot \zeta \tag{6.2}$$

where T_c is the corrected TOF, T_m is the measured TOF, η and ζ are the angles in the dispersive direction X and non-dispersive direction Y, respectively. The set of parameters α_i was adjusted empirically for each run. Figure 6.9 is analogous to Figure 6.8. The corrected TOF is shown on the horizontal axis.

Another quantitiy we used to identify outgoing particles is their energy loss in the ion chamber. Depending on the position and angle of the trajectory of particles as they enter the ion chamber, the length of their path inside the chamber can be different, so their energy loss can be different too. We corrected for this effect using an equation analogous to equation 6.2. The four parameters used to calculate the corrected energy loss were adjusted empirically for each run.

Once we had all the empirical parameters needed to calculate the corrected time-of-flight and the corrected energy loss, we used them to build the particle identification (ID) plots. Figures 6.10, 6.11, and 6.12 show the particle ID plots for the runs dedicated to the

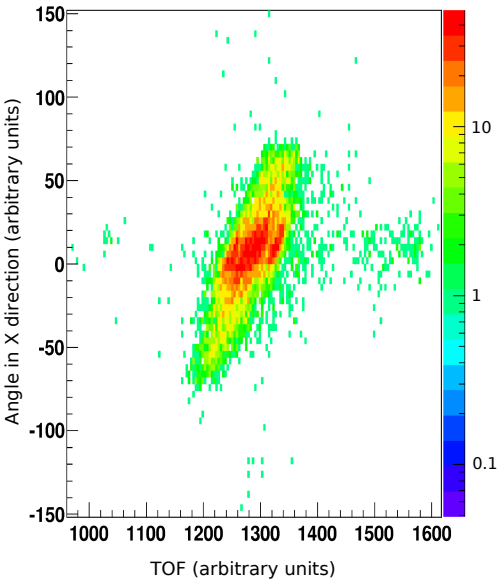


Figure 6.8: Uncorrected TOF-angle plot for one of the experimental runs. The TOF is on the horizontal axis, and the angle in the X direction is on the vertical axis. This figure shows that there is a correlation between the two quantities.

unreacted beam of ^{71}Cu (without plunger, with target only, and with plunger, respectively). In all of the following particle ID plots, the corrected time-of-flight is on the horizontal axis, while the corrected energy loss is on the vertical axis. Figure 6.13 was produced from the runs with a target-degrader distance of 1 mm, and the S800 set for ^{70}Ni. The black closed curve is the two-dimensional gate used to select ^{70}Ni. The correct identification was confirmed by the corresponding gamma spectra, where we were able to identify known transisions. The gamma spectra will be discussed in the next section. Figures from 6.14 to 6.17 are the particle ID plots with the gates used to select the outgoing beams of ^{73}Cu and ^{72}Ni.

The two-dimensional gates were then used to select the data belonging to the Cu unreacted beams, or the Ni (reacted) beams. The data from Ni were used to sort and build the gamma spectra.

6.3 Gammas from ^{70}Ni

Figure 6.18 shows the gamma spectra for ^{70}Ni with target only. The two peaks correspond to the $4_1^+ \rightarrow 2_1^+$ transition at 970 keV and the $2_1^+ \rightarrow 0_{gs}^+$ transition at 1260 keV. These spectra are Doppler-corrected with $\beta = 0.369$. This value of β was adjusted so that the peaks in the forward and in the backward ring appear at the same energy. The same spectra were also used to estimate the direct feeding of the 4_1^+ and 2_1^+ states, and the feeding of the 2_1^+ from the 4_1^+ state. The feeding of the 2_1^+ state was 55% direct and 45% from the 4_1^+ state.

In Figure 6.19 shows the spectra when the whole plunger is present (i.e. both target and degrader) and the distance d between target and degrader is 10 mm. In that case most transitions occurred before the degrader, so the peaks in the figure appear aligned at the correct energy. Figure 6.20 shows the same kind of spectra but in that case the distance d is only 0.1 mm. In that case most transitions occurred after the degrader, but the Doppler correction applied corresponds to the velocity before the target, so the peaks

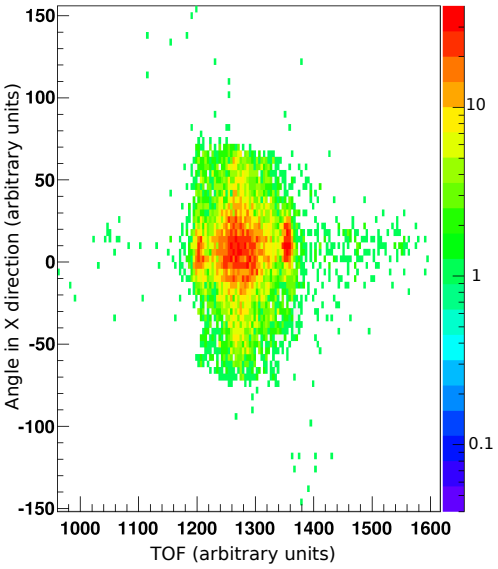


Figure 6.9: Corrected TOF-angle plot for the same experimental run as in Figure 6.8. The corrected TOF is on the horizontal axis, and the angle in the X direction is on the vertical axis.

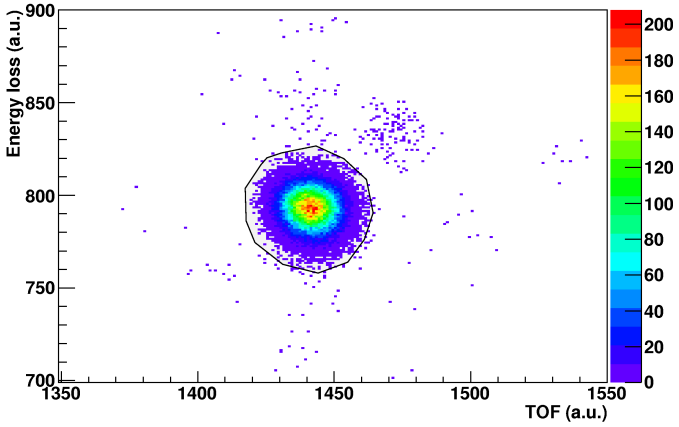


Figure 6.10: Particle ID plot for runs without plunger, S800 set for ^{71}Cu. The black closed curve is the two-dimensional gate used to select ^{71}Cu.

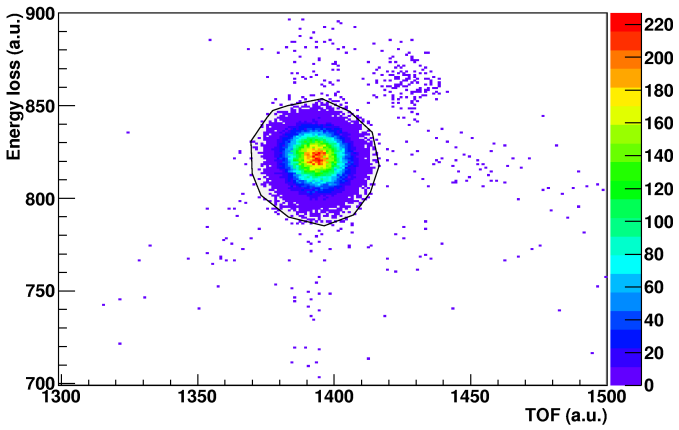


Figure 6.11: Particle ID plot for runs with target only, S800 set for ^{71}Cu. The black closed curve is the two-dimensional gate used to select ^{71}Cu.

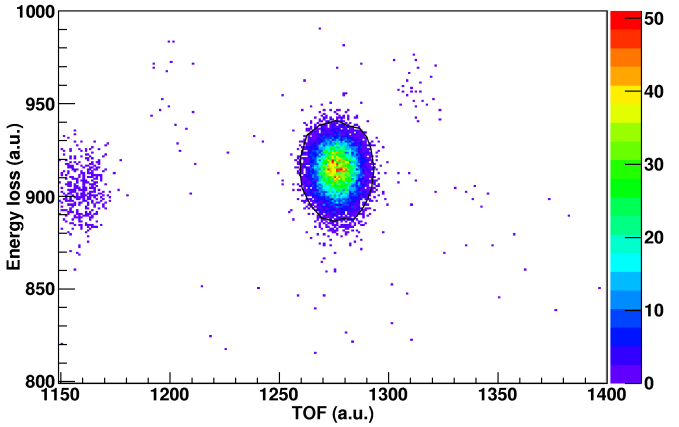


Figure 6.12: Particle ID plot for runs with plunger, S800 set for ^{71}Cu. The black closed curve is the two-dimensional gate used to select ^{71}Cu.

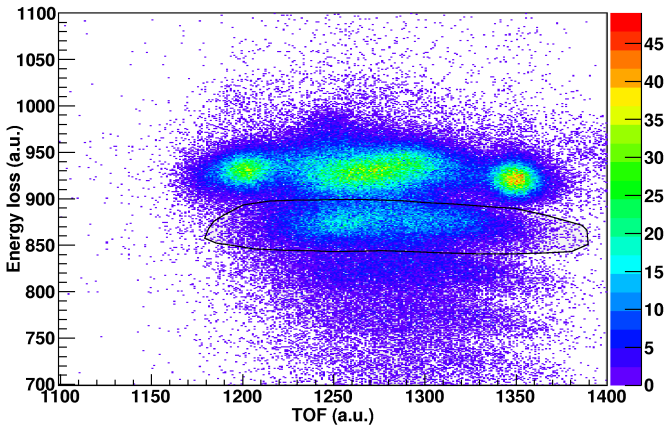


Figure 6.13: Particle ID plot for runs with plunger, S800 set for ^{70}Ni. The black closed curve is the two-dimensional gate used to select ^{70}Ni.

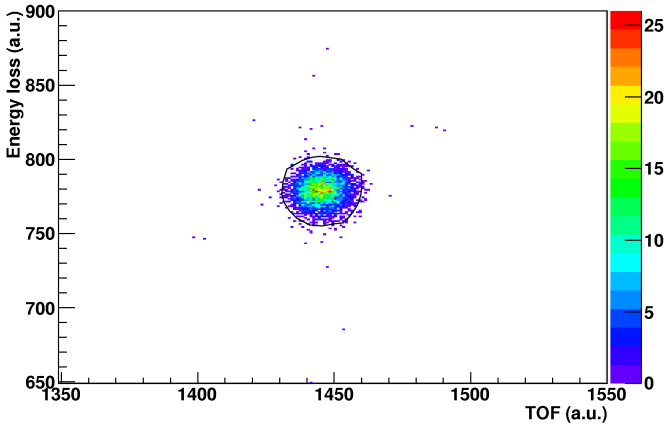


Figure 6.14: Particle ID plot for runs without plunger, S800 set for ^{73}Cu. The black closed curve is the two-dimensional gate used to select ^{73}Cu.

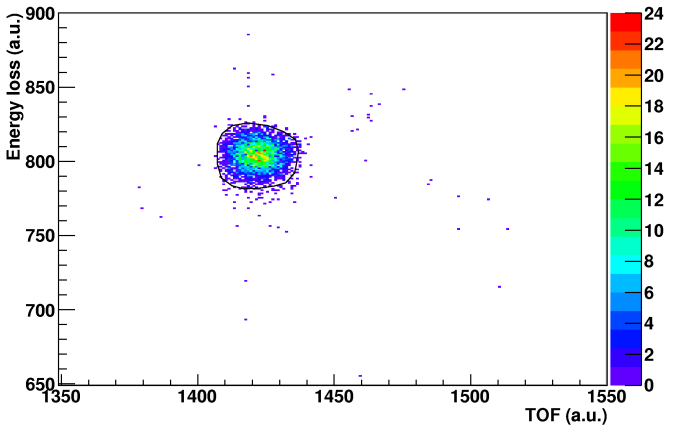


Figure 6.15: Particle ID plot for runs with target only, S800 set for ^{73}Cu. The black closed curve is the two-dimensional gate used to select ^{73}Cu.

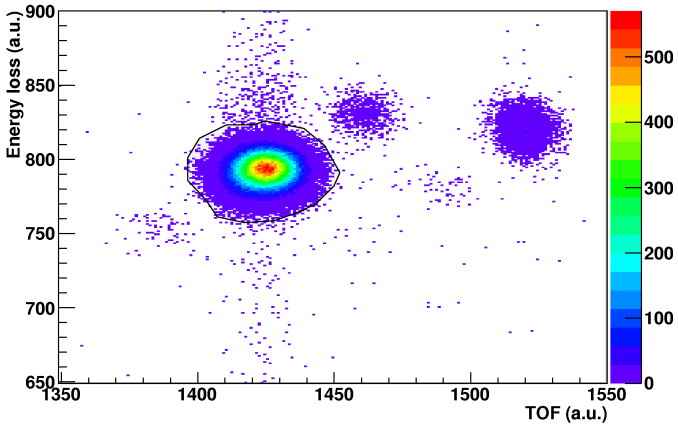


Figure 6.16: Particle ID plot for runs with plunger, S800 set for ^{73}Cu. The black closed curve is the two-dimensional gate used to select ^{73}Cu.

are no longer aligned at the correct energy. As expected, the peaks in the forward ring are shifted towards lower energies, and the peaks in the backward ring are shifted toward higher energies.

Figure 6.21 shows the gamma spectra measured by the forward array with the plunger set at three different target-degrader distances. The $4_1^+ \rightarrow 2_1^+$ transition at 970 keV is not well visible above the background, but the $2_1^+ \rightarrow 0_{gs}^+$ transition at 1260 keV is quite well defined. The peak due to radiation emitted before the degrader (also called the "fast peak") appears at the correct energy, and is most prominent when the distance d is larger, as expected. The peak due to radiation emitted after the degrader (also called the "slow peak") appears shifted, because of the different velocity of the emitting nucleus, and is most prominent when the distance d is smaller. When the distance d is 1 mm the two peaks are both clearly present, with comparable intensities.

6.4 Particle tracking

The position (x, y) and angles (η, ζ) of the trajectory of each particle are measured at the focal plane of the S800, and that information is used to calculate the position and angles back at the target. This tracking requires the calculation of the so-called inverse map. Each inverse map, calculated automatically at the request of the experimenter, relates the quantities measured at the focal plane to those at the target. The aberrations of the system, due to non-uniform fringe magnetic fields, are calculated from magnetic field measurement and taken into account when calculating the transport of ions through the spectrometer [Bazin et al., 2003]. The experimental positions and angles of the trajectories are used as a reference for the GEANT4 simulation of the beam.

Table 6.2: List of the main beam parameters that need to be adjusted in the simulations. See text for details.

Parameter	Unit	Short description
Beam In E	MeV/u	Energy per nucleon of incoming beam
dp	MeV	Average momentum of outgoing nucleon
dp FWHM	Mev	FWHM of momentum distribution of outgoing nucleon
Ata	mrad	Angle with respect to optical axis in dispersive plane
Bta	mrad	Angle with respect to optical axis in non-dispersive plane
max Ata	mrad	Angular divergence in dispersive plane
max Bta	mrad	Angular divergence in non-dispersive plane
Y	mm	Position in the non-dispersive direction at the focal plane
DY	mm	Y size for incoming beam at the focal plane
Low Dta	‰	Low limit for Dta fit
High Dta	‰	High limit for Dta fit
Beam In Bρ	Tm	Magnetic rigidity for the incoming beam

6.5 Simulations

GEANT4 [Agostinelli et al., 2003, Allison et al., 2006] was used to run simulations of this experiment. We used a simulation tool specifically developed for plunger measurements at NSCL [Adrich et al., 2009]. The simulation included the incoming beam, the beam pipe, the target, the degrader, and the SeGa arrays. Many parameters describing the beam could be adjusted so that the actual beam was reproduced as closely as possible. Table 6.2 contains a list of adjustable beam parameters. The outgoing nucleon mentioned in the table indicates the proton ejected from the nucleus in the proton-knockout reaction used to produce ^{70}Ni as the beam traversed the target. Ata and Bta are the angles that describe the direction of the trajectory at the target position. Max Ata and max Bta measure the angular divergence of the beam at the target position. Dta indicates the difference in kinetic energy with respect to the particles in the central trajectory.

A schematic drawing in figure 6.22 illustrates how the angles Ata and max Ata are defined in the dispersive plane. The angles Bta and max Bta are the defined the same way in the non-dispersive plane.

Figure 6.23 shows the results of a simulation of the unreacted ^{71}Cu beam going through the plunger. The simulation (in blue) is compared to the corresponding measurement (in red). Once the optimal beam parameters for the simulations were established, we simulated the gamma spectra emitted by those beams. The simulations included both direct feeding of the 2^+ and 4^+ excited state, and indirect feeding of the 2^+ state from the $4^+ \rightarrow 2^+$ transition. The fraction of 2^+ population coming from indirect feeding was estimated from the experimental runs with target only. The half-life of each state was treated as a free parameter.

6.5.1 Half-life of ^{70}Ni excited states

A good method to find the value of the lifetime for an excited state would be to choose a reasonable range of values for the lifetime, run the simulation for each of those values, and calculate the chi-square value as a measure of the goodness of fit to the experimental data. Then the chi-square values could be plotted versus the corresponding lifetimes, and the minimum of the curve would correspond to the lifetime of the state. This method has been applied successfully for other lifetime measurements with the plunger system, see for example [Petri et al., 2011]. We tried to apply it to the half-life of ^{70}Ni excited states, but it was not successful, probably because the experimental spectra are too noisy. The calculated chi-square values were too erratic and did not exhibit a clear minimum.

We tried to obtain a better agreement between simulations and measurements. The degrader thickness in the simulations was changed to better reproduce the experimental data. The thickness declared by the vendors may not be accurate, and a measurement with a caliper was ineffective because of the softness of the target material (gold). In a future experiment it would be advisable to run part of the measurements with the beam going through the target only. The energy loss in the target will give an accurate measurement of the target thickness. The angles of the germanium detectors with respect to the beam line and the position of the plunger along the beam line were adjusted. The simulated number

of reactions happening in the degrader was changed. The agreement between simulations and measurement was improved, but still not enough to reliably use the chi-square method.

Sseveral methods were tried in an attempt to obtain cleaner gamma spectra from our measurements. More accurate adjustments of the TOF and energy loss corrections discussed in Section 6.2.2 were performed, trying to obtain a cleaner separation between different nuclei in the two-dimensional plots used for particle identification. Both smaller and larger 2D gates in the particle ID plots for the outgoing beam were tried. A smaller gate should be more effective in cutting out unwanted contaminants, but a larger gate may allow to collect more of the gammas of interest. Similar attempts were made also with the TOF gate for the incoming beam. Despite our efforts, we couldn't obtain less noisy gamma spectra.

Figures 6.24, 6.25, and 6.26 show measured gamma spectra for ^{70}Ni, together with simulations, with the target-degrader distance set at 10 mm, 1 mm and 0.1 mm, respectively. The agreement between simulations and measurements is qualitatively good, especially for the forward detectors array. The agreement is somewhat poorer for the spectra collected by the backward array, because there are materials holding the backward detectors that are not included in the simulations. These simulations were run with a half-life of 14 ps for the $4^+ \rightarrow 2^+$ transition, and a half-life of 8 ps for the $2^+ \rightarrow 0^+_{gs}$ transition. This result suggests a weaker proton core polarization than indicated in [Perru et al., 2006].

Figure 6.27 shows an attempt to fit the experimental data with a simulation where the half-life of the 2^+ state is 1 ps. Even by changing significantly other parameters, like for example the feeding from the 4^+ state and the half-life of the 4^+ state, it was not possible to obtain an acceptable fit. When the plunger-degrader distance is as short as 0.1 mm, as in Figures 6.26 and 6.27, only the "slow peak" is clearly visible in our data, indicating that the vast majority of ^{70}Ni nuclei decay after traversing the degrader. With a half-life of the order of 1 ps the "fast peak" and the "slow peak" would have comparable intensities at d=0.1 mm. Since in our experiment the intensity of the "slow peak" is much greater than

the intensity of the "fast peak" at d=0.1mm, we conclude that the expected half-life of the order of 1 ps [Perru et al., 2006] for the 2^+ state is not compatible with our data.

6.6 Summary

A new measurement of the half life of the 2_1^+ excited state in ^{70}Ni has been performed with the plunger method. The result is a half life of the order of 10 ps, which is significantly longer than the half life of the order of 1 ps from a previous experiment [Perru et al., 2006] that was based on Coulomb excitation. Although the analysis of the new experiment is still in progress, it is clear that the new experimental data are not compatible with the results reported by [Perru et al., 2006]. In view of our result, we cannot confirm the claims [Perru et al., 2006] of significant changes in the nuclear structure of nickel isotopes. The longer lifetime is closer to what was predicted by the calculations of [Lisetskiy et al., 2005], which include to some degree a core-breaking effect. Recent measurements of ^{74}Ni [deAngelis et al., 2011] are in contradiction with the previous measurement by [Aoi et al., 2010], who like [Perru et al., 2006] postulated the effects of enhanced collectivity. Further experiments are planned to disentangle these conflicting results.

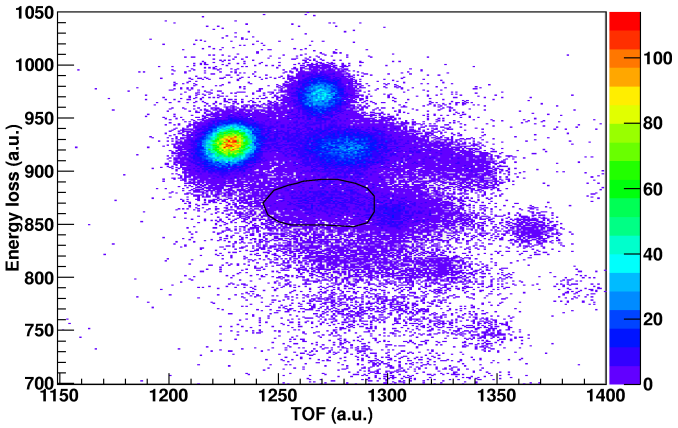


Figure 6.17: Particle ID plot for runs with plunger, S800 set for ^{72}Ni. The black closed curve is the two-dimensional gate used to select ^{72}Ni.

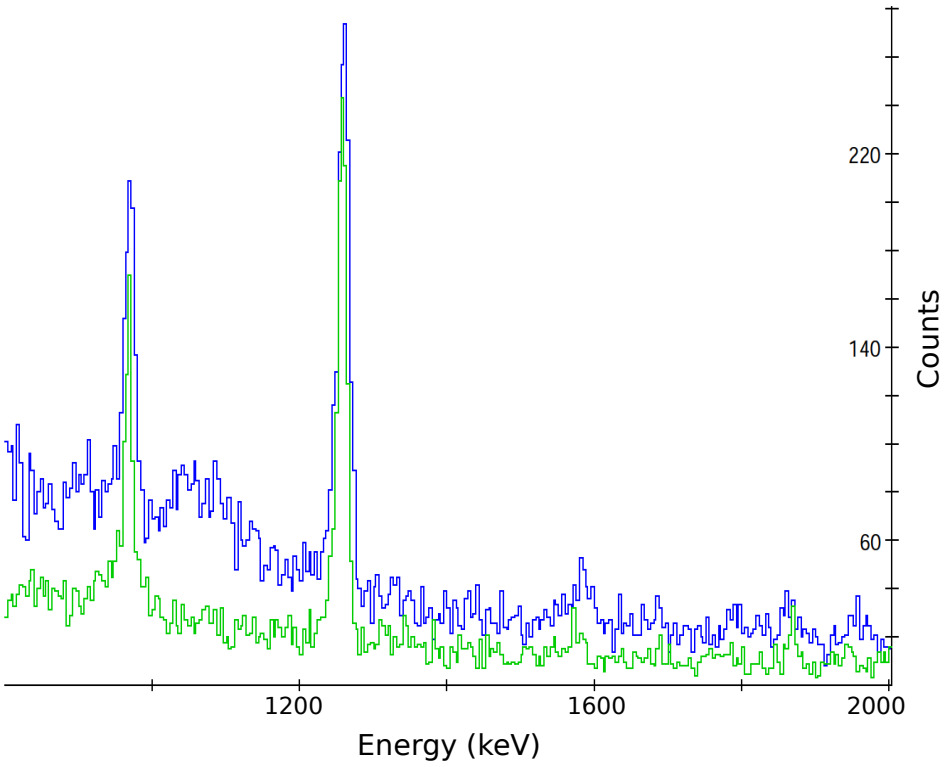


Figure 6.18: ^{70}Ni gamma spectra with target only. Blue: forward array. Green: backward array. The spectra are Doppler-corrected with $\beta = 0.369$.

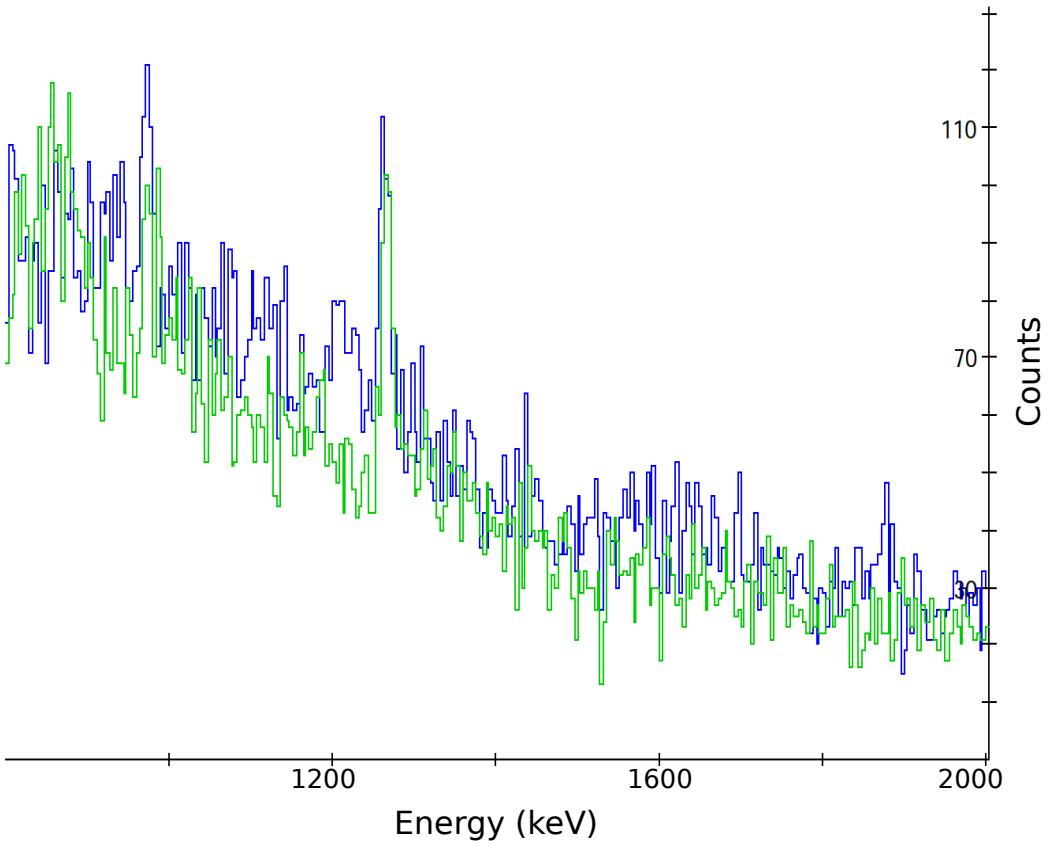


Figure 6.19: Doppler-corrected ^{70}Ni gamma spectra with plunger, d=10 mm. Blue: forward array. Green: backward array. The spectra are Doppler-corrected with $\beta = 0.369$.

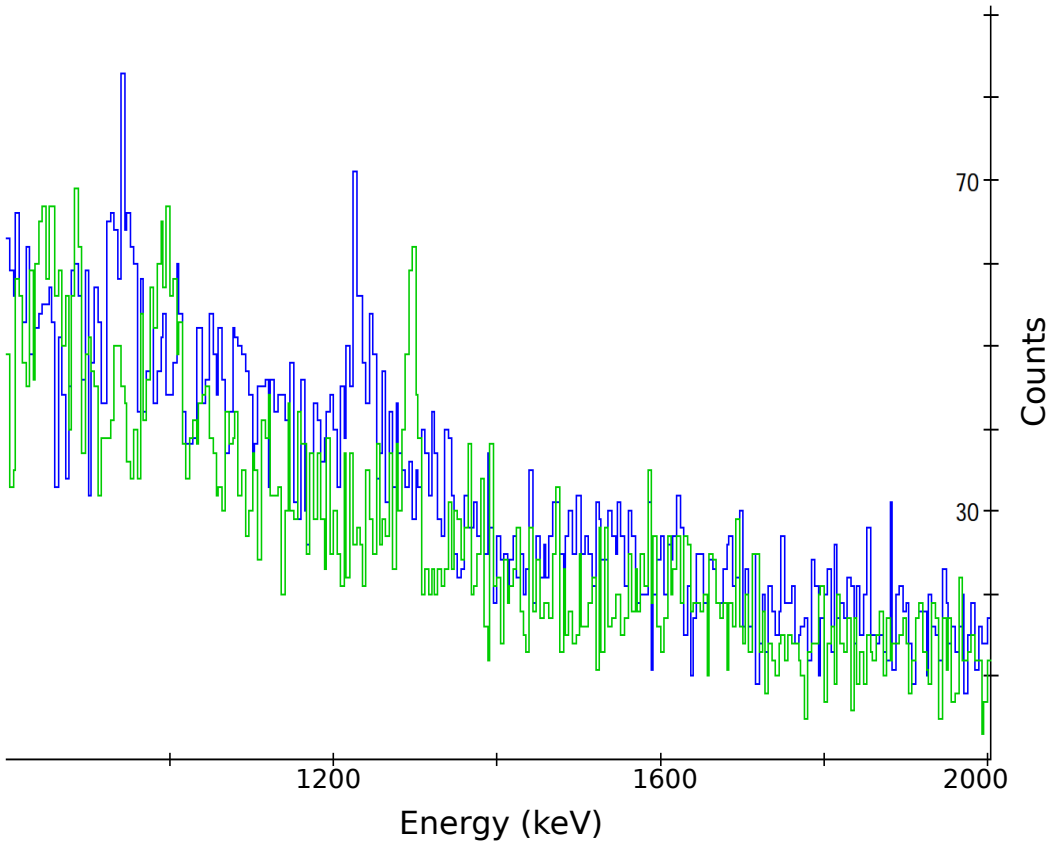


Figure 6.20: Doppler-corrected ^{70}Ni gamma spectra with plunger, d=0.1 mm. Blue: forward array. Green: backward array. The spectra are Doppler-corrected with $\beta = 0.369$.

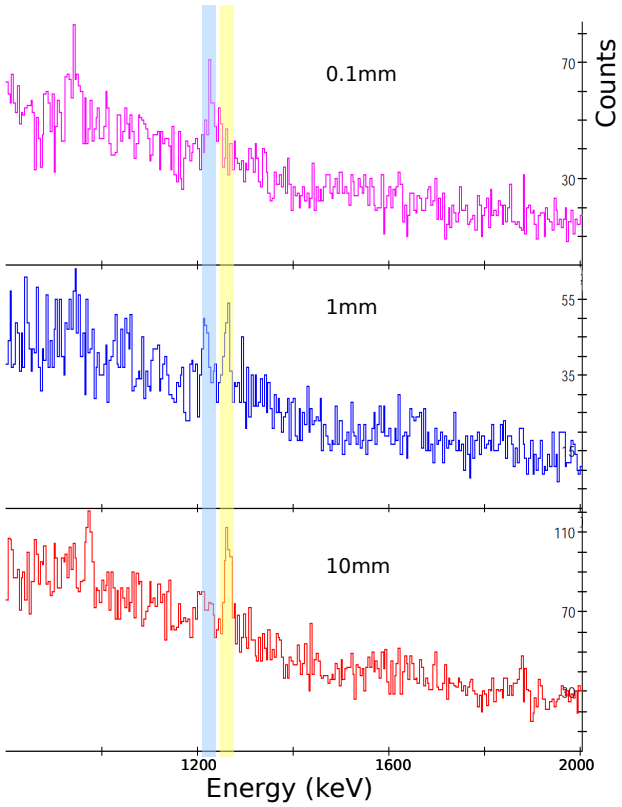


Figure 6.21: Doppler-corrected ^{70}Ni gamma spectra measured by the forward array. Upper panel: d=0.1 mm. Middle panel: d=1 mm. Lower panel: d=10 mm. The yellow shaded region shows the position of the $2^+ \rightarrow 0^+$ peak at the correct energy, corresponding to gammas emitted before the degrader. The blue shaded region shows the shifted peak, corresponding to gammas emitted after the degrader.

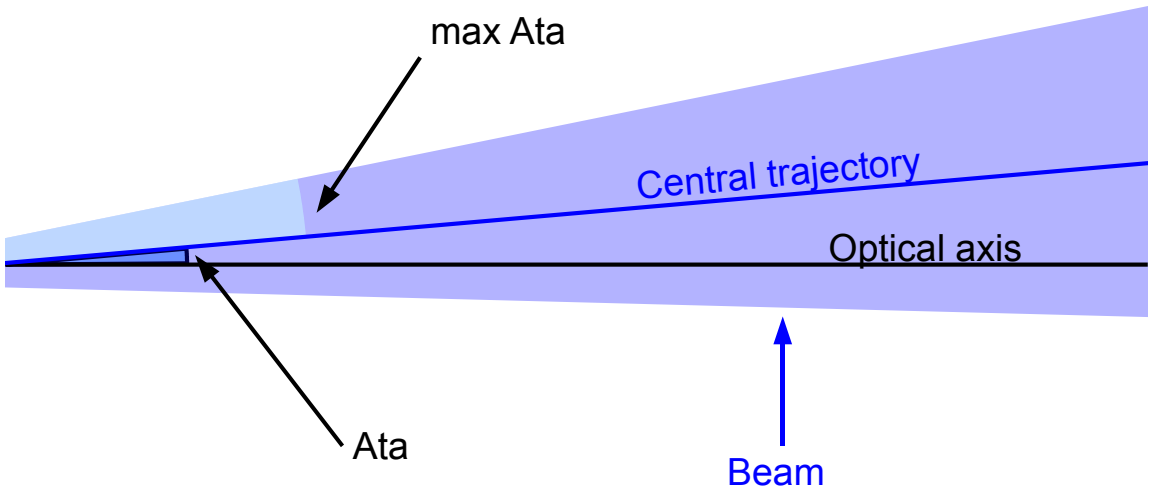


Figure 6.22: Schematic drawing of the beam at the focal plane. The angles Ata and max Ata are measured in the dispersive plane. An analogous drawing would illustrate the angles Bta and max Bta, measured in the non-dispersive plane.

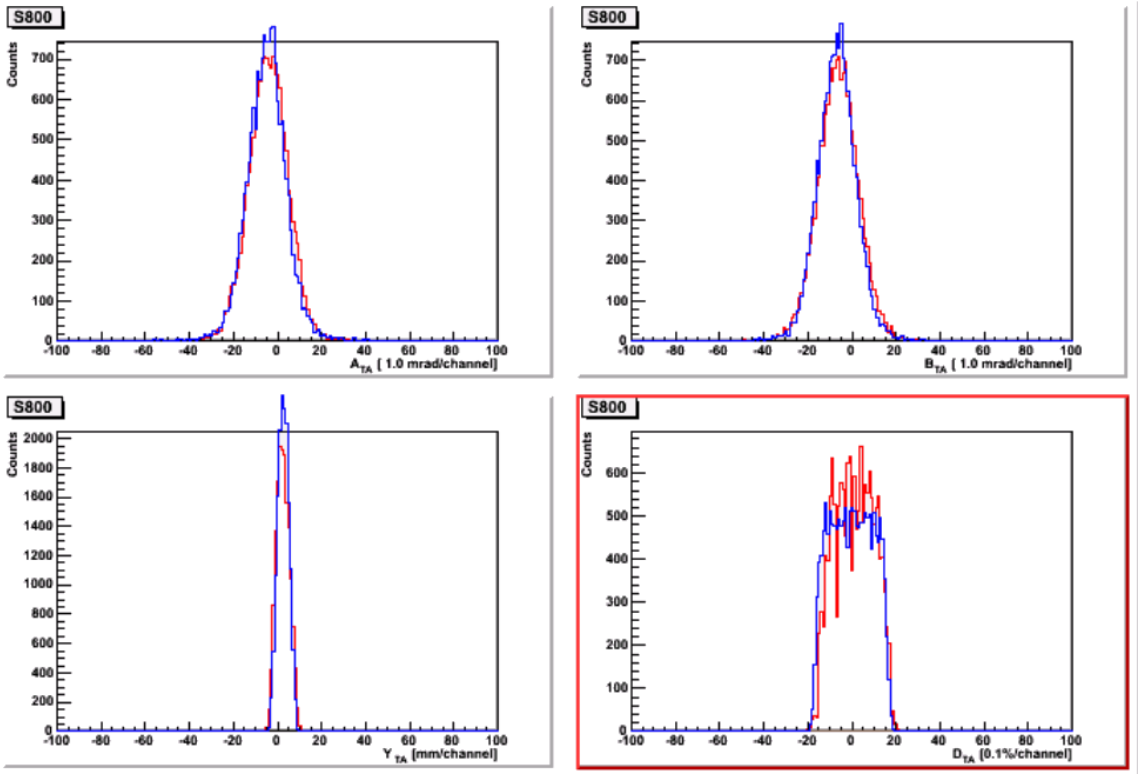


Figure 6.23: Simulation (in blue) and measurement (in red) of the unreacted ^{71}Cu beam going through the plunger. Upper left: Ata (angle with respect to optical axis in the dispersive plane). Upper right: Bta (angle with respect to optical axis in the non-dispersive plane). Lower left: Y (position in the non-dispersive direction). Lower right: Dta (difference in kinetic energy with respect to the particles in the central trajectory).

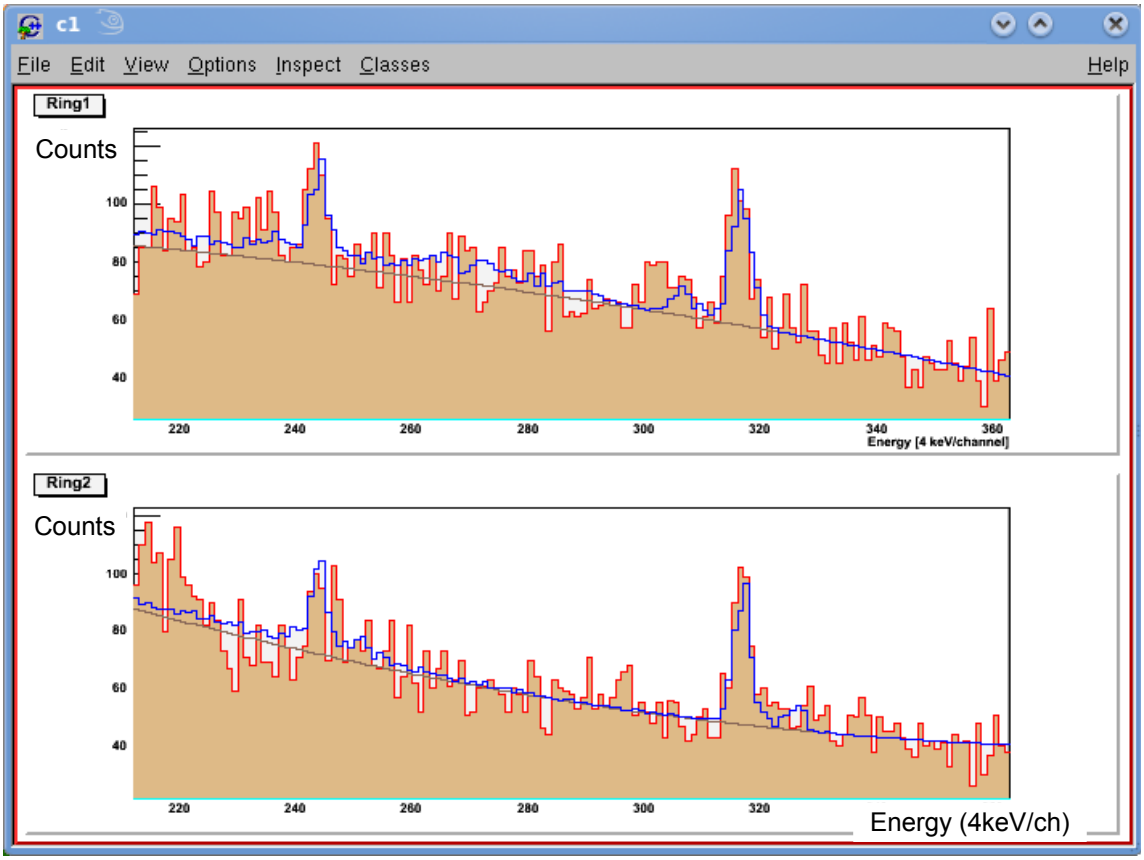


Figure 6.24: Gamma spectra for ^{70}Ni, with d=10 mm. The measurement is in red, and the simulation is in blue. Upper panel: forward ring. Lower panel: backward ring.

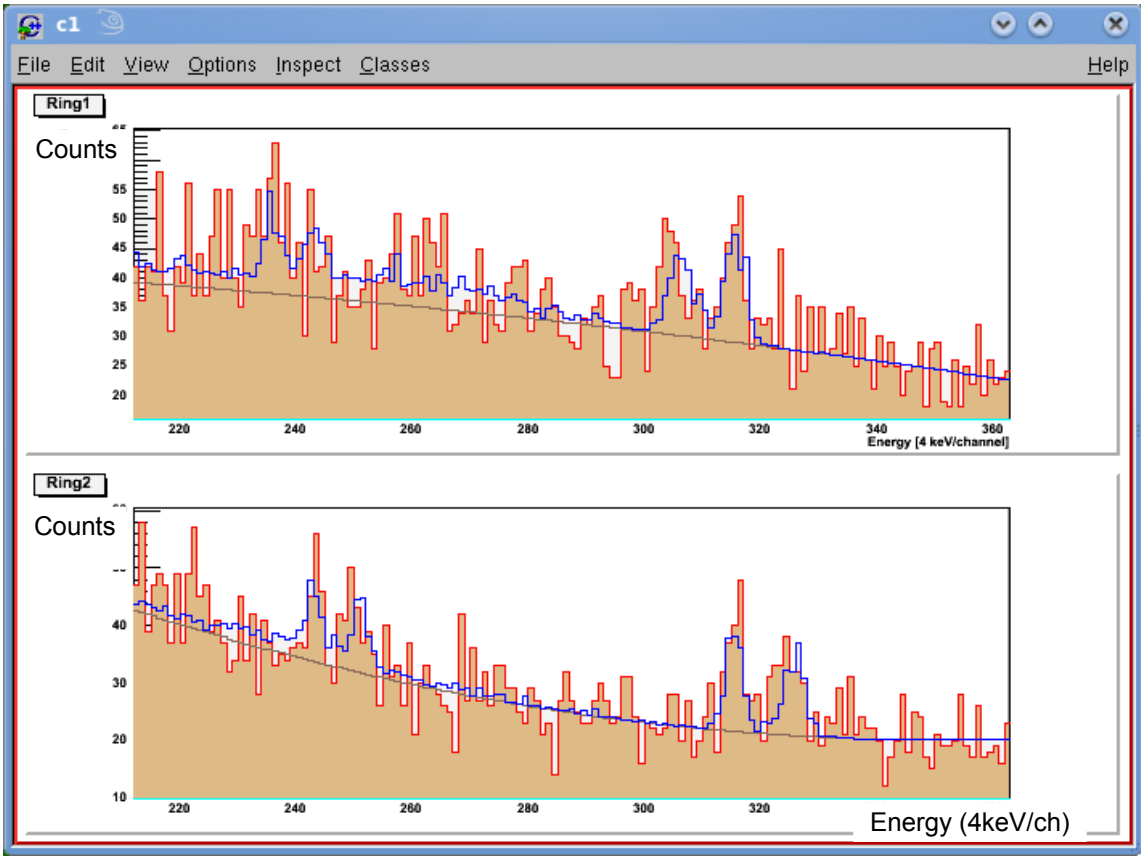


Figure 6.25: Gamma spectra for ^{70}Ni, with d=1 mm. The measurement is in red, and the simulation is in blue. Upper panel: forward ring. Lower panel: backward ring.

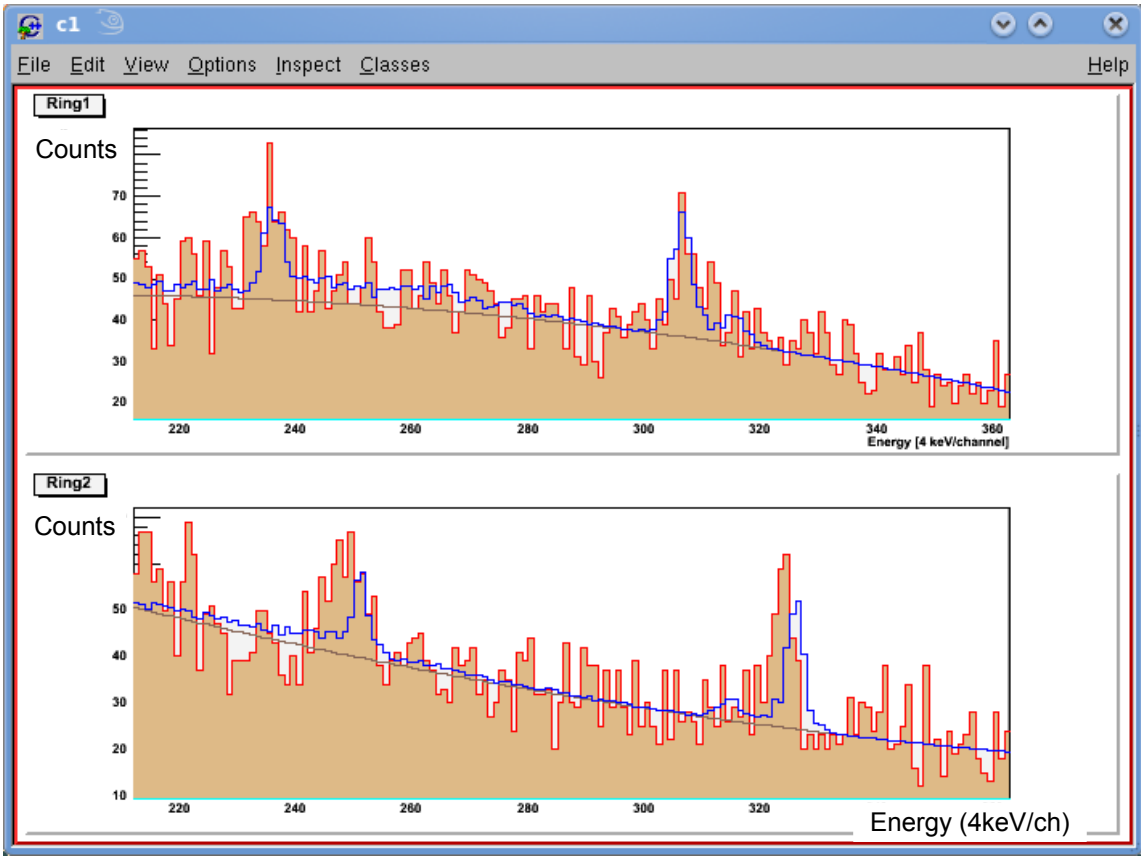


Figure 6.26: Gamma spectra for ^{70}Ni, with d=0.1 mm. The measurement is in red, and the simulation is in blue. Upper panel: forward ring. Lower panel: backward ring.

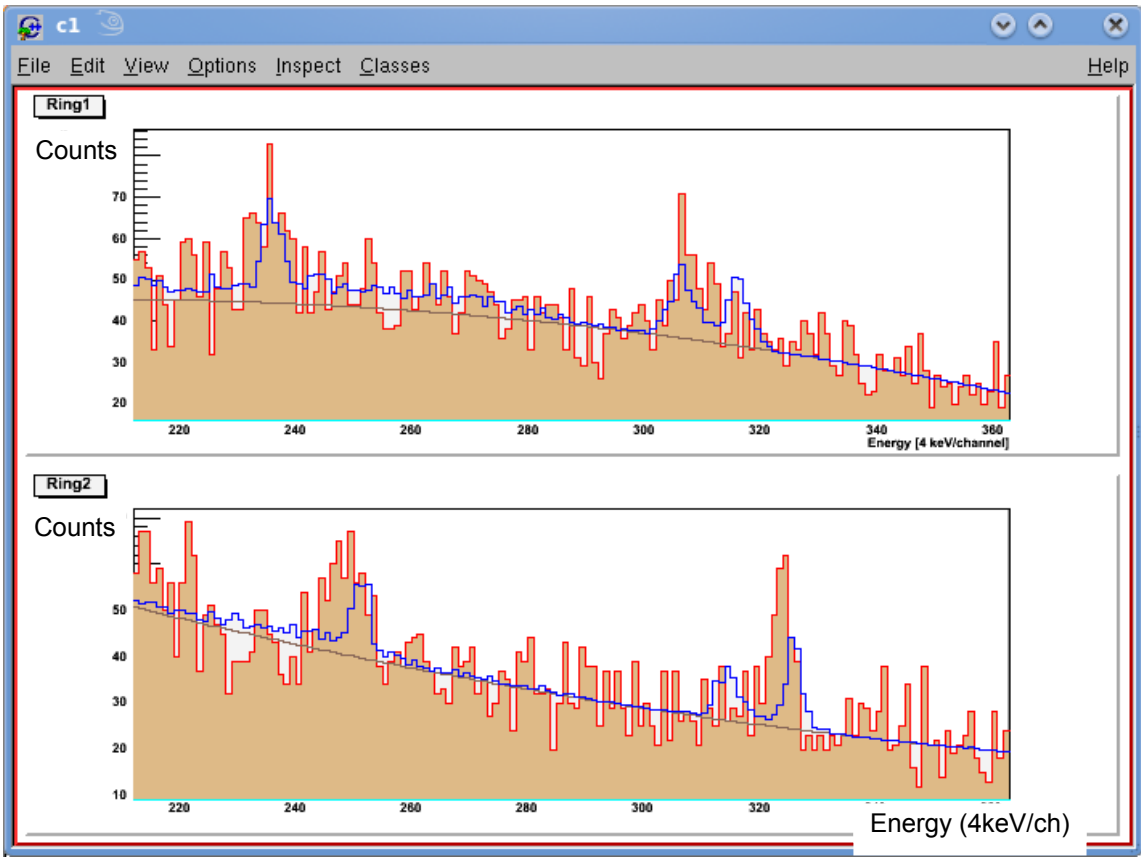


Figure 6.27: Gamma spectra for ^{70}Ni, with d=0.1 mm. The measurement is in red, and the simulation is in blue. Upper panel: forward ring. Lower panel: backward ring. The simulation corresponds to a half life of 1 ps for the 2^+ state.

Bibliography

Bibliography

[Adrich et al., 2009] Adrich, P., Enderich, D., Miller, D., Moeller, V., Norris, R., Starosta, K., Vaman, C., Voss, P., and Dewald, A. (2009). A simulation tool for Recoil Distance Method lifetime measurements at NSCL. *Nuclear Instruments and Methods in Physics Research Section A: Accelerators, Spectrometers, Detectors and Associated Equipment*, 598(2):454 – 464.

[Agostinelli et al., 2003] Agostinelli, S., Allison, J., Amako, K., Apostolakis, J., Araujo, H., Arce, P., Asai, M., Axen, D., Banerjee, S., Barrand, G., Behner, F., Bellagamba, L., Boudreau, J., Broglia, L., Brunengo, A., Burkhardt, H., Chauvie, S., Chuma, J., Chytracek, R., Cooperman, G., Cosmo, G., Degtyarenko, P., Dell'Acqua, A., Depaola, G., Dietrich, D., Enami, R., Feliciello, A., Ferguson, C., Fesefeldt, H., Folger, G., Foppiano, F., Forti, A., Garelli, S., Giani, S., Giannitrapani, R., Gibin, D., Cadenas, J. G., Gonzlez, I., Abril, G. G., Greeniaus, G., Greiner, W., Grichine, V., Grossheim, A., Guatelli, S., Gumplinger, P., Hamatsu, R., Hashimoto, K., Hasui, H., Heikkinen, A., Howard, A., Ivanchenko, V., Johnson, A., Jones, F., Kallenbach, J., Kanaya, N., Kawabata, M., Kawabata, Y., Kawaguti, M., Kelner, S., Kent, P., Kimura, A., Kodama, T., Kokoulin, R., Kossov, M., Kurashige, H., Lamanna, E., Lampn, T., Lara, V., Lefebure, V., Lei, F., Liendl, M., Lockman, W., Longo, F., Magni, S., Maire, M., Medernach, E., Minamimoto, K., de Freitas, P. M., Morita, Y., Murakami, K., Nagamatu, M., Nartallo, R., Nieminen, P., Nishimura, T., Ohtsubo, K., Okamura, M., O'Neale, S., Oohata, Y.,

Paech, K., Perl, J., Pfeiffer, A., Pia, M., Ranjard, F., Rybin, A., Sadilov, S., Salvo, E. D., Santin, G., Sasaki, T., Savvas, N., Sawada, Y., Scherer, S., Sei, S., Sirotenko, V., Smith, D., Starkov, N., Stoecker, H., Sulkimo, J., Takahata, M., Tanaka, S., Tcherniaev, E., Tehrani, E. S., Tropeano, M., Truscott, P., Uno, H., Urban, L., Urban, P., Verderi, M., Walkden, A., Wander, W., Weber, H., Wellisch, J., Wenaus, T., Williams, D., Wright, D., Yamada, T., Yoshida, H., and Zschiesche, D. (2003). Geant4a simulation toolkit. *Nuclear Instruments and Methods in Physics Research Section A: Accelerators, Spectrometers, Detectors and Associated Equipment*, 506(3):250 – 303.

[Allison et al., 2006] Allison, J., Amako, K., Apostolakis, J., Araujo, H., Dubois, P., Asai, M., Barrand, G., Capra, R., Chauvie, S., Chytracek, R., Cirrone, G., Cooperman, G., Cosmo, G., Cuttone, G., Daquino, G., Donszelmann, M., Dressel, M., Folger, G., Foppiano, F., Generowicz, J., Grichine, V., Guatelli, S., Gumplinger, P., Heikkinen, A., Hrivnacova, I., Howard, A., Incerti, S., Ivanchenko, V., Johnson, T., Jones, F., Koi, T., Kokoulin, R., Kossov, M., Kurashige, H., Lara, V., Larsson, S., Lei, F., Link, O., Longo, F., Maire, M., Mantero, A., Mascialino, B., McLaren, I., Lorenzo, P., Minamimoto, K., Murakami, K., Nieminen, P., Pandola, L., Parlati, S., Peralta, L., Perl, J., Pfeiffer, A., Pia, M., Ribon, A., Rodrigues, P., Russo, G., Sadilov, S., Santin, G., Sasaki, T., Smith, D., Starkov, N., Tanaka, S., Tcherniaev, E., Tome, B., Trindade, A., Truscott, P., Urban, L., Verderi, M., Walkden, A., Wellisch, J., Williams, D., Wright, D., and Yoshida, H. (2006). Geant4 developments and applications. *Nuclear Science, IEEE Transactions on*, 53(1):270 –278.

[Aoi et al., 2010] Aoi, N., Kanno, S., Takeuchi, S., Suzuki, H., Bazin, D., Bowen, M., Campbell, C., Cook, J., Dinca, D.-C., Gade, A., Glasmacher, T., Iwasaki, H., Kubo, T., Kurita, K., Motobayashi, T., Mueller, W., Nakamura, T., Sakurai, H., Takashina, M., Terry, J., Yoneda, K., and Zwahlen, H. (2010). Enhanced collectivity in ^{74}Ni. *Physics Letters B*, 692(5):302 – 306.

[Audi et al., 2003] Audi, G., Bersillon, O., Blachot, J., and Wapstra, A. (2003). The nubase evaluation of nuclear and decay properties. *Nuclear Physics A*, 729(1):3 – 128.

[Bair et al., 1975] Bair, J. K., Biggerstaff, J. A., Jones, C. M., Larson, J. D., McConnell, J. W., Milner, W. T., and Ziegler, N. F. (1975). Design considerations for the ornl 25 mv tandem accelerator. *Nuclear Science, IEEE Transactions on*, 22(3):1655 –1658.

[Bazin et al., 2003] Bazin, D., Caggiano, J., Sherrill, B., Yurkon, J., and Zeller, A. (2003). The S800 spectrograph. *Nuclear Instruments and Methods in Physics Research Section B: Beam Interactions with Materials and Atoms*, 204(0):629 – 633.

[Blachot, 2005a] Blachot, J. (2005a). Nuclear Data Sheets for A = 113. *Nuclear Data Sheets*, 104(4):791 – 966.

[Blachot, 2005b] Blachot, J. (2005b). Nuclear Data Sheets for A = 115. *Nuclear Data Sheets*, 104(4):967 – 1110.

[Blachot, 2006] Blachot, J. (2006). Nuclear Data Sheets for A = 109. *Nuclear Data Sheets*, 107(2):355 – 506.

[Blachot, 2009] Blachot, J. (2009). Nuclear Data Sheets for A = 111. *Nuclear Data Sheets*, 110(6):1239 – 1407.

[Blank and Borge, 2008] Blank, B. and Borge, M. (2008). Nuclear structure at the proton drip line: Advances with nuclear decay studies. *Progress in Particle and Nuclear Physics*, 60(2):403 – 483.

[BNL, 2011] BNL (2011). National nuclear data center. `http://www.nndc.bnl.gov`.

[Chester et al., 2006] Chester, A., Adrich, P., Becerril, A., Bazin, D., Campbell, C., Cook, J., Dinca, D.-C., Mueller, W., Miller, D., Moeller, V., Norris, R., Portillo, M., Starosta, K., Stolz, A., Terry, J., Zwahlen, H., Vaman, C., and Dewald, A. (2006). Application of the time-of-flight technique for lifetime measurements with relativistic beams of heavy

nuclei. *Nuclear Instruments and Methods in Physics Research Section A: Accelerators, Spectrometers, Detectors and Associated Equipment*, 562(1):230 – 240.

[Clement et al., 2003] Clement, R., Benenson, W., Brown, B., Richter, W., Schatz, H., Sherrill, B., and Volya, A. (2003). Sensitivities of rp-process calculations to nuclear mass uncertainties. *Nuclear Physics A*, 718(0):617 – 619.

[Darby et al., 2010] Darby, I. G., Grzywacz, R. K., Batchelder, J. C., Bingham, C. R., Cartegni, L., Gross, C. J., Hjorth-Jensen, M., Joss, D. T., Liddick, S. N., Nazarewicz, W., Padgett, S., Page, R. D., Papenbrock, T., Rajabali, M. M., Rotureau, J., and Rykaczewski, K. P. (2010). Orbital dependent nucleonic pairing in the lightest known isotopes of tin. *Phys. Rev. Lett.*, 105:162502.

[deAngelis et al., 2011] deAngelis, G. et al. (2011). presented at the Joint ANL-HRIBF-NSCL Workshop, MSU, MI.

[Dombrádi et al., 1995] Dombrádi, Z., Nyakó, B. M., Perez, G. E., Algora, A., Fahlander, C., Seweryniak, D., Nyberg, J., Atac, A., Cederwall, B., Johnson, A., Kerek, A., Kownacki, J., Norlin, L.-O., Wyss, R., Adamides, E., Ideguchi, E., Julin, R., Juutinen, S., Karczmarczyk, W., Mitarai, S., Piiparinen, M., Schubart, R., Sletten, G., Törmänen, S., and Virtanen, A. (1995). High-spin spectroscopy of ^{109}Te. *Phys. Rev. C*, 51:2394–2399.

[Elomaa et al., 2009] Elomaa, V.-V., Vorobjev, G. K., Kankainen, A., Batist, L., Eliseev, S., Eronen, T., Hakala, J., Jokinen, A., Moore, I. D., Novikov, Y. N., Penttilä, H., Popov, A., Rahaman, S., Rissanen, J., Saastamoinen, A., Schatz, H., Seliverstov, D. M., Weber, C., and Äystö, J. (2009). Quenching of the SnSbTe Cycle in the *rp* Process. *Phys. Rev. Lett.*, 102(25):252501.

[Ferreira and Maglione, 2001] Ferreira, L. S. and Maglione, E. (2001). Odd-Odd Deformed Proton Emitters. *Phys. Rev. Lett.*, 86(9):1721–1724.

[Ginter, 1999] Ginter, T. N. (1999). *The new HRIBF recoil mass spectrometer: performance and first results.* PhD thesis, Vanderbilt University, TN.

[Gross et al., 1998] Gross, C. J., Akovali, Y. A., Baktash, C., Batchelder, J. C., Bingham, C. R., Carpenter, M. P., Davids, C. N., Davinson, T., Ellis, D., Galindo-Uribarri, A., Ginter, T. N., Grzywacz, R., Janssens, R. V. F., Johnson, J. W., Liang, J. F., Lister, C. J., Mas, J., MacDonald, B. D., Paul, S. D., Piechaczek, A., Radford, D. C., Reviol, W., Rykaczewski, K., a, W. S., Seweryniak, D., Shapira, D., Toth, K. S., Weintraub, W., Woods, P. J., Yu, C.-H., Zganjar, E. F., and Uusitalo, J. (1998). In-beam gamma-ray spectroscopy in the ground-state proton emitter ^{113}Cs. *AIP Conference Proceedings*, 455(1):444–449.

[Gross et al., 2000] Gross, C. J., Ginter, T. N., Shapira, D., Milner, W. T., McConnell, J. W., James, A. N., Johnson, J. W., Mas, J., Mantica, P. F., Auble, R. L., Das, J. J., Blankenship, J. L., Hamilton, J. H., Robinson, R. L., Akovali, Y. A., Baktash, C., Batchelder, J. C., Bingham, C. R., Brinkman, M. J., Carter, H. K., Cunningham, R. A., Davinson, T., Fox, J. D., Galindo-Uribarri, A., Grzywacz, R., Liang, J. F., MacDonald, B. D., MacKenzie, J., Paul, S. D., Piechaczek, A., Radford, D. C., Ramayya, A. V., Reviol, W., Rudolph, D., Rykaczewski, K., Toth, K. S., Weintraub, W., Williams, C., Woods, P. J., Yu, C.-H., and Zganjar, E. F. (2000). Performance of the Recoil Mass Spectrometer and its detector systems at the Holifield Radioactive Ion Beam Facility. *Nucl. Instr. and Meth. in Phys. Research A*, 450(1):12 – 29.

[Grzywacz, 2003] Grzywacz, R. (2003). Applications of digital pulse processing in nuclear spectroscopy. *Nucl. Instr. and Meth. in Phys. Research B*, 204:649 – 659.

[Hauschild and Jentschel, 2001] Hauschild, T. and Jentschel, M. (2001). Comparison of maximum likelihook estimation and chi-square statistic applied to counting experiments. *Nucl. Inst. and Meth. in Phys. Research A*, 457:384–401.

[Heine et al., 1991] Heine, F., Faestermann, T., Gillitzer, A., Homolka, J., Köpf, M., and Wagner, W. (1991). Proton and alpha radioactivity of very neutron deficient Te, I, Xe and Cs isotopes, studied after electrostatic separation. *Zeitschrift für Physik A Hadrons and Nuclei*, 340:225–226.

[Heine et al., 1992] Heine, F., Faestermann, T., Gillitzer, A., and Körner, H. J. (1992). Proton and alpha radioactivity in the vicinity of ^{100}Sn. In *Proceedings of the 6th Conference on Nuclei Far From Stability and the 9th International Conference on Atomic Masses and Fundamental Constants*, page 331.

[Hofmann, 1995] Hofmann, S. (1995). Proton radioactivity. *Radiochim. Acta*, 70/71:93.

[Hubbard-Nelson et al., 1999] Hubbard-Nelson, B., Momayezi, M., and Warburton, W. K. (1999). A module for energy and pulse shape data acquisition. *Nuclear Instruments and Methods in Physics Research Section A: Accelerators, Spectrometers, Detectors and Associated Equipment*, 422(1-3):411 – 416.

[Janas et al., 2005] Janas, Z., Mazzocchi, C., Batist, L., Blazhev, A., Grska, M., Kavatsyuk, M., Kavatsyuk, O., Kirchner, R., Korgul, A., La Commara, M., Miernik, K., Mukha, I., Płochocki, A., Roeckl, E., and Schmidt, K. (2005). Measurements of ^{110}Xe and ^{106}Te decay half-lives. *The European Physical Journal A - Hadrons and Nuclei*, 23:197–200. 10.1140/epja/i2004-10076-x.

[Jones, 1981] Jones, C. (1981). The 25 MV tandem accelerator at Oak Ridge. *Nuclear Instruments and Methods*, 184(1):145 – 151.

[Jones et al., 1989] Jones, C., Haynes, D., Juras, R., Meigs, M., Ziegler, N., Raatz, J., and Rathmell, R. (1989). Improved voltage performance of the Oak Ridge 25URC tandem accelerator. *Nuclear Instruments and Methods in Physics Research Section A: Accelerators, Spectrometers, Detectors and Associated Equipment*, 276(3):413 – 417.

[Karny et al., 2008] Karny, M., Rykaczewski, K. P., Grzywacz, R. K., Batchelder, J. C., Bingham, C. R., Goodin, C., Gross, C. J., Hamilton, J. H., Korgul, A., Królas, W., Liddick, S. N., Li, K., Maier, K. H., Mazzocchi, C., Piechaczek, A., Rykaczewski, K., Schapira, D., Simpson, D., Tantawy, M. N., Winger, J. A., Yu, C. H., Zganjar, E. F., Nikolov, N., Dobaczewski, J., Kruppa, A. T., Nazarewicz, W., and Stoitsov, M. (2008). Shell structure beyond the proton drip line studied via proton emission from deformed ^{141}Ho. *Phys. Lett. B*, 664(1-2):52 – 56.

[Kirchner et al., 1977] Kirchner, R., Klepper, O., Nyman, G., Reisdorf, W., Roeckl, E., Schardt, D., Kaffrell, N., Peuser, P., and Schneeweiss, K. (1977). New neutron-deficient tellurium, iodine, and xenon isotopes produced by reactions of 290 MeV ^{58}Ni ions on ^{58}Ni and ^{63}Cu targets. *Physics Letters B*, 70(2):150 – 154.

[Liddick et al., 2006] Liddick, S. N., Grzywacz, R., Mazzocchi, C., Page, R. D., Rykaczewski, K. P., Batchelder, J. C., Bingham, C. R., Darby, I. G., Drafta, G., Goodin, C., Gross, C. J., Hamilton, J. H., Hecht, A. A., Hwang, J. K., Ilyushkin, S., Joss, D. T., Korgul, A., Królas, W., Lagergren, K., Li, K., Tantawy, M. N., Thomson, J., and Wigner, J. A. (2006). Discovery of ^{109}Xe and ^{105}Te: Superallowed α Decay near Doubly Magic ^{100}Sn. *Phys. Rev. Lett.*, 97:082501.

[Lisetskiy et al., 2005] Lisetskiy, A. F., Brown, B. A., and Horoi, M. (2005). Exotic nuclei near 78ni in a shell model approach. In Gross, C. J., Nazarewicz, W., and Rykaczewski, K. P., editors, *The 4th International Conference on Exotic Nuclei and Atomic Masses*, pages 95–96. Springer Berlin Heidelberg.

[Macfarlane and Siivola, 1965] Macfarlane, R. D. and Siivola, A. (1965). New region of alpha radioactivity. *Phys. Rev. Lett.*, 14(4):114–115.

[Mang, 1960] Mang, H. J. (1960). Calculation of α-transition probabilities. *Phys. Rev.*, 119:1069–1075.

[Mazzocchi et al., 2007] Mazzocchi, C., Grzywacz, R., Liddick, S. N., Rykaczewski, K. P., Schatz, H., Batchelder, J. C., Bingham, C. R., Gross, C. J., Hamilton, J. H., Hwang, J. K., Ilyushkin, S., Korgul, A., Królas, W., Li, K., Page, R. D., Simpson, D., and Winger, J. A. (2007). α decay of ^{109}I and its implications for the proton decay of ^{105}Sb and the astrophysical rapid proton-capture process. *Phys. Rev. Lett.*, 98:212501.

[Möller et al., 1997] Möller, P., Nix, J. R., and Kratz, K.-L. (1997). Nuclear Properties for Astrophysical and Radioactive-Ion Beam Applications. *Atomic Data and Nuclear Data Tables*, 66:131–+.

[Morrissey et al., 2003] Morrissey, D., Sherrill, B., Steiner, M., Stolz, A., and Wiedenhoever, I. (2003). Commissioning the A1900 projectile fragment separator. *Nuclear Instruments and Methods in Physics Research Section B: Beam Interactions with Materials and Atoms*, 204(0):90 – 96.

[Page et al., 1994a] Page, R. D., Woods, P. J., Cunningham, R. A., Davinson, T., Davis, N. J., James, A. N., Livingston, K., Sellin, P. J., and Shotter, A. C. (1994a). Alpha Radioactivity above ^{100}Sn including the decay of ^{108}I. *Phys. Rev. C*, 49(6):3312.

[Page et al., 1994b] Page, R. D., Woods, P. J., Cunningham, R. A., Davinson, T., Davis, N. J., James, A. N., Livingston, K., Sellin, P. J., and Shotter, A. C. (1994b). Decays of odd-odd n-z=2 nuclei above ^{100}Sn: The observation of proton radioactivity from ^{112}Cs. *Phys. Rev. Lett.*, 72(12):1798.

[Perru et al., 2006] Perru, O., Sorlin, O., Franchoo, S., Azaiez, F., Bouchez, E., Bourgeois, C., Chatillon, A., Daugas, J. M., Dlouhy, Z., Dombrádi, Z., Donzaud, C., Gaudefroy, L., Grawe, H., Grévy, S., Guillemaud-Mueller, D., Hammache, F., Ibrahim, F., Le Coz, Y., Lukyanov, S. M., Matea, I., Mrazek, J., Nowacki, F., Penionzhkevich, Y.-E., de Oliveira Santos, F., Pougheon, F., Saint-Laurent, M. G., Sletten, G., Stanoiu, M., Stodel, C., Theisen, C., and Verney, D. (2006). Enhanced core polarization in ^{70}Ni and ^{74}Zn. *Phys. Rev. Lett.*, 96:232501.

[Petri et al., 2011] Petri, M., Fallon, P., Macchiavelli, A. O., Paschalis, S., Starosta, K., Baugher, T., Bazin, D., Cartegni, L., Clark, R. M., Crawford, H. L., Cromaz, M., Dewald, A., Gade, A., Grinyer, G. F., Gros, S., Hackstein, M., Jeppesen, H. B., Lee, I. Y., McDaniel, S., Miller, D., Rajabali, M. M., Ratkiewicz, A., Rother, W., Voss, P., Walsh, K. A., Weisshaar, D., Wiedeking, M., and Brown, B. A. (2011). Lifetime measurement of the 2_1^+ state in ^{20}**C**. *Phys. Rev. Lett.*, 107:102501.

[Rasmussen, 1959] Rasmussen, J. O. (1959). Alpha-decay barrier penetrabilities with an exponential nuclear potential: Even-even nuclei. *Phys. Rev.*, 113(6):1593–1598.

[Roeckl et al., 1980] Roeckl, E., Gowdy, G. M., Kirchner, R., Klepper, O., Piotrowski, A., Płochocki, A., Reisdorf, W., Tidemand-Petersson, P., Żylicz, J., Schardt, D., Nyman, G., and Lindenzweig, W. (1980). The decay of 0.57 s ^{114}Cs. *Zeitschrift fur Physik A*, 294:221–232.

[Rykaczewski et al., 1999] Rykaczewski, K., Batchelder, J. C., Bingham, C. R., Davinson, T., Ginter, T. N., Gross, C. J., Grzywacz, R., Karny, M., MacDonald, B. D., Mas, J. F., McConnell, J. W., Piechaczek, A., Slinger, R. C., Toth, K. S., Walters, W. B., Woods, P. J., Zganjar, E. F., Barmore, B., Ixaru, L. G., Kruppa, A. T., Nazarewicz, W., Rizea, M., and Vertse, T. (1999). Proton emitters ^{140}Ho and ^{141}Ho: Probing the structure of unbound nilsson orbitals. *Phys. Rev. C*, 60:011301.

[Schardt et al., 1981] Schardt, D., Batsch, T., Kirchner, R., Klepper, O., Kurcewicz, W., Roeckl, E., and Tidemand-Petersson, P. (1981). Alpha decay of neutron-deficient isotopes with $52 \leq Z \leq 55$, including the new isotopes 106Te (T1/2 = 60 μs) and 110Xe. *Nucl. Phys. A*, 368(1):153 – 163.

[Schardt et al., 1979] Schardt, D., Kirchner, R., Klepper, O., Reisdorf, W., Roeckl, E., and Tidemand-Petterson, P. (1979). Alpha Decay Studies of Tellurium, Iodine, Xenon and Cesium Isotopes. *Nucl. Phys. A*, 326:65.

[Schatz et al., 2001] Schatz, H., Aprahamian, A., Barnard, V., Bildsten, L., Cumming, A., Ouellette, M., Rauscher, T., Thielemann, F.-K., and Wiescher, M. (2001). End Point of the rp Process on Accreting Neutron Stars. *Phys. Rev. Lett.*, 86(16):3471.

[Schatz et al., 1998] Schatz, H., Aprahamian, A., Görres, J., Wiescher, M., Rauscher, T., Rembges, J. F., Thielemann, F. K., Pfeiffer, B., Möller, P., Kratz, K. L., Herndl, H., Brown, B. A., and Rebel, H. (1998). rp-process nucleosynthesis at extreme temperature and density conditions. *Phys. Rep.*, 294(4):167 – 263.

[Sellin et al., 1993] Sellin, P. J., Woods, P. J., Davinson, T., Davis, N. J., Livingston, K., Page, R. D., Shotter, A. C., Hofmann, S., and James, A. N. (1993). Proton spectroscopy beyond the drip line near A=150. *Phys. Rev. C*, 47(5):1933–1942.

[Shapira et al., 2000] Shapira, D., Lewis, T. A., and Hulett, L. D. (2000). A fast and accurate position-sensitive timing detector based on secondary electron emission. *Nucl. Instr. and Meth. in Phys. Research A*, 454(2-3):409 – 420.

[Tarasov and Bazin, 2004] Tarasov, O. and Bazin, D. (2004). LISE++ : design your own spectrometer. *Nucl. Phys. A*, 746:411 – 414. Proceedings of the Sixth International Conference on Radioactive Nuclear Beams (RNB6).

[Tidemand-Petersson et al., 1985] Tidemand-Petersson, P., Kirchner, R., Klepper, O., Roeckl, E., Schardt, D., Płochocki, A., and Żylicz, J. (1985). β-delayed particle emission from neutron-deficient Te, I, Xe, Cs and Ba isotopes. *Nuclear Physics A*, 437(2):342 – 366.

[Wallace and Woosley, 1981] Wallace, R. K. and Woosley, S. E. (1981). Explosive hydrogen burning. *Astrophys. J. Suppl.*, 45:389.

[Wiringa et al., 1995] Wiringa, R. B., Stoks, V. G. J., and Schiavilla, R. (1995). Accurate nucleon-nucleon potential with charge-independence breaking. *Phys. Rev. C*, 51(1):38–51.

[Yurkon et al., 1999] Yurkon, J., Bazin, D., Benenson, W., Morrissey, D., Sherrill, B., Swan, D., and Swanson, R. (1999). Focal plane detector for the S800 high-resolution spectrometer. *Nuclear Instruments and Methods in Physics Research Section A: Accelerators, Spectrometers, Detectors and Associated Equipment*, 422(1-3):291 – 295.

[Ziegler et al., 1985] Ziegler, J. F., Biersack, J. P., and Littmark, U. (1985). *The Stopping and Ranges of Ions in Matter*, volume 1. Pergamon.

Vita

Lucia Cartegni graduated from the University of Milano (Italy) with a Laurea degree in Physics. The experimental work for her thesis in Plasma Physics was performed at the University of Tromsø (Norway). She then worked at Oak Ridge National Laboratory (USA) as a post-master, studying radiation detectors. She obtained a PhD in Physics at the University of Tennessee (USA), with a dissertation in Experimental Nuclear Physics.